A Scalable Process for Rapid and Uniform Assembly of Repeated Origami-Like Structures Using Elastic Membranes

by

Charles M. Wheeler
B.S. Mechanical Engineering
University of Colorado at Boulder, 2013

Submitted to the Department of Mechanical Engineering
in Partial Fulfillment of the Requirements for the Degree of
Master of Science in Mechanical Engineering
at the
Massachusetts Institute of Technology

June 2015

Signature of Author .....
Charles M. Wheeler
Department of Mechanical Engineering
May 18, 2015

Certified by .....
Martin L. Culpepper
Professor of Mechanical Engineering
Thesis Supervisor

Accepted by .....
David E. Hardt
Professor of Mechanical Engineering
Graduate Officer

This page is intentionally blank.

A Scalable Process for Rapid and Uniform Assembly of Repeated Origami-Like Structures Using Elastic Membranes

by

Charles M. Wheeler

Submitted to the Department of Mechanical Engineering on May 18, 2015
in Partial Fulfillment of the Requirements for the Degree of
Master of Science in Mechanical Engineering

ABSTRACT

The purpose of this work is the modeling and prototyping of a highly parallelized process capable of folding large and compliant two-dimensional sheets into ordered, three-dimensional structures. The direct application of this work is the assembly of tissue scaffolds for replacement of human tissues and organs. A folding process capable of creating complex 3D geometries in a highly parallel, highly uniform fashion would enable the production of tissue scaffolds or other flexible systems at a fraction of the cost and time required by competing methods such as 3D printing. No existing research has attempted to apply folding to the manufacture of artificial organs and tissues; this work is the first to do so. This thesis introduces "membrane-driven folding," a process whereby pre-strained elastic membranes are used to drive folding. Rules for constraint and actuation, governing kinematic equations, and design rules necessary to implement this process are presented. These are then translated into functional requirements and a design for a prototype machine employing this process. This prototype machine is then tested and demonstrated to successfully achieve folding using this highly parallel, membrane-driven approach.

Thesis Supervisor: Martin L. Culpepper
Title: Professor of Mechanical Engineering

This page is intentionally blank.

Acknowledgements

There are many people without whom the opportunity to complete this thesis would not have been possible. First and foremost among them are my sister, mother, and father, who have been a boundless source of love, encouragement, and support. They consistently and lovingly push me to perform at my best, always pursuing new challenges and never settling for less. My work can seem all-consuming at times, but when the opportunities to return home finally do come around, there is truly no better place to be.

I would like to thank Professor Martin Culpepper, who invited me to the Precision Compliant Systems Laboratory (PCSL) at MIT, who introduced me to this project, and who has served as my greatest mentor over the past two years. Of all that I have learned here, many of the most invaluable items have come from Dr. Culpepper. His advice – be it academic, professional, or otherwise – has armed me to grapple with the challenges of navigating the seas of engineering, research, and life at MIT.

My senior labmates at the PCSL made my transition to graduate school possible, offering support and advice that I could not have gotten anywhere else. I would like to extend thanks to Sourabh Saha, who taught me to always keep an eye on the bottom line and whose advice proved pivotal in choosing the research path which led me to this work; to Aaron Ramirez and Marcel Thomas, for showing me the ropes in the PCSL, for their irreplaceable friendship, and for their inside advice on research, classes, and life; and to Joshua Nation, Brandon Evans, and Jonathan Monti, who made my first year in the PCSL a very warm and welcoming one.

I would like to thank my project collaborators at MIT and Northeastern University – in particular my labmate Lauren Chai. Many late nights have been spent pouring over this project and it would never have reached fruition without our many conversations together.

I would like to thank Jean Sack, who has been my greatest friend and confidant over the past two years. Without her unshakable support, many of the seemingly insurmountable challenges I have overcome here would have remained just that.

Finally, I would like to thank all of my friends at MIT and everywhere else, who have collectively made my life such a great one. It is easy at times to siphon all of our time and attention into our work – yet we must not forget that the people in our lives are what make it so fulfilling!

This page is intentionally blank.

Contents

FIGURES

Tables

Chapter 1

Introduction

The purpose of this work is the modeling and prototyping of a highly parallelized process capable of folding very large and compliant two-dimensional sheets (with hundreds or thousands of folding units) into ordered, three-dimensional structures. The work presented herein includes: an optimal approach for constraining and manipulating these large structures with repeated folding units; derivations of the fundamental equations governing the membrane-driven folding process; discussion of the means by which these relationships are converted into functional requirements for a real machine; the design process for a prototype machine meeting these functional requirements; a sensitivity analysis exploring the effect of fabrication errors on the ultimate performance of the machine; and finally, preliminary testing results of the machine itself. Existing research has contemplated neither the analysis nor design of a massively parallel folding processes of this type. The constraint rules, kinematic relationships, and design concepts presented in this thesis are the first of their kind and enable the end user to quickly develop a membrane-driven folding process meeting their functional requirements.

The direct application of this work is the assembly of tissue scaffolds for replacement of human tissues and organs. In this process, the geometry of a spatially complex 3D tissue is divided into slices and then mapped to a 2D sheet, where cells can be easily seeded and cultured using existing methods and technologies. The cultured sheet is then folded into a space-filling 3D structure, thus producing the 3D geometry of the desired tissue. A process capable of folding these geometries in a highly parallel, highly uniform fashion would enable the production of tissue scaffolds or other flexible systems at a fraction of the cost and time required by competing methods such as 3D printing. Previously, no attempt has been made to apply folding to the manufacture of artificial organs and tissues. This thesis proposes, models, and prototypes such a scalable process which is capable of folding compliant sheets into 3D structures using only a small number of actuators (five) and a pair of highly extensible elastic membranes. The prototype folding machine

is shown below in Figure 1.1. Visible in this photograph is the system of axles and rollers which ultimately enable folding through the manipulation of strain in attached elastic membranes (not pictured here):

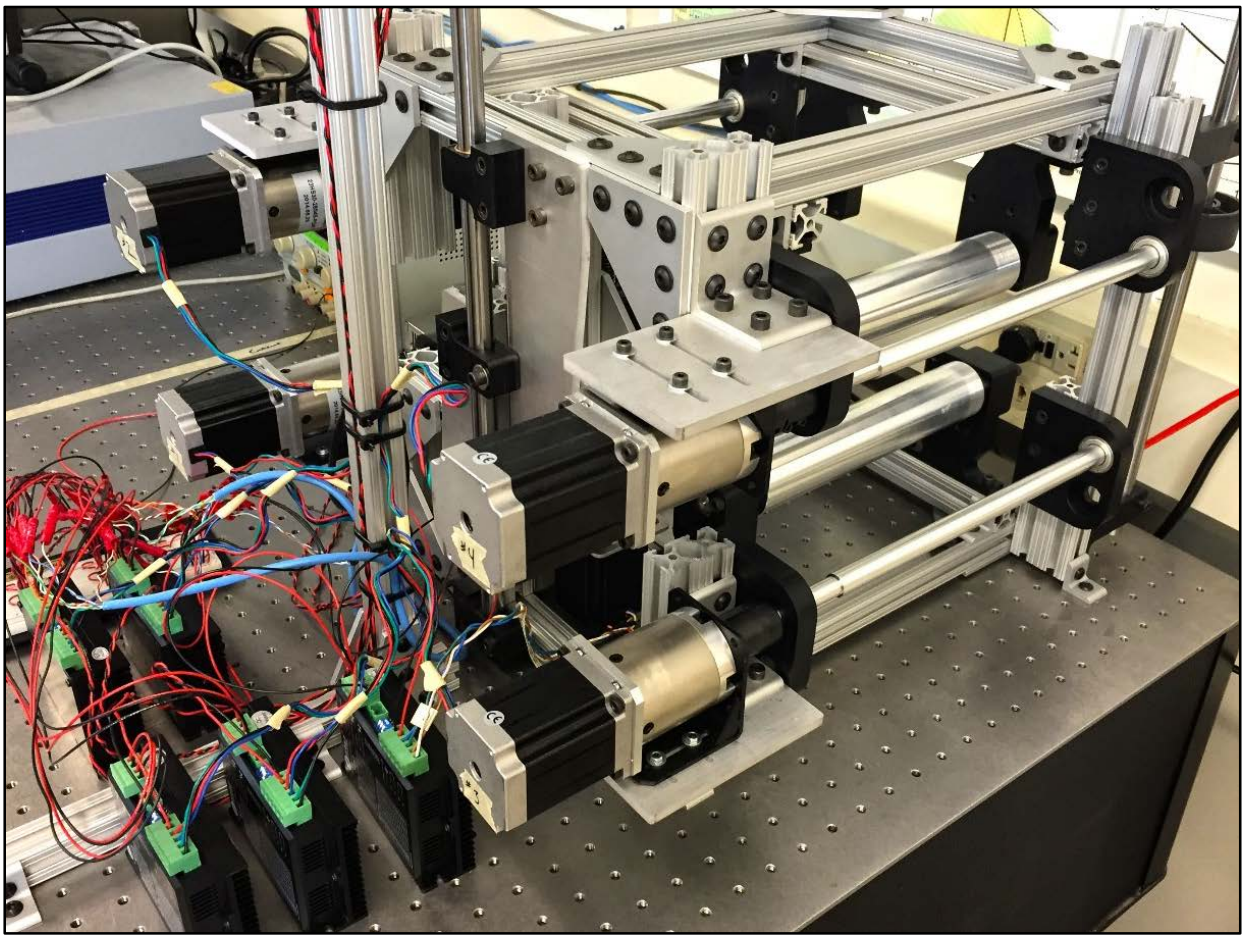

Figure 1.1: Prototype membrane-driven folding machine

Once the vertices of a thin folding film are adhered to the pre-strained membranes, this tension is released in a controlled manner, thereby folding the thin film. A series of images of this folding process are seen in Figure 1.2:

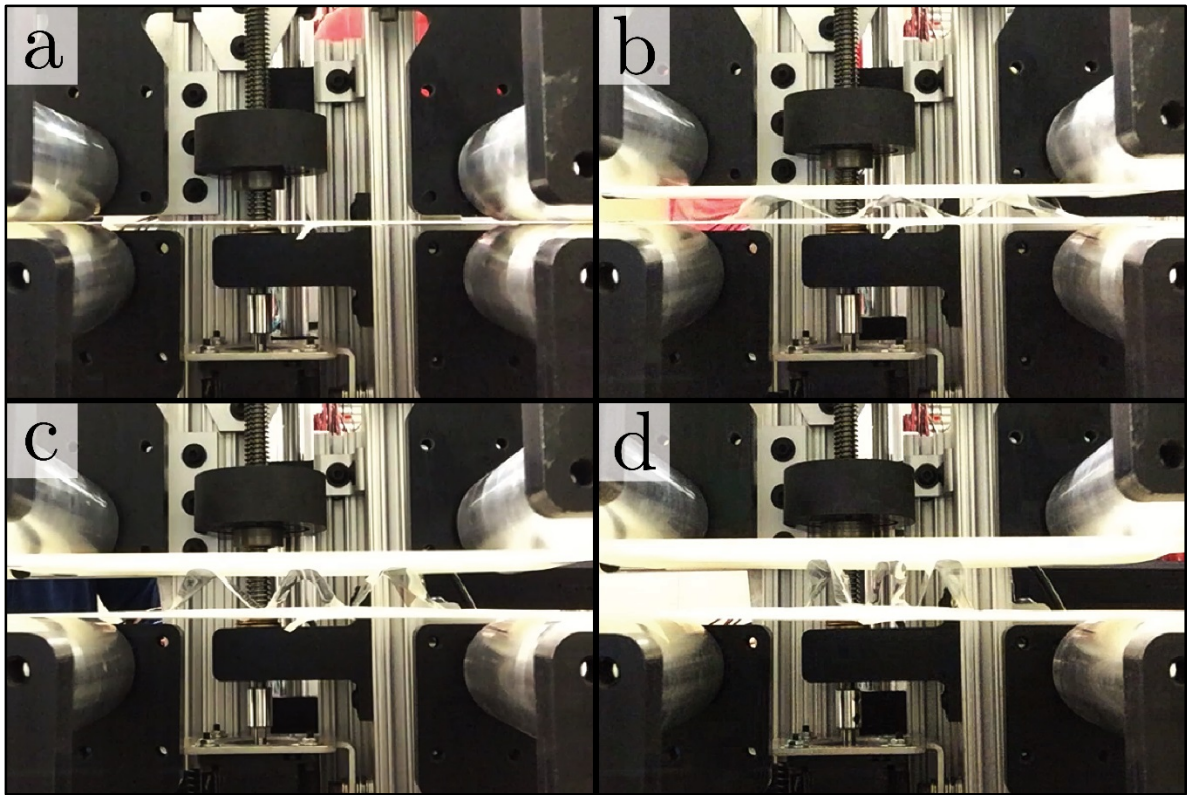

Figure 1.2: Timelapse of folding process

These images clearly show the emergence of a repeated, wave-like folding pattern from an initial flat sheet. This thesis details the development of this folding process, beginning with a discussion of relevant principles shared with the well-known art form of origami.

1.1 Origami Principles & Design

Origami has recently received increased attention from the engineering community because, in many fields, the capability to rapidly and cheaply transform a simple, 2D sheet into a complex 3D geometry poses significant time, cost, and throughput advantages. In recent years, "origami" has graduated from a traditional art form into an area of research, and now the term loosely refers to any transformation of a 2D sheet into a 3D structure. It is important to review a few key principles from the traditional art form because they apply directly to the folding process presented in the following chapters.

1.1.1 Origami: Systems of Panels, Hinges, and Vertices

Traditional paper-folded origami is produced by introducing targeted deformations (creases) to a flat sheet of paper, thereby transforming it into a stunning 3D structure:

Figure 1.3: Origami rhinoceros beetle [1]
Reproduced with permission. All rights reserved.

Origami structures are often depicted alongside their *folding maps* or *folding patterns*, which depict the "instructions" for folding each system (one such folding map can be seen in Figure 1.4). Three features can be observed in these maps: hinges, vertices, and panels. Collectively these serve to "map" the starting sheet to the final structure, and each feature has its own properties:

Hinges – Represented as lines on the folding map, hinges correspond to the locations where folding is induced. Often considered equivalent to revolute hinges, these features imbue the structure with its mechanism-like folding behavior.

Vertices – Vertices occur any time two or more hinges meet. Hinges start, terminate, or change direction at vertices, allowing different parts of the sheet to fold in different ways. In stiff systems, the vertices also dictate the degrees-of-freedom of the system by restricting the freedom space of coincident hinges.

Panels – The planar, polygonal regions between hinges and vertices; the "white space" on the folding map. Panels comprise the surface area of the sheet and enclosed volume after folding.

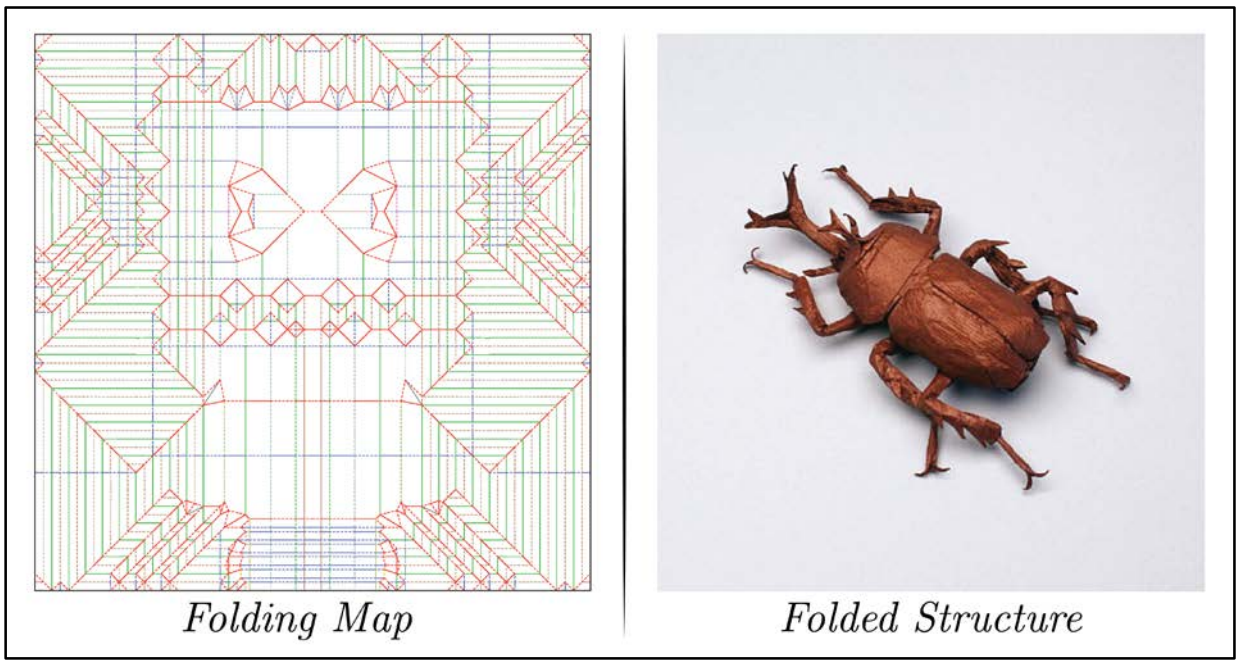

Figure 1.4: Rhinoceros beetle folding map and final form [1]
On the folding map, lines are hinges, vertices are where lines intersect, and panels are white space.

1.1.2 Fold Patterns: Uniformity vs. Complexity

The arrangement of hinges, vertices, and panels on the fold map dictates the final geometry, the folds which must occur for the structure to take shape, and the constraints and actuation which must be imposed (based on its degrees-of-freedom). Origami structures designed as art pieces typically map to highly complex and non-uniform folding patterns. Some regions feature very dense folding patterns while others are relatively sparse by comparison. In Figure 1.5 it can be seen that, using a single sheet, the artist Robert Lang successfully captures many details of the head, legs, and body of the beetle, despite their great differences in form. These differences manifest as variations in the folding map; complex structures such as the beetle's legs require a high concentration of complex folds, while larger surfaces (its thorax and abdomen) are comprised of comparatively few and simple folds. Thus the non-uniformities (highlighted in Figure 1.5) occur in two ways: the density and arrangement of folds.

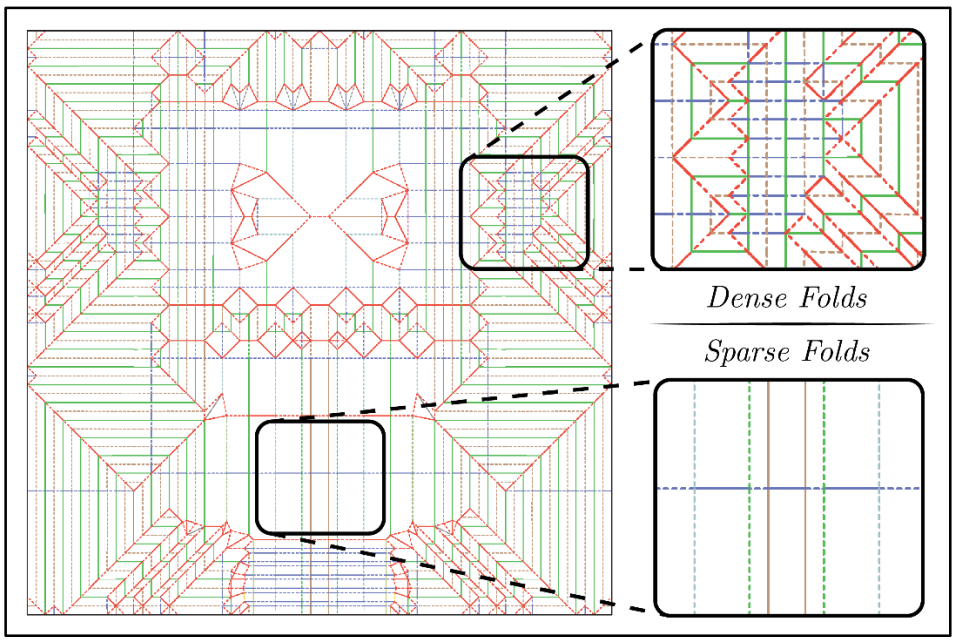

Figure 1.5: Dense and sparse regions for an artistic origami fold [1]
This non-uniform pattern produces intricate pieces of art but is undesirable for bulk folding.

Density: Areas dense with folds require additional actuation when compared to sparsely-populated regions, so folding effort (number of actuations per unit area) is not distributed equally.

Arrangement: Variations in the folding pattern itself imply that different actuation and constraint topologies are required from one location to another; the constraint requirements differ between regions.

This highly non-uniform arrangement is desired for origami sculptures, where intricate details and shapes are sought. However, when the goal of the folding process is the bulk transformation of 2D sheets into uniform 3D structures it remains advantageous to pursue to fold patterns exhibiting highly uniform, repeated arrangements.

Two examples of uniform, repeated origami patterns are the "accordion fold" and "Miura-Ori" fold, seen in Figure 1.6. From an assembly and manufacturing perspective, these patterns are attractive for a number of reasons:

- Vertices are repeated and spaced uniformly
- Constraint and actuation requirements do not change from one unit to the next
- All vertices remain external (patterns do not fold around / enclose themselves)
- Efficient and uniform space-filling behavior when folded

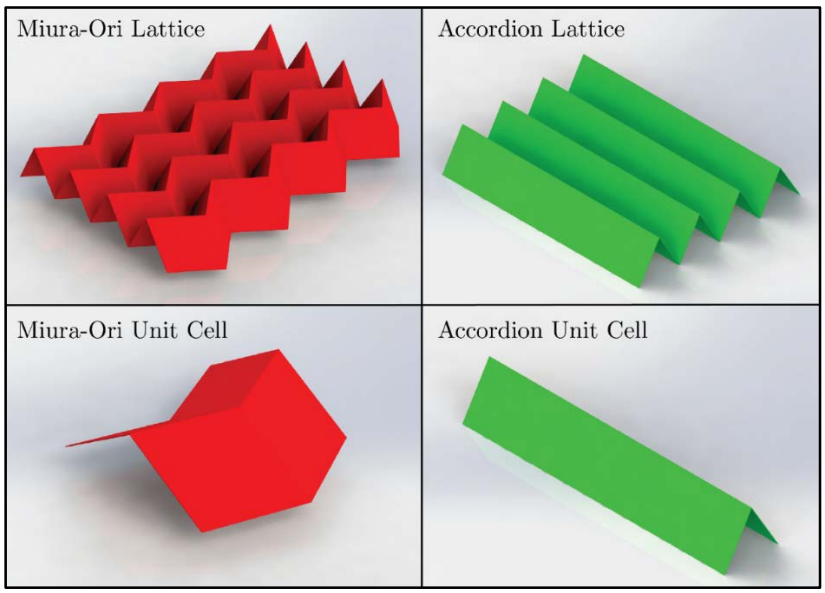

Figure 1.6: Miura-Ori and Accordion folds
The Miura-Ori folds in two directions, while the Accordion folds in just one.

This thesis considers the accordion fold due to its greater simplicity and single-direction actuation behavior. However, because the Miura-Ori fold is perhaps the most popular and well-understood two-direction folding pattern of this type, it deserves mention here and should be considered as an option when a folding process is needed.

1.1.3 Rigid Origami Degrees-of-Freedom

Most analysis treats origami as being *rigid*, that is, compliance comes only from the structure's hinges and panels have no capability to deform. Tomohiro Tachi offers the following definition of rigid origami [2]:

> *"Rigid Origami is a piecewise linear origami that is continuously transformable along its folds without deformation by bending or folding of any facet."*

The rigid assumption is equivalent to treating origami as a system of linkages and joints: mobility is granted by the joints (hinges), while the linkages (panels) remain undeformed. For the fold process presented in the following chapters, the rigid assumption is not valid due to the extreme compliance of the materials being folded. However, analysis of an equivalent rigid origami system still provides insight into the pattern's motions during folding and the positions/movements required of its actuators/constraints, respectively.

The rigid representation of the accordion fold of interest is quite straightforward: each joint imbues the system with an additional degree of freedom. With this assumption alone, the accordion fold is underconstrained, but the degrees of freedom can be reduced to one if all vertices are constrained in two planes (the "mountain" vertices in one plane, and the "valley" vertices in another). The motion of the lattice with this one degree of freedom constraint resembles the expansion and contraction of a bellows and is the desired actuation scheme for the external constraints and actuators.

1.2 Motivation & Application: Origami for Human-Tissue-Engineering

The work presented in this thesis is intended as a prototype and precursor process for the rapid assembly of engineered human tissues. The National Academy of Engineering has identified Human-Tissue-Engineering as a component of their "Personalized Medicine" Grand Challenge [3]. Engineered tissues could greatly supplement the supply of organs available for transplantation (limited supplies currently lead to thousands of deaths each year), while also providing a tool for testing and screening new medical therapies before the human trials stage.

A major challenge in the development of man-made organs and tissues is the geometric complexity of their microstructure. This microstructure requires a means by which an adequate supply of nutrients and oxygen may be delivered to cells and metabolic waste can be removed. Vasculature serves this purpose in living creatures, and are likewise required when growing synthetic tissues. The microstructure also typically includes a variety of cell types necessary for the function of the desired tissue or organ. In many cases, both the types of cells required and their specific arrangement affect the function of the tissue, as has been demonstrated in multiple studies [4-7]. Therefore an effective approach to tissue scaffolding must be capable of precisely placing many cells of varying types in a complex 3D geometry. Existing state-of-the-art approaches remain limited in three ways:

1. **Control** – While some success has been achieved with simple planar or hollow tissues, most existing approaches fail to recreate the intricate geometries required of complex human tissues [8-11]. Complex, fully 3D tissues have been successfully created using a droplet printing approach [12-24]. However, these methods suffer from the below disadvantages.

2. **Throughput** – 3D droplet printing methods capable of achieving the desired 3D architecture are not capable of producing human tissues quickly enough. The use of this approach for the creation of large tissues with repetitive high resolution microscale architecture is not feasible [16, 25].
3. **Scalability** – As a result of the above limitations, existing methods are not capable of meeting demand for organs and tissues from those in need.

Origami-inspired tissue scaffolds are well-positioned to solve all three of these problems by coupling existing well-controlled culturing methods (patterning cells onto sheets) with a rapid, parallelized folding process.

1.2.1 Sorting Cells on Patterned Sheets

Functioning tissue not only requires the presence of the right cell types, but also the correct placement of each cell in relation to its neighbors. To produce a viable engineered tissue, an assembly method must therefore be capable of correctly placing all cells in the desired locations within the tissue volume. In 2011, Gunjan Agarwal and Dr. Carol Livermore-Clifford demonstrated an effective method for sorting cells on 2D sheets [26]. Their technique, termed "Templated Self-Assembly by Selective Removal (TASR)," is illustrated in Figure 1.7.

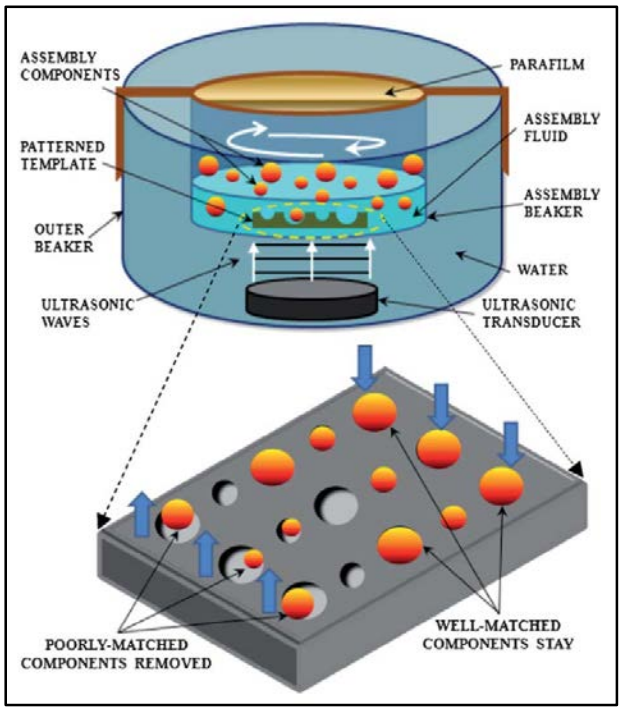

Figure 1.7: Illustration of ultrasonic cell sorting method
Reproduced with permission. All rights reserved. License #3626020440221.

TASR begins with the fabrication of a pattern template, were hemispherical wells of varying sizes are etched into a small silicon die. A solution of cells (of varying types) is pipetted onto the die, after which an ultrasonic transducer excites the system and sorts cells into their desired locations. Different cell types differ in size (diameter) and pair preferentially with different well sizes (small/large cells settle in small/large wells, respectively). The ultrasonic perturbation drives this matching process by unseating cells from mismatched wells and pairing cells with well-matched wells. As seen in Figure 1.8, TASR allows cells to be accurately patterned onto a 2D surface.

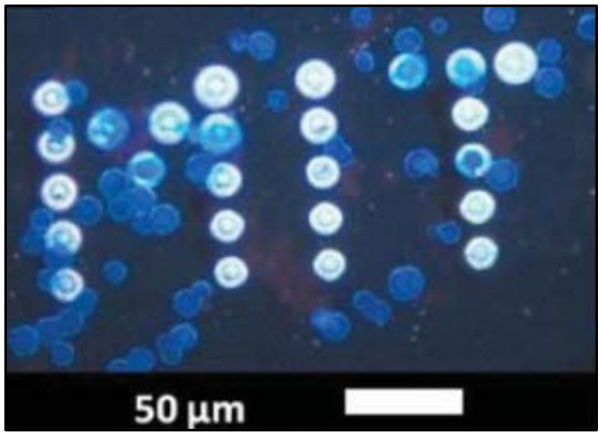

Figure 1.8: Cells arranged with TASR to spell "MIT"
Reproduced with permission. All rights reserved. License #3626020440221.

1.2.2 Transforming Patterned Sheets into Engineered Tissues

TASR enables the accurate placement of cells on a 2D sheet. By adding a subsequent folding process, this 2D sheet is transformed into a 3D volume where the arrangement of all cells within the volume is deterministically controlled. Careful selection of the 2D pattern allows for the production of intricate 3D cell architectures. For example, if endothelial cells are patterned on adjacent sheets, a blood vessel-like structure is produced after folding is completed, as seen in Figure 1.9.

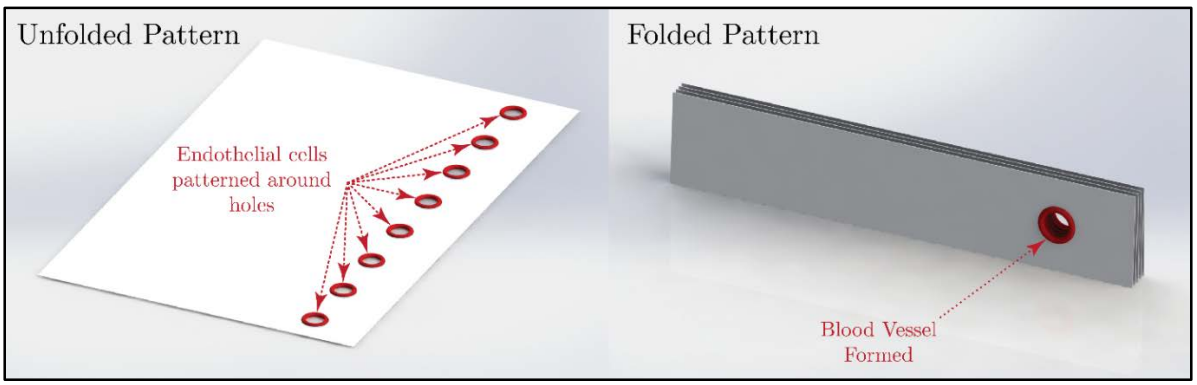

Figure 1.9: Ring patterns can fold to produce vasculature
Careful selection of the cell arrangement allows 3D features, such as vasculature, to be replicated when the folding process completes.

No previous work has considered the use of an origami-like process for the assembly of cultured sheets into complete tissues. This thesis documents a prototype process designed to solve the problem of folding compliant sheets in a robust and highly scalable fashion.

1.3 Prior Art: Self-Assembling Origami

Existing research on the development of novel folding processes deals primarily with *programmable materials* – materials whose physical properties (in particular, shape) change in response to external stimuli. In the case of origami, programmable matter is exploited for the purpose of achieving self-folding structures. Self-folding behavior is highly attractive because no external actuators are required and various geometries can be achieved simply by changing the locations of the programmable hinges. Many mechanisms for self-folding have been investigated, including shape-memory polymers, photo-thermal and photo-chemical materials, swelling bilayer hinges, and even the use of cell traction forces [27-36].

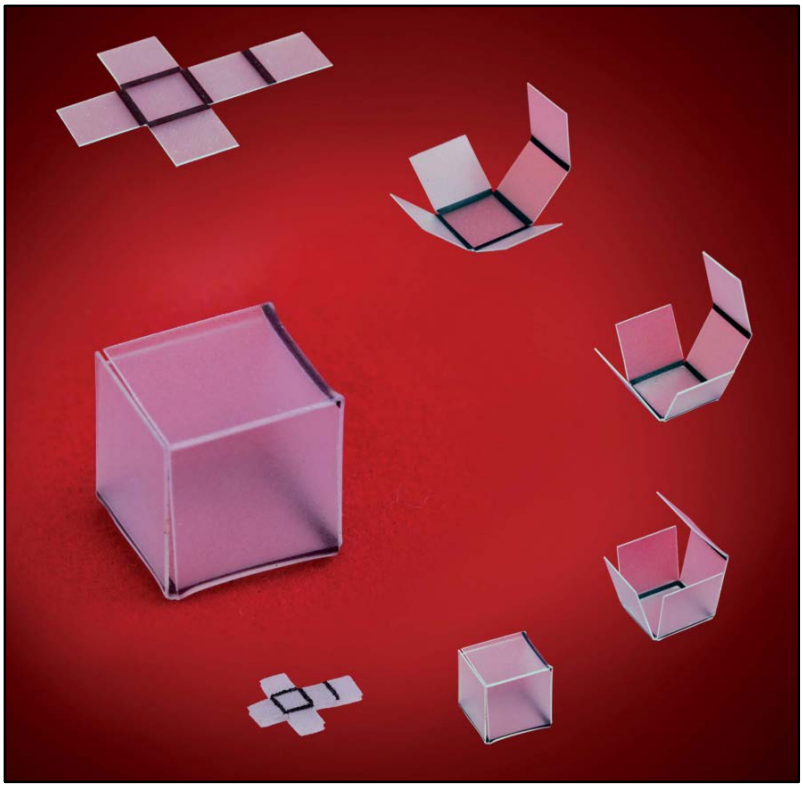

Figure 1.10: Light-activated self-folding box [32]
Reproduced with permission. All rights reserved. License #3626020316935

1.3.1 Scaling Limitations

The structures produced using self-folding often resemble boxes or packages, where the folding structure is designed to encapsulate another material (for applications such as drug delivery). Virtually all self-folding structures contain fewer than 20 folds, with the vast majority containing fewer than 10 – in the case of the popular cross-pattern box (shown in Figure 1.10), only five folds are present. In fact, there is a distinct lack of any large, self-folded structures whatsoever in the literature, and no self-folding examples of large accordion or Miura-Ori folds are currently known to exist. The lack of large self-folded structures is partly attributable to unfavorable scaling laws with respect to both the scaling of characteristic lengths and the scaling of the number of discrete folding units within the structure. Consider two plates connected by a hinge as shown in Figure 1.11:

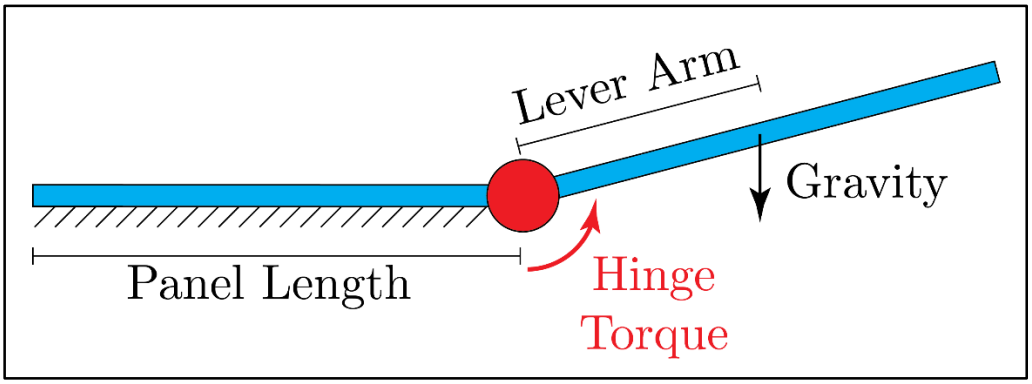

Figure 1.11: Panel/hinge model for scaling laws

In a back-of-the-envelope calculation, the maximum torque output of the self-folding hinge is said to scale with its volume ($[T] \sim l^3$; l is a characteristic length). The moment it must lift (the weight of the plate times its lever arm) is then said to scale as $[T_{req}] \sim Vl \sim l^4$. The torque output of the hinge does not scale with the lifting requirement, and a small system cannot simply be scaled directly to produce a successful larger version.

Second, large origami systems inherently include long serial chains with many folding units in a row. Considering one point of the system to be fixed, it is important to remember that each hinge must not only lift its adjacent panel – it must also be capable of pulling *all downstream folding units towards it*:

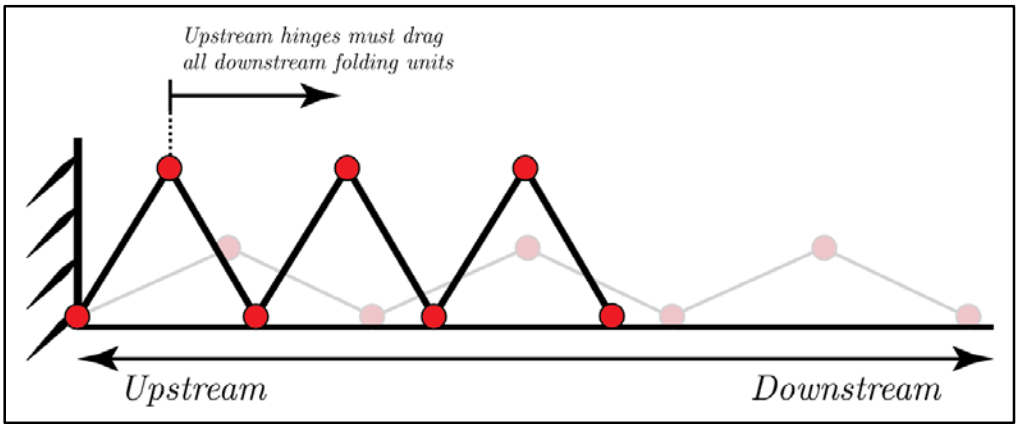

Figure 1.12: Actuation of a long serial linkage chain

Upstream hinges must be capable of overcoming drag and friction experienced by the entire downstream system, and so this approach is not feasible (in generality) for very large systems where serial chains are dozens or hundreds of folding units long.

1.3.2 Biocompatibility

In addition to the scaling limitations outlined above, self-folding structures typically utilize exotic materials to achieve their programmable behavior, the vast majority of which are non-biocompatible. This immediately eliminates many potential options for self-folding that might otherwise be acceptable in other applications.

1.3.3 Fabrication Effort

A final limitation of self-folding methods is that folding features must be fabricated into each structure that is produced. This introduces additional time-consuming steps into the fabrication process, all of which must be repeated for each example produced. Utilizing external actuation – i.e. a separate machine which performs the folding – eliminates this additional fabrication overhead. The folding structure can be a simple homogeneous sheet (with no special folding features) and the machine simply guides it into the desired configuration.

1.4 Thesis Outline

Chapter 2 of this thesis discusses potential options for actuating and constraining origami and introduces design rules for ensuring proper folding of very large systems. The design rules developed in Chapter 2 motivate the use of highly extensible membranes as actuators for driving folding. Chapter 3 presents the equations necessary for implementing these extensible membranes as the drivers for folding, including kinematic relationships, error sensitivity, and a correction for practical implementation. Chapter 4 details the design of a prototype membrane-driven folding machine, developed using the equations from Chapter 3. Chapter 5 details the setup and preparation required for running the prototype machine and includes preliminary results and discussion. Chapter 6 concludes this thesis with a synopsis and a discussion of potential future work.

Chapter 2

Methods for Controlled Folding

A well-controlled folding process is one in which:

1. All hinges fold in the correct direction
2. All hinges reach their desired fold angle

Section 2.1 of this chapter introduces the concept of Hinge Directionality and identifies the two classes of options for controlling this during folding. Section 2.2 discusses options for actuation of a folding structure and the distribution of deflections throughout simple systems. Section 2.3 describes the actuation scheme implemented in the prototype machine: the pairing of the Direct-Displacement method with Pointwise Actuation.

2.1 Hinge Directionality

Controlling the direction of hinge folding is a crucial part of implementing a successful folding process. At best, the failure to achieve proper directionality in a hinge (hereafter deemed "misfolding") will result in the misplacement of at least one attached plate. However, other common error modes of misfolding can result in more serious consequences. First, a misfolded hinge can lead to unwanted warping in the system, potentially driving it into a state of premature lockup. In this case the folding process cannot be completed and further forcing may simply damage the origami structure or the actuators themselves. Second, origami systems tend to be tightly coupled, and a misfolding error in one hinge may propagate to induce other misfolding errors. The more tightly coupled the system (the fewer global degrees of freedom it possesses) and the more it behaves as idealized "Rigid Origami," the worse this error propagation will be. In the extreme case of a perfectly rigid, single-degree of freedom system, one misfolded hinge necessarily requires that *all* hinges in the system are likewise misfolded.

A hinge feature behaves as a revolute joint, connecting two panels (linkages) along an axis of rotation. Each joint has a single degree of freedom and can deflect in two directions: the "mountain" direction or the Valley direction (as described in a top-down view). The folding pattern dictates the arrangement of mountain and valley hinges in such a combination that they form a foldable mechanism.

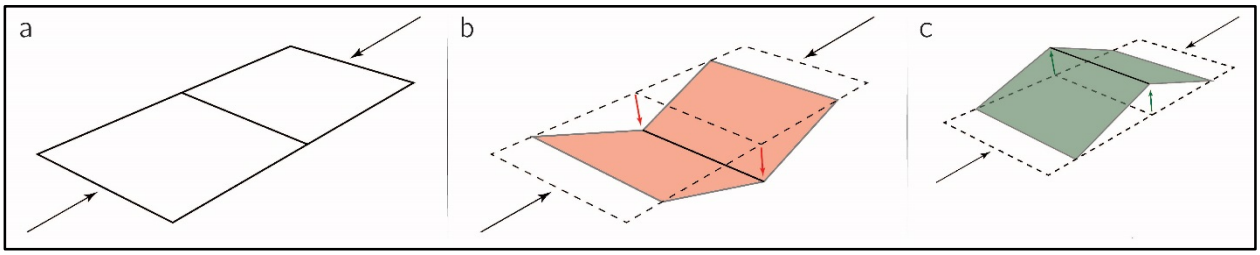

Figure 2.1: (a) Unfolded hinge; (b)"Valley" fold; (c) "Mountain" fold

Strategies for controlling hinge directionality fall into two regimes, based on the direction of actuation forces applied in each case: Controlled Buckling and Direct-Displacement Folding.

2.1.1 Controlled Buckling

The first method for controlling hinge directionality treats the folding procedure as a Controlled Buckling process. This regime models the case where a system of many hinges is folded by only a small number of actuators. Each actuator is attached to and manipulates either a single vertex or a single fold, after which the folding process is driven by bringing actuators towards one another. This induces compressive loading into the system and intermediate hinges buckle away.

The simplest possible case of a buckling-driven folding process is that of two adjacent panels connected by hinge. One actuator is attached at each end, and when they are drawn together, compressive loads are induced:

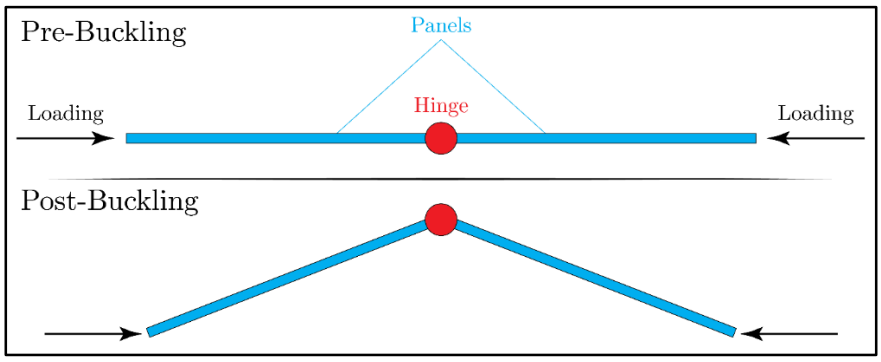

Figure 2.2: Diagram of buckling-driven folding

If no special concession is made for designing a directional hinge and the eccentricities of the compressive loads are zero (the loads pass through the center of the hinge), then the system exists at a bifurcation point where the joint is equally likely to buckle up or down. This behavior is highly undesirable as the buckling response of the joint is neither predictable nor consistent.

"Preferential buckling," whereby the direction of buckling can be reliably controlled, is achieved by biasing the system in such a way that one buckling pathway becomes sufficiently more energetically favorable than the other. Some options for direction-control features include: (a) offsetting the joint from the forces such that an eccentric condition is achieved (this eccentricity must be great enough to overcome any imperfections which might exist in the system); or, (b) implementing hard-stops or similar features which prevent the joint from buckling in the undesired direction (these options can be seen in Figure 2.3).

The main benefit of the Controlled Buckling approach is that it offers control over the direction of the buckling path without the need for additional actuators or external constraints. However, the success of this approach is contingent on two assumptions:

1. The direction-control features must be sufficiently designed as to overcome any undesired moments or eccentric forces seeking to drive the system in an undesired direction
2. The panels must be sufficiently stiff to bear the applied loads without buckling

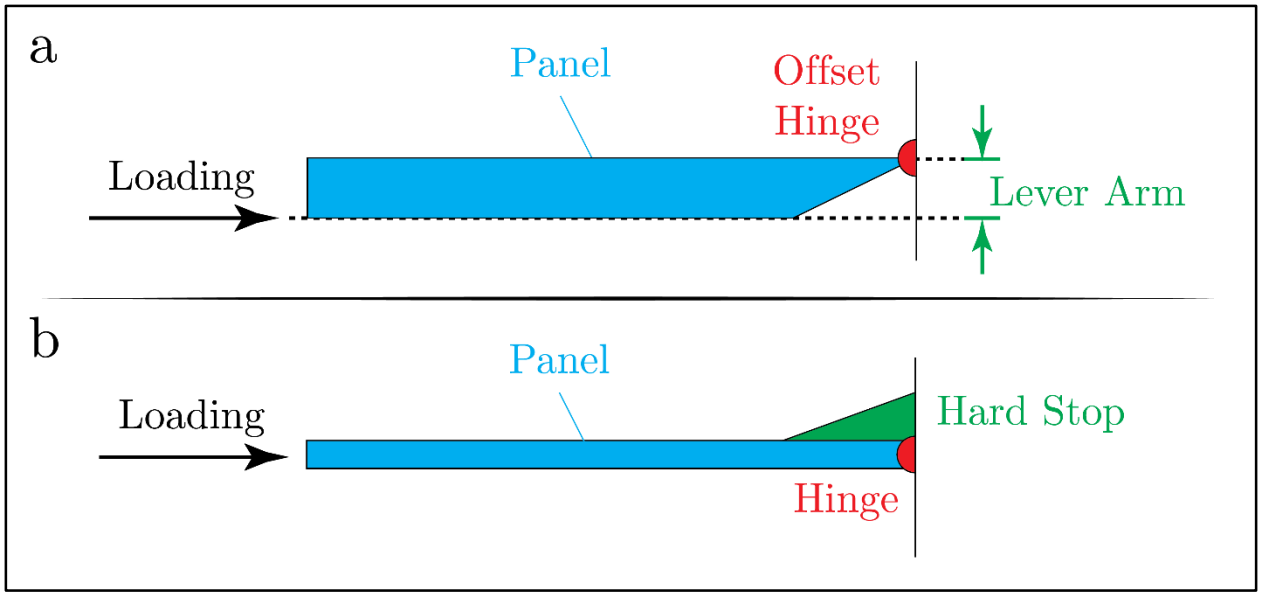

Figure 2.3: Features to control buckling direction
(a) Loading offset from hinge to create moment
(b) Hard-stop to prevent undesired buckling

Thus, accurate knowledge of the internal forces, moments, and flex experienced in the system is necessary to design optimal direction-control features. For the folding of extremely compliant sheets, this approach is simply not feasible as such structures will buckle readily under compressive loading.

In designing a folding system relying on Controlled Buckling, it is important to remember that buckling often occurs in the form of an energy release. Consider the example in Figure 2.4, which shows a pair of hinges utilizing hard-stops to guide the buckling direction. In the resting state of this system, the hard-stops are very nearly engaged, but have not yet made contact. Upon loading, the system misfolds slightly – a result of manufacturing or assembly errors. However, but the hard-stops prevent further misfolding. As the imposed compressive load increases, the stored energy increases until sudden snap-through occurs in the opposite direction, releasing the stored energy very rapidly. The hard-stops have succeeded in restricting folding to the desired direction, but have introduced the potential for very sudden (and potentially unsafe) energy release.

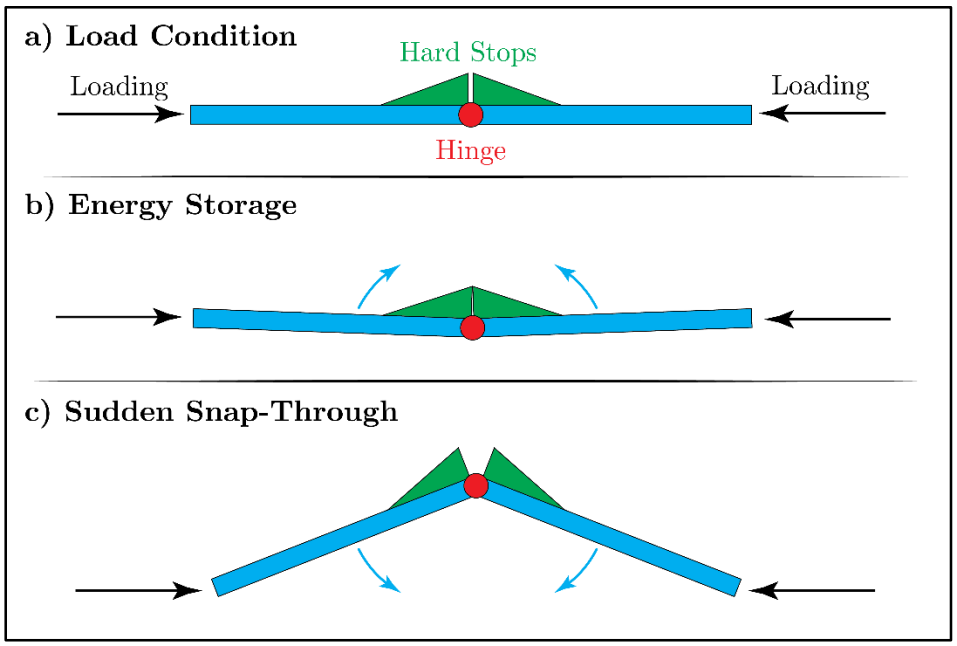

Figure 2.4: Snap-through of compressed joint with hard-stops

2.1.2 Direct-Displacement Folding

Direct-Displacement Folding is the second means of controlling hinge directionality. In this case, we again consider a pair of plates connected by a hinge. However, rather than apply compressive loads at the two ends of the system, we directly control the displacement at three locations. In this regime, all three vertices are directly manipulated at the cost of needing a third actuator. This explicit control of all vertices eliminates the possibility for a hinge to fold in the undesired direction. No direction-control features are required as the hinge directionality is directly imposed, and the response of the system is predictable and deterministic. Additionally, the lack of any buckling mechanism in this approach eliminates the potential for a sudden and destructive release of energy, as is possible in the Controlled-Buckling regime.

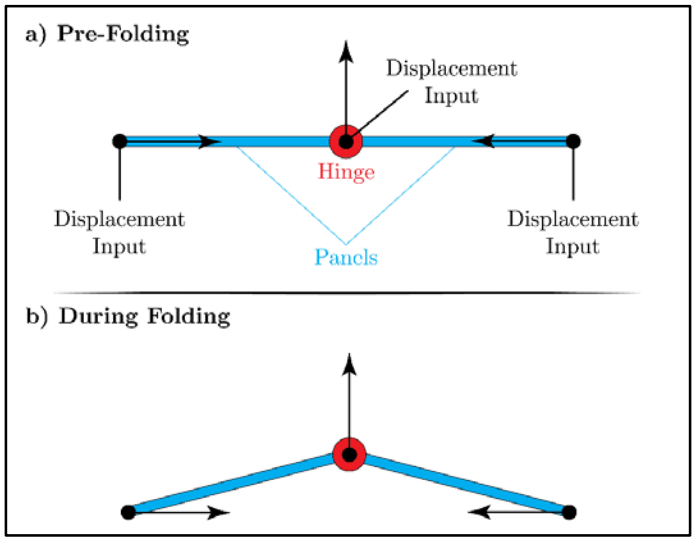

Figure 2.5: Diagram of direct-displacement folding

Unlike the Controlled-Buckling approach, a system of two loads cannot be used to drive a series of intermediate hinges – rather, a separate input is required at each hinge. Because the number of hinges scales directly with the complexity of the system, even moderately-sized systems may require actuation inputs at dozens or hundreds of locations. This approach is not viable for folding very complex patterns with many non-uniformities, as this would require an unreasonable number of independent actuators. However, folding of *very large* systems is feasible in certain special cases, where the folding behavior is highly uniform across the structure. Patterns such as the accordion fold can be exploited, as a single degree of freedom is repeated throughout the entire structure. In this case, it is possible to use a single actuator to manipulate several points at once. This is the premise for the folding process presented in Chapter 3.

2.2 Actuation Methods

In addition to controlling folding direction, it is necessary to control the fold angles of each hinge to ensure the structure reaches an accurate final geometry; deviations from this final

geometry should be minimized. While origami mechanisms such as the Miura-Ori pattern possess only a single degree of freedom in theory, the inherent compliance in real systems means that the true behavior falls short of the ideal and one must consider the deflections and warping which will arise. It is therefore important to choose an actuation scheme which will allow for the most uniform folding behavior, even in the presence of warping and deformation.

In this section we consider the repeated Miura-Ori structure alongside a one-dimensional grid of springs. Three actuation schemes are considered:

- **Two-Point Actuation,** where the system is actuated by manipulating two nodes
- **Two-Edge Actuation,** where the system is actuated by manipulating two rows of nodes
- **Pointwise Actuation,** where all nodes are manipulated direction.

The system of springs is not intended to model the origami lattice directly, but instead serves as a simplified, instructive analogue for the more complicated Miura-Ori. In this section it is assumed that all hinges deflect in the desired direction.

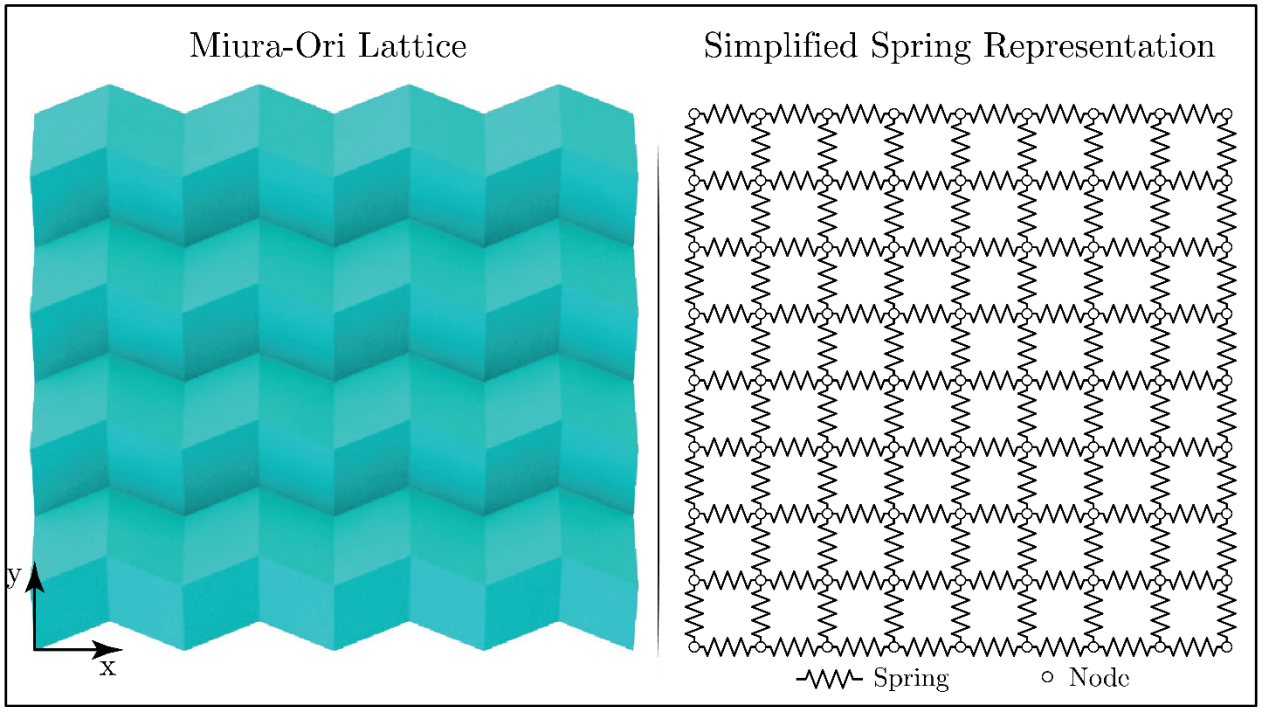

Figure 2.6: Miura-Ori lattice and simplified spring-node representation

2.2.1 Two-Point Actuation

In the case of *Two-Point Actuation*, the Miura-Ori is fixed at one corner and actuated by an imposed force at the opposite corner. This arrangement, along with the analogous spring-grid example, is seen in Figure 2.7. In this example, the bottom left corner is brought towards the top right and a net compression is induced in the structure. The response of the structure can be analyzed in two ways: (a) by observing the total *displacement* of each node in the structure; and (b) by observing the total *compression* of each spring element in the structure. These representations are shown in Figure 2.8.

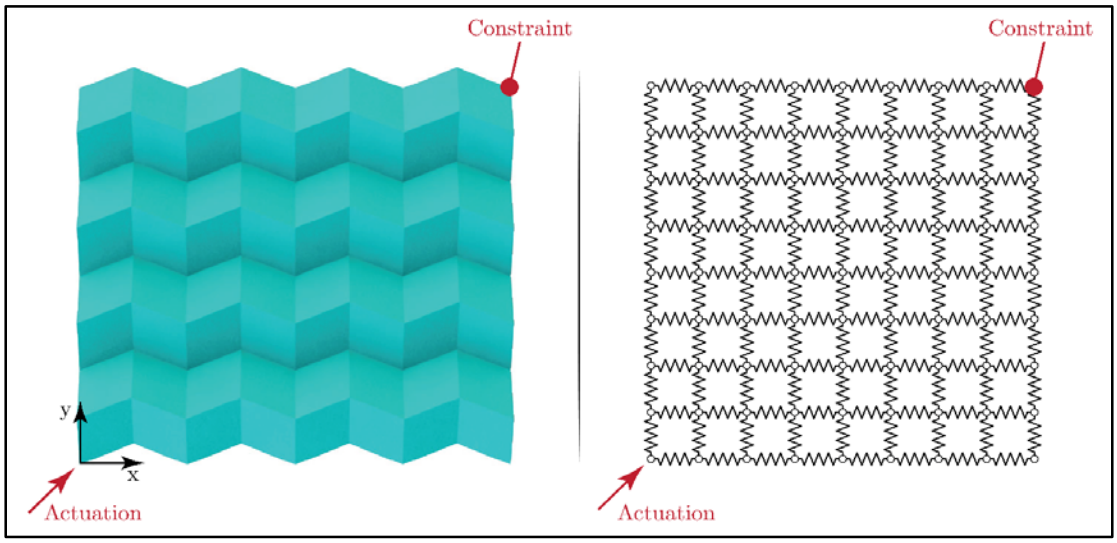

Figure 2.7: Two-point actuation
Top-right corner held fixed; bottom-right corner actuated inwards

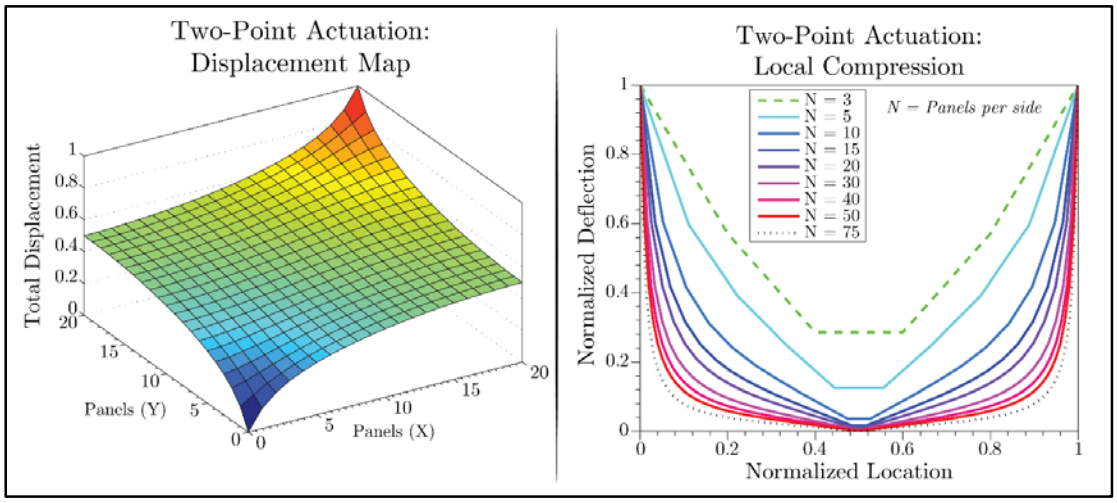

Figure 2.8: Displacement and compression maps for two-point actuation
"Local Compression" graph shows compression along line from corner-to-corner

Both maps clearly show that compression through the structure is far from uniform. The corners nearest the actuation/constraint points experience most of the compression, while the center of the structure sees very little. Unfortunately no modulation of the applied forces will correct this non-uniformity – it is inherent to this loading arrangement.

This actuation method may be sufficient for origami structures possessing very tightly controlled degrees of freedom, where all undesired deflections are negligibly small and shape change results only from revolution of the hinges. However, for soft structures such as those folded in this work, the non-uniformities which arise from this approach invalidate it as a potential solution. This method is efficient from an actuation perspective (requiring only two manipulation points), but it is a poor choice when uniform folding of non-stiff structures is required.

2.2.2 Two-Edge Actuation

In the *Two-Edge Actuation* case, we consider the structure to be actuated from one side and constrained on the other; now an entire *layer* of nodes is actuated, as shown in Figure 2.9:

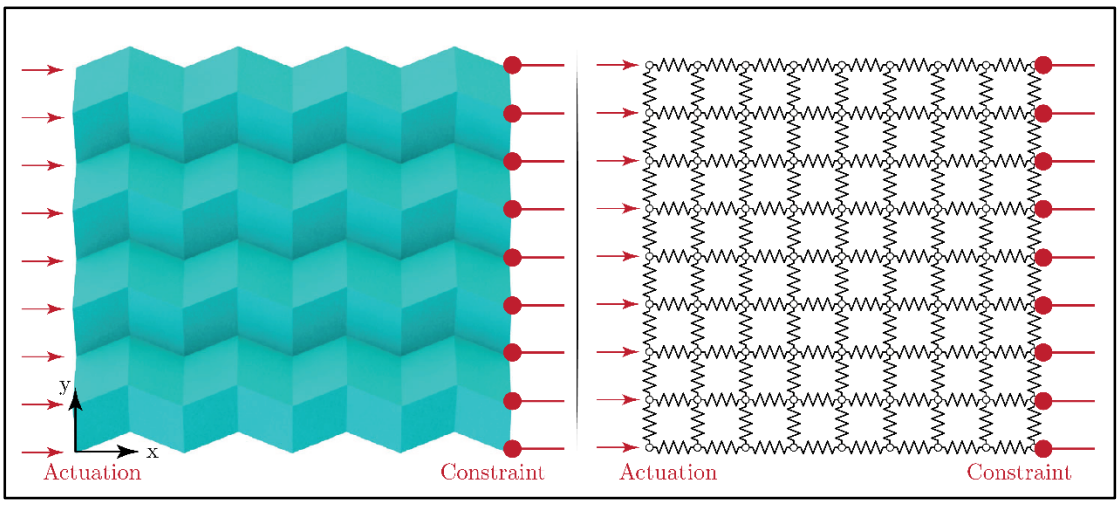

Figure 2.9: Two-edge actuation
Right nodes held fixed; left nodes actuated inwards

In this case, all points share the same slope and the folding response of the system – seen in Figure 2.10 – is uniform (compression is equal at all points):

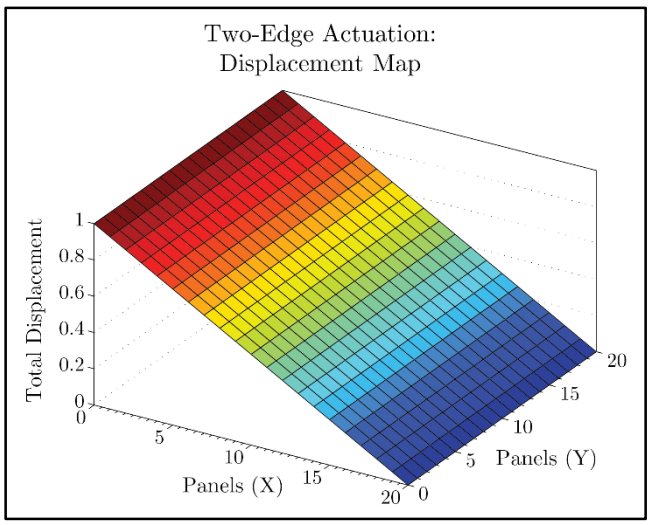

Figure 2.10: Displacement map for two-edge actuation

However, this assumes a perfectly uniform spring behavior. If a non-uniformity is introduced such that the stiffness of one layer of springs differs slightly from its surrounding layers, the result in Figure 2.11 arises:

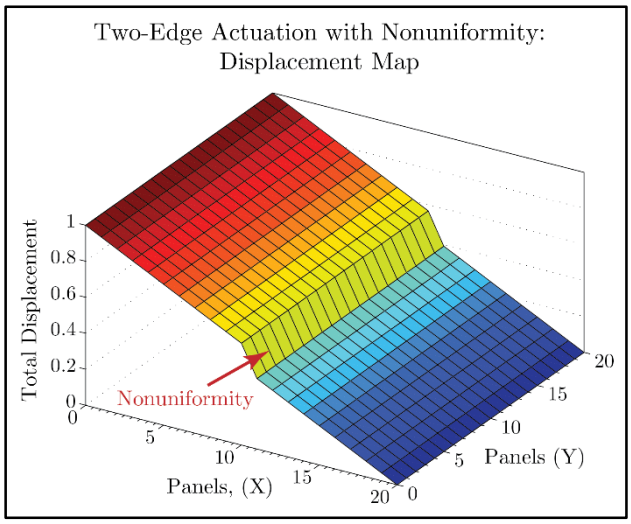

Figure 2.11: Displacement map for two-edge actuation with nonuniformity

In this scenario, no modulation of forces can correct for the difference in deflection between layers. Although Two-Edge actuation achieves uniform actuation using ideal, uniform springs, it is insufficient for achieving a uniform response from real, non-uniform systems.

2.2.3 Pointwise Actuation

The final actuation case we consider, *Pointwise Actuation*, manipulates the structure at *each* vertex. The results of the loading condition are straightforward – each vertex is actuated independently, so the endpoints of all springs can be dictated directly, achieving whatever shape is desired. This one-to-one mapping of vertex-to-actuator allows for direct control of all folding surfaces, and the actuating machine can actively correct for nonuniformities in the folding structure.

2.3 Combining Direct-Displacement & Pointwise Actuation

The similarities between Direct-Displacement Folding and Pointwise Actuation are clear: both require manipulating the folding structure at each vertex, ensuring the proper outcome for both hinge directionality and folding itself. It is therefore natural to pair these approaches in the pursuit of a reliable folding scheme; the means for doing so is presented in the next chapter.

Chapter 3

Membrane-Driven Folding

This chapter develops the method of Membrane-Driven Folding and presents the equations necessary for successfully implementing this approach.

Section 3.1 presents the principle through which strain of an elastic member can be used to guide many vertices of an origami structure. In Section 3.2, the governing equations relating stretch of two membranes to the geometry of an attached accordion fold are derived. Section 3.3 presents the relationship relating membrane stretch and the rotation of the winding axle driving stretching, while Section 3.4 presents a correction to this relationship which is necessary for membranes of non-negligible thickness. Section 3.5 discusses the compliance required for a sheet of material to be successfully folded using this membrane-driven approach. The Origami Compliance Metric – a means for quickly classifying the compliance of origami sheets – is also presented in this section. Finally, Section 3.6 discusses the sensitivity of the system to errors in the membrane length, winding axle radius, and winding angle.

3.1 Strain as a Means to Drive Folding

In Chapter 2 we demonstrated that all vertices of an origami system should be actuated to ensure maximum control of the folding process. However, for general systems of any reasonable size, assigning an individually-controlled actuator to each vertex is simply not feasible. Consider the 6x6 Miura-Ori lattice pictured in Figure 3.1. The number of vertices scales as $(N+1)(M+1)$, where N and M are the dimensions of the lattice in number of panels; even for this relatively small 6x6 system, the vertex count is 46 (note that 3 would-be vertices are cutoff by the sheet edges). Assigning a dedicated positioning actuator to each vertex is simply not feasible, and another approach is needed.

Here we introduce the concept of *Strain-Driven Folding* as a means of performing the folding of certain systems using a minimal number of actuators. This actuation method considers special origami folds whose vertices share special properties, namely:

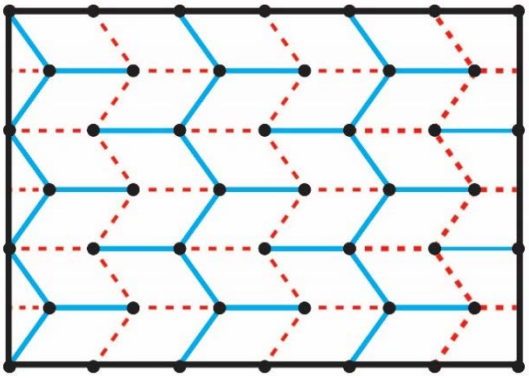

Figure 3.1: Folding map (with vertices) for Miura-Ori pattern

- The positions of any vertex always lies in one of two possible planes; all vertices are contained in two planes.
- The arrangement of vertices on a plane can be thought of as a field of dots, where the final dot field must be related to the original dot field by a stretch, rotation, translation, and/or skew transformation.

Consider the one-dimensional example of a bar in uniaxial compression:

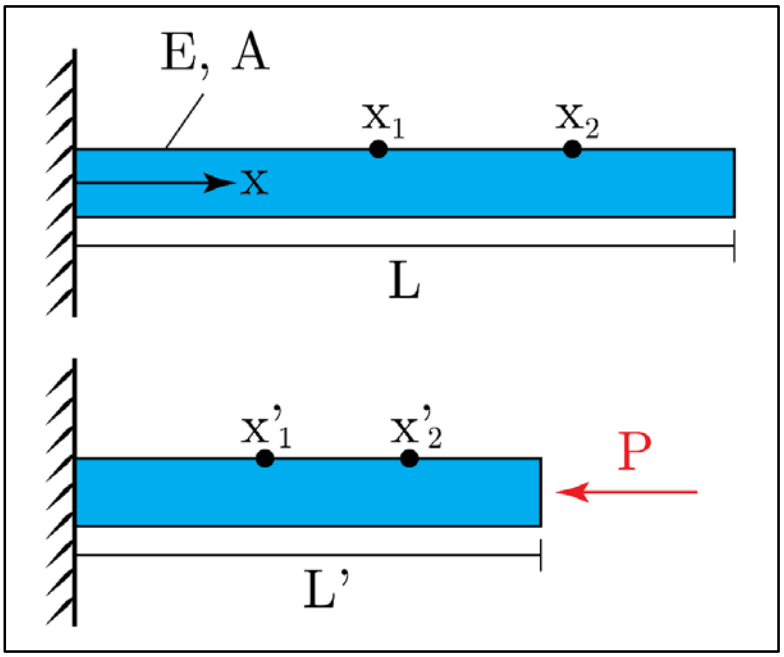

Figure 3.2: Strain of a bar under uniaxial compression

This bar experiences uniform strain, and the x-coordinates of any two points on the bar obey the following relationship (primes indicate post-loading coordinates; values without primes indicate unloaded coordinates):

$$\lambda = \frac{x_2' - x_1'}{x_2 - x_1} \tag{1}$$

Here, λ is the stretch of the bar and may also be expressed as a strain in the bar (ϵ) or a ratio of the initial and final bar lengths:

$$\lambda = \frac{L'}{L} = \epsilon + 1 \tag{2}$$

The uniform compression of the bar is exploited to drive the folding of a mechanism, such as the one placed above the bar in Figure 3.3:

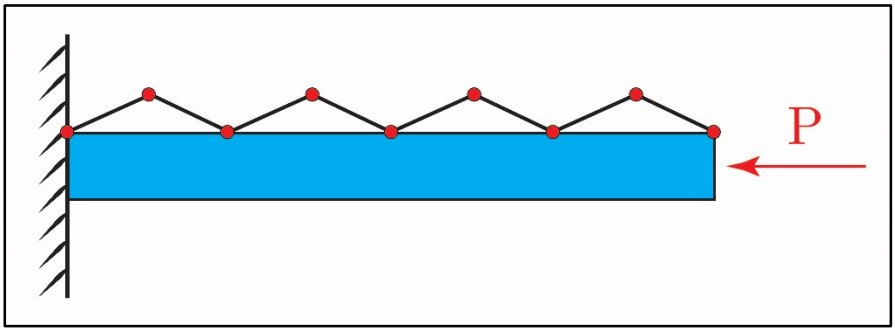

Figure 3.3: Bar with attached folding mechanism

When the bar is compressed, folding of the mechanism atop is induced:

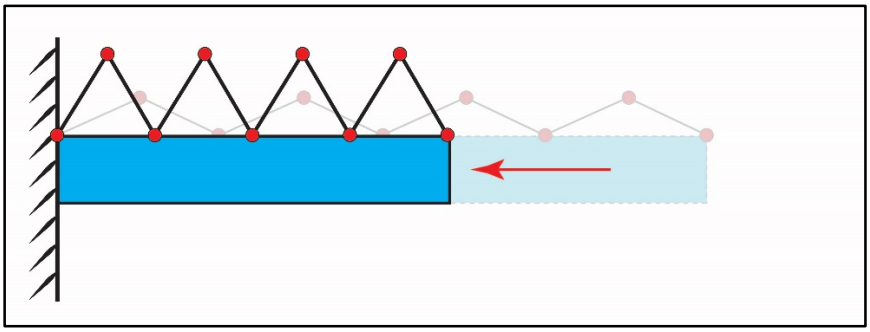

Figure 3.4: Bar with attached folding mechanism, post-loading

If the joints of the mechanism are extremely compliant in comparison to the stiffness of the bar, then the additional work expended to actuate the attached mechanism is negligible and folding of the attached mechanism can be considered *displacement-controlled*. Further, a mechanism containing *any number of simultaneously-actuating linkages* (limited only by the amount of space needed to fix each vertex to the bar) is folded using just one actuator.

The previous example only constrains the bottom vertices, but constraint of all vertices (a potential requirement in the case of a real-world system with compliant linkages) can be achieved by adding a second bar above the structure and allowing it to translate up and down as the mechanism folds:

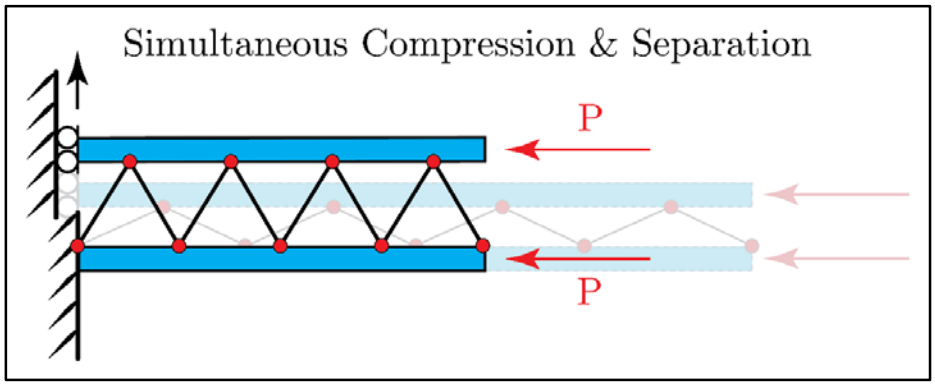

Figure 3.5: Two bars constrain top and bottom vertices of folding mechanism

In this example, we see that all vertices are individually constrained and actuated. Further, the entire system can be controlled using just two actuators – one to drive bar compression, and one to control the vertical position of the upper bar. This is the benefit to this folding approach: fully-controlled actuation of many vertices is achieved using only two actuators and an intermediate stretching medium. We now make four modifications to the example for practical reasons:

Use tension instead of compression: Using a strain-driven folding method relies on very large shape changes in the stretching medium. To avoid the potential for buckling or plastic damage to the bar under compression, we instead adopt the following folding procedure, which uses a pre-stretch to drive the system:

- Stretch the bars in tension *before* attaching the folding mechanism
- Affix the folding mechanism between the bars
- Release tension in a controlled manner to drive folding

Use an elastomer as the bar material: If strain is to be used as the driver for folding, it is important to select a material which is highly extensible, as this allows for the greatest range of actuation for the attached mechanism. It is also desirable that the material is able to fully recover from very high strains so that it can be used multiple times. Finally, it is desirable to pick a material with low stiffness, so large strains may be achieved more easily. Conventional

engineering materials (metals, plastics, ceramics) typically failure at strains of much less than 10% ($\epsilon \ll 0.1$). However, elastomers offer desirable characteristics for this application, boasting high extensibility (500+%) and a comparatively low stiffness.

Make the bar as thin as possible; replace it with a stretching membrane: Significant energy must be expended to stretch the elastomeric stretching medium, and so it is desirable to thin the medium as much as possible; in the limiting case of a frictionless mechanism, the bars can be replaced with infinitely thin membranes. In real systems the thickness of the membrane should be selected by considering (a) the minimum membrane thickness required to maintain an acceptably high membrane-to-mechanism stiffness ratio (such that a displacement-controlled condition is maintained), and (b) the maximum thickness allowable due to force and power limitations of the actuators used for stretching the membrane.

Use winding axles to induce stretch into the actuating membranes: Significant tension forces develop when membranes reach very high strains. The use of axles provides significant mechanical advantage for winding as high winding torque is achieved when the winding axles are small.

Figure 3.6 and Figure 3.7 show the resulting folding process:

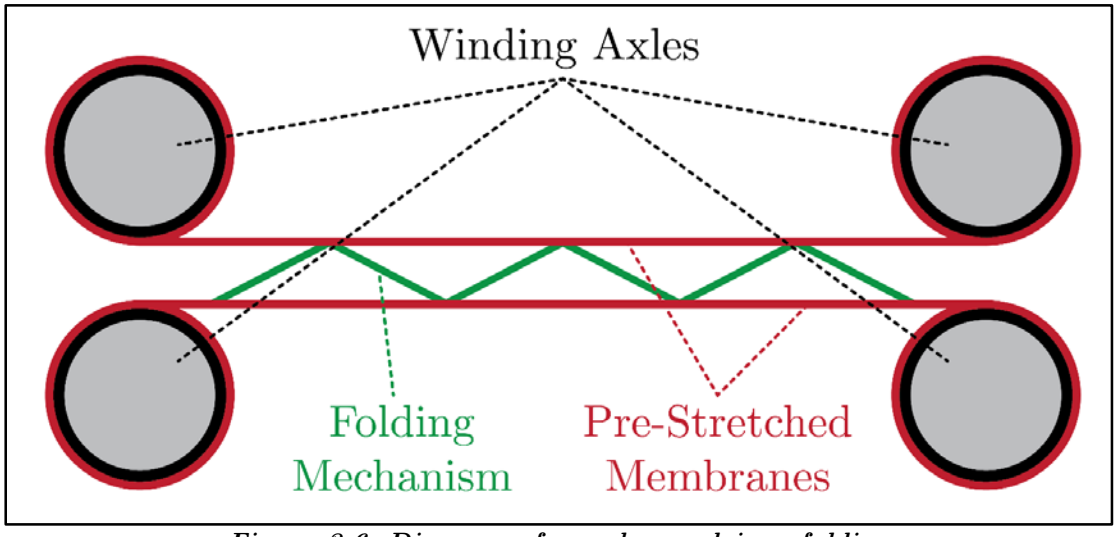

Figure 3.6: Diagram of membrane-driven folding

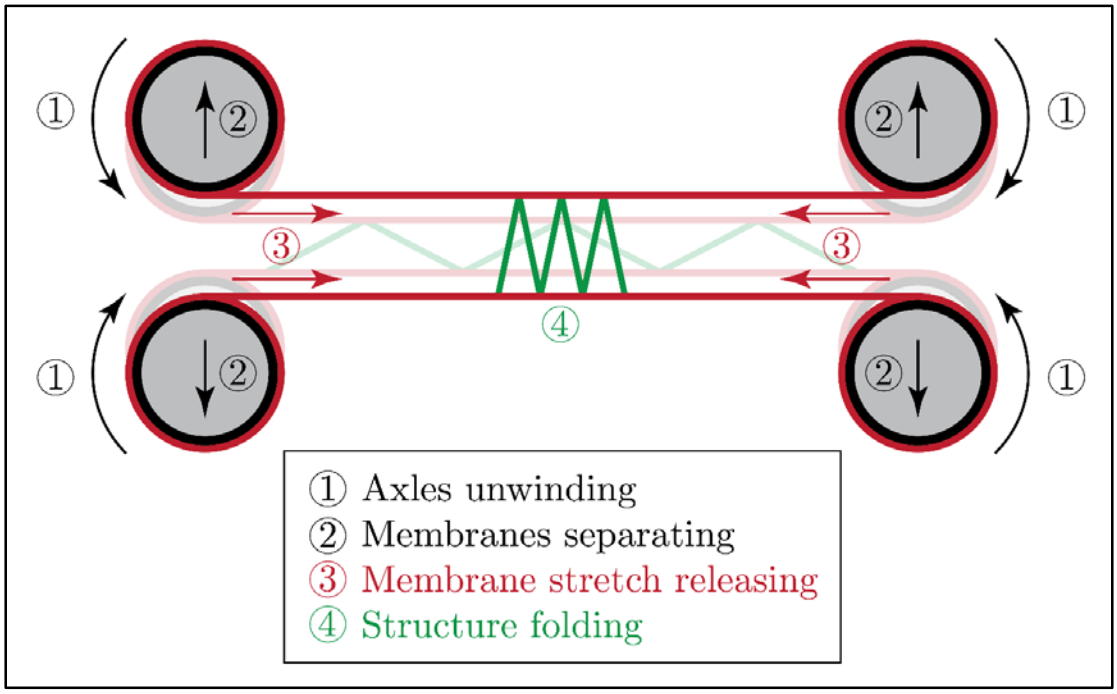

Figure 3.7: Illustration of the membrane-driven folding process
All four actions occur simultaneously

3.2 Kinematic Equations for Folding Lattice

3.2.1 Ideal Accordion Fold

In Figure 3.7 the actuating membranes are simultaneously stretched and separated. The relative rates of the stretch and separation must be controlled to preserve the geometry of the folding mechanism and prevent damage. To determine the relative rate, we first consider the idealized accordion fold:

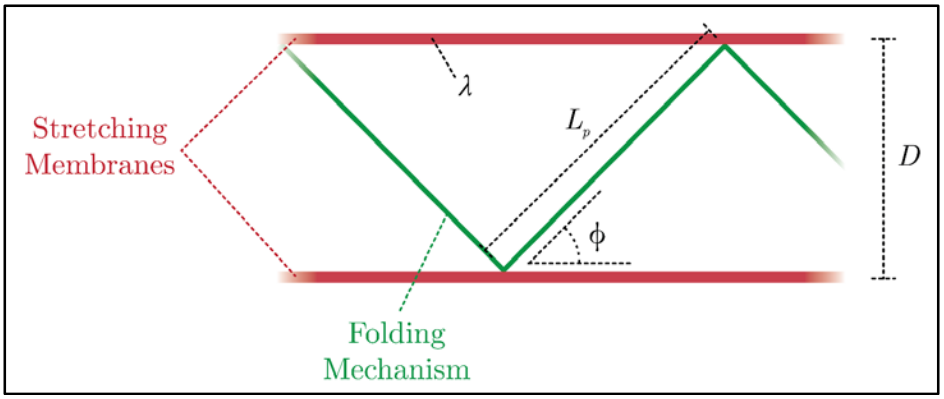

Figure 3.8: Accordion fold: Important variables for kinematic analysis

The geometry of this arrangement is given by:

$$D = L_p \sin(\phi) \tag{3}$$

Here, $D =$ Membrane Separation, $L_p =$ Plate Separation, and $\phi =$ Folding Angle.

We now consider the system at its initial and final configurations. The initial condition is given by a membrane stretch of λ_0 and a fold angle of ϕ_0, while the final condition is given by a membrane stretch of λ_f and a fold angle of ϕ:

$$\frac{\lambda_0}{\lambda_f} = \frac{\cos(\phi_0)}{\cos(\phi)} \tag{4}$$

In general ϕ varies as $0 \leq \phi \leq \frac{\pi}{2}$, where $\phi = 0$ is the flat, unfolded case and $\phi = \frac{\pi}{2}$ is a complete fold (adjacent panels are flat against one another). Setting λ to be the ratio of initial to final stretch $\left(\lambda = \frac{\lambda_0}{\lambda_f}\right)$:

$$\lambda = \frac{\cos(\phi_0)}{\cos(\phi)} \tag{5}$$

ϕ in terms of λ is:

$$\phi = \cos^{-1}\left(\frac{\cos(\phi_0)}{\lambda}\right) \tag{6}$$

We now define the rate of folding to be governed by the rate of change of the folding angle $\left(\frac{d\phi}{dt}\right)$, obtaining expressions for the rates-of-change of the membrane separation and membrane stretch, respectively:

$$\frac{dD}{dt} = L_p \cos(\phi) \frac{d\phi}{dt} \tag{7}$$

$$\frac{d\lambda}{dt} = \tan(\phi) \sec(\phi) \frac{d\phi}{dt} \tag{8}$$

Additionally, the relationship between D and λ obeys:

$$D = L_p \sin\left(\cos^{-1}\left(\frac{\cos(\phi_0)}{\lambda}\right)\right) = L_p \sqrt{1 - \left(\frac{\cos(\phi_0)}{\lambda}\right)^2} \tag{9}$$

This process is intended for applications where 3D structures emerge from 2D surfaces, so we set $\phi_0 = 0$. This simplifies the kinematic equations to become:

Table 1: Kinematic Equations for Accordion Fold		
Membrane Stretch	$\lambda = \frac{1}{\cos(\phi)}$	(10)
Folding Angle	$\phi = \cos^{-1}\left(\frac{1}{\lambda}\right)$	(11)
Membrane Separation Rate	$\frac{dD}{dt} = L_p \cos(\phi) \frac{d\phi}{dt}$	(12)
Stretching Rate	$\frac{d\lambda}{dt} = \tan(\phi)\sec(\phi)\frac{d\phi}{dt}$	(13)
Membrane Separation Distance	$D = L_p\sqrt{1-\left(\frac{1}{\lambda}\right)^2}$	(14)

3.2.2 Modified Accordion Fold

In Section 3.2.1 we consider an ideal accordion fold, where the vertices meet the folding membrane at point contacts. In real systems, however, this sort of point-contact is not possible, and instead a length of the lattice will be fixed to the membrane:

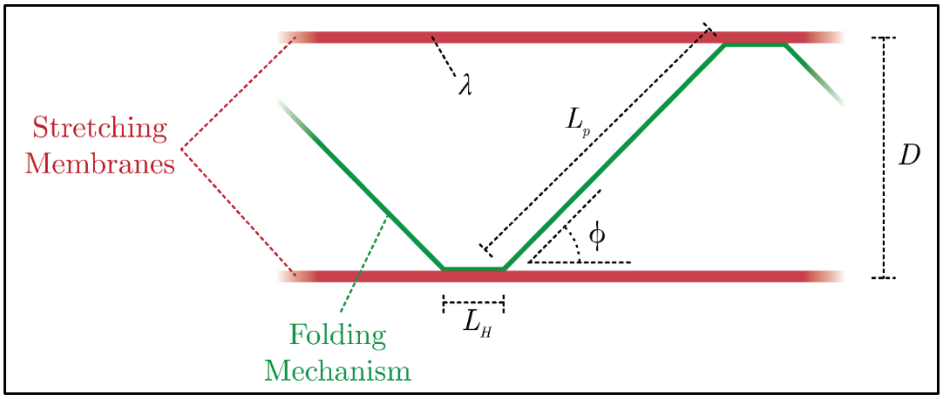

Figure 3.9: Modified accordion fold: Important variables for kinematic analysis
Modified accordion fold includes a short "hinge" length, where the folding structure attaches to the membrane

Now we obtain the following equations:

Table 2: Kinematic Equations for Modified Accordion Fold		
Membrane Stretch	$\lambda = \frac{L_p \cos(\phi_0) + L_H}{L_p \cos(\phi) + L_H}$	(15)
Folding Angle	$\phi = \cos^{-1}\left(\frac{L_p \cos(\phi_0) - \mathrm{L_H}(\lambda - 1)}{L_p \lambda}\right)$	(16)
Membrane Separation Rate	$\frac{dD}{dt} = L_p \cos(\phi) \frac{d\phi}{dt}$	(17)
Stretching Rate	$\frac{d\lambda}{dt} = \frac{L_p \sin(\phi)\left(L_p \cos(\phi_0) + L_H\right)}{\left(L_p \cos(\phi) + L_H\right)^2} \frac{d\phi}{dt}$	(18)
Membrane Separation Distance	$D = L_p \sqrt{1 - \left(\frac{L_p \cos(\phi_0) - \mathrm{L_H}(\lambda - 1)}{L_p \lambda}\right)^2}$	(19)

For the condition $\phi_0 = 0$:

Table 3: Kinematic Equations for Modified Accordion Fold, $\phi_0 = 0$		
Membrane Stretch	$\lambda = \frac{L_p + L_H}{L_p \cos(\phi) + L_H}$	(20)
Folding Angle	$\phi = \cos^{-1}\left(\frac{1}{\lambda} - \frac{L_H}{L_p} + \frac{L_H}{L_p \lambda}\right)$	(21)
Membrane Separation Rate	$\frac{dD}{dt} = L_p \cos(\phi) \frac{d\phi}{dt}$	(22)
Stretching Rate	$\frac{d\lambda}{dt} = \frac{L_p \sin(\phi)\left(L_p + L_H\right)}{\left(L_p \cos(\phi) + L_H\right)^2} \frac{d\phi}{dt}$	(23)
Membrane Separation Distance	$D = L_p \sqrt{1 - \left(\frac{1}{\lambda} - \frac{L_H}{L_p} + \frac{L_H}{L_p \lambda}\right)^2}$	(24)

3.3 Angle-Stretch Relationship of a Winding Axle

The physical folding system discussed in Chapter 4 utilizes winding axles to induce stretch in the folding membrane. Here we derive the relationship between the membrane stretch λ and the winding axle angle θ. If the membrane is stretched using two winding axles operating at the same rotational speed, symmetry dictates that the center of the membrane will remain fixed, while other points will stretch outwards. We examine a portion of the membrane (L') which starts at the symmetry plane and terminates some length before the roller. We consider L_0 to be the width of the system (roller-to-roller distance), and $L'_0 = \frac{L_0}{2}$ to be the half-width:

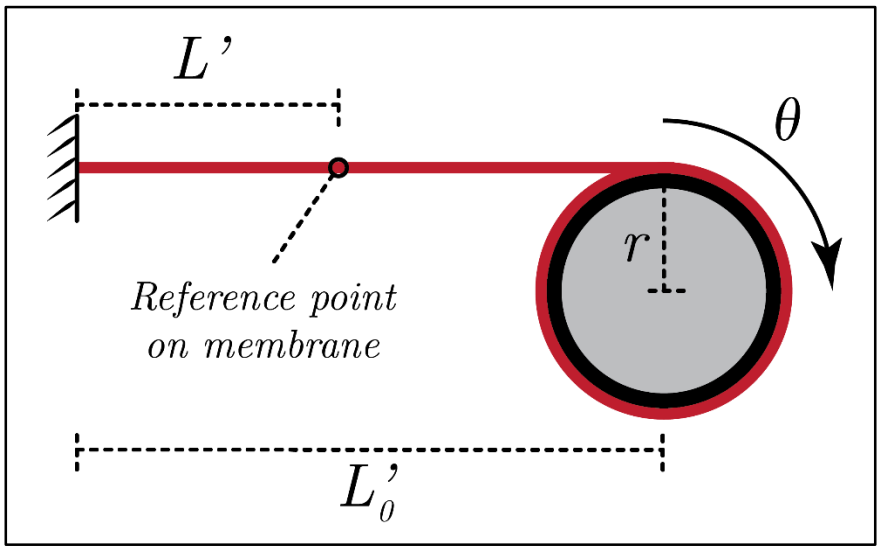

Figure 3.10: System half-width relating membrane stretch to winding axle rotation

The instantaneous rate of change of the membrane length L' with respect to the axle winding angle is:

$$dL' = \frac{rL'}{L'_0} d\theta \tag{25}$$

Where r is the radius of the winding axle. The instantaneous change of stretch in the membrane is:

$$d\lambda = \frac{\lambda}{L'} dL' = \frac{\lambda r}{L'_0} d\theta \tag{26}$$

The differential equation relating stretch to winding rate is given by:

$$\frac{d\lambda}{d\theta} = \frac{\lambda r}{L_0'} \tag{27}$$

This equation assumes a constant value for r, though a correction may need to be applied if the membrane contributes non-negligibly to the axle radius as it winds up. A derivation and discussion of this correction can be found in Section 3.4.

Integrating Equation (27) produces:

$$\lambda = \exp\left(\frac{r}{L_0'}(\theta - \theta_0)\right) \tag{28}$$

Or:

$$\theta = \frac{L_0'}{r}\ln(\lambda) + \theta_0 \tag{29}$$

Recalling that $\lambda = \frac{\lambda_0}{\lambda_f}$, we notice a powerful characteristic of this membrane-driven approach: only the *ratio* of starting to ending stretch dictates the required folding angle θ, and *not the absolute values of* λ_0 *and* λ_f. Conversely, a distinct winding angle θ will produce a stretch ratio of λ and desired folding angle ϕ. This is a very important result because it means that the membranes above and below the folding structure do not need to be exactly calibrated to one another. They can start at two different, arbitrary stretches ($\lambda > 1$ to prevent sagging), but as long as both are wound through the angle θ, the stretch ratio in each will be the same and folding will occur successfully. One need not worry about synchronizing the absolute stretches of the membranes – he or she only needs to ensure that all winding axles operate at the same rate during folding.

3.3.1 Limits to the Angle-Stretch Relationship

The stretching membrane's limit of extensibility will determine the overall performance of the system, i.e. the range geometries it is capable of folding and how well it folds each geometry within that range. Therefore it is important to understand the relationship between the membrane stretch ratio λ, the plate / hinge length ratio L_p/L_H, and the final folding angle ϕ. Using Equation (21), we map λ vs ϕ for a range of plate / hinge length ratios, producing Figure 3.11:

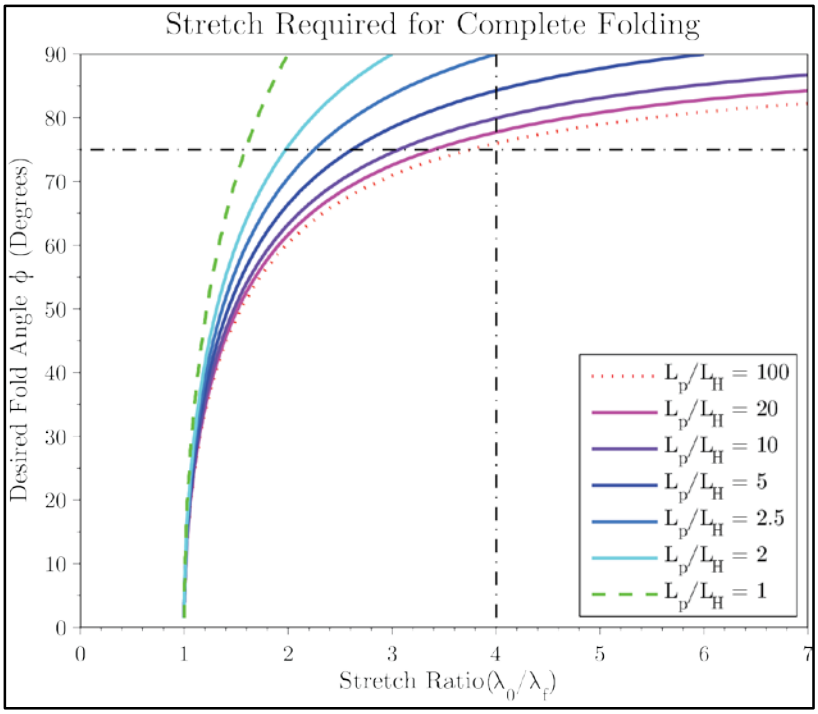

Figure 3.11: Relationship between stretch ratio and folding angle

For small values of L_p/L_H, where the hinge and plate lengths are roughly equal, only small stretch ratios are required. If $L_p = L_H$, the membrane must only actuate between $1 \leq \lambda \leq 2$ to achieve the full range of folding angles. As the hinge length decreases ($L_H \to 0$, $L_p/L_H \to \infty$), the stretch needed to achieve a fold angle of $\phi = 90^o$ approaches infinity ($\lambda = \infty$). Obviously no real system can achieve an infinite stretch ratio, but it is possible to achieve near-complete folding angles with real membranes, even for large plate-hinge ratios. We see that a stretch ratio of $\lambda = 4$ is sufficient to drive the folding angle past 75^o for most systems, even those with very large plate-hinge ratios. Many elastomers are capable of achieving stretches of 5 or more, and so a system capable of folding these geometries is entirely feasible.

3.4 Corrected Radius of the Winding Axle

As the winding axles take up the stretching membrane, the thickness of the membrane will contribute to the radius of the axles, leading to error in the winding angle / stretch relationship. In this section we derive a differential equation describing the corrected relationship between θ and λ, and present an approximate correction for empirical use.

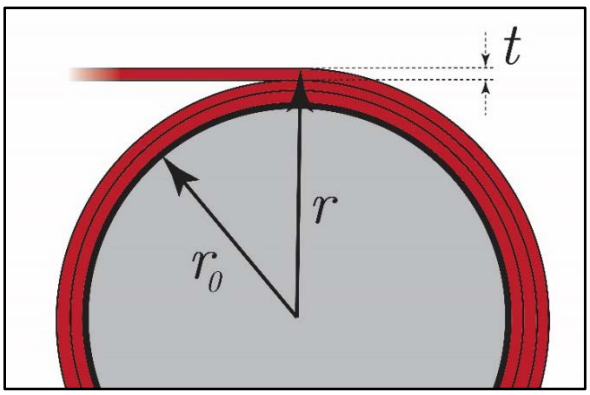

Figure 3.12: Contribution of membrane thickness to winding axle radius

3.4.1 Exact Solution for Radius Correction

The large-deformation relationship between membrane strain in the actuated direction (ϵ_λ), and strain in the thickness direction (ϵ_t), is:

$$\epsilon_t = -1 + (1 + \epsilon_\lambda)^{-\nu} \tag{30}$$

(A derivation of this relationship can be found in Appendix A)

Substituting $\lambda_t = \epsilon_t + 1$ and $\lambda = \epsilon_\lambda + 1$:

$$\lambda_t = \lambda^{-\nu} \tag{31}$$

The relationship between membrane thickness and stretch in the actuated direction is:

$$t = t_0 \lambda^{-\nu} \tag{32}$$

The differential equation relating change in axle radius to change in winding angle is:

$$\frac{dr}{d\theta} = \frac{t_0 \lambda^{-\nu}}{2\pi} \tag{33}$$

Integration produces:

$$r(\theta) = \frac{t_0}{2\pi}\left(\int_{\theta_0}^{\theta} \lambda^{-\nu} d\theta\right) + r_0 \tag{34}$$

Substitution into Equation (27) gives:

$$\frac{d\lambda}{d\theta} = \frac{\lambda t_0}{2L_0{}'\pi}\left(\int_{\theta_0}^{\theta} \lambda^{-\nu} d\theta\right) + \frac{r_0 \lambda}{L_0{}'} \tag{35}$$

Solving this equation would produce the radius-corrected relationship between λ and θ. However, because λ is itself a function of θ, the method of solution for this differential equation would require an iterative approach. An approximation is presented in the following section.

3.4.2 Approximation of Radius Correction

The total change in winding axle radius can be approximated by modifying Equation (33):

$$\Delta r \approx \frac{t_0 \lambda^{-\nu}}{2\pi} \Delta\theta \tag{36}$$

Here, the pre-corrected values for λ and $\Delta\theta$ $\left(\Delta\theta = \theta_f - \theta_0\right)$ from Equations (28) and (29) are used. This approximation results in a slight overestimate of Δr for two reasons: (a) the initial stretch ratio λ is used (rather than the average during the process), and (b) the $\Delta\theta$ calculated here will be greater than the corrected $\Delta\theta$ due to the increase in effective winding axle radius. Due to this overestimation, the true final radius r_f will be bounded by $(r_0) < \left(r_f\right) < (r_0 + \Delta r)$. An average radius during the stretching process is approximated as the arithmetic mean of the initial and final winding axle radii:

$$r_{avg} \approx \frac{r_0 + (r_0 + \Delta r)}{2} = r_0 + \frac{t_0 \lambda^{-\nu}}{4\pi} \Delta\theta \tag{37}$$

This corrected radius value r_{avg} is then be substituted for r in Equations (28) and (29). The need for a radius correction factor depends on the ratio:

$$\frac{\Delta r}{r_0} = \frac{t_0 \lambda^{-\nu}}{2\pi r_0} \Delta\theta \tag{38}$$

For low values of this ratio $\left(\frac{\Delta r}{r_0} < 0.01\right)$, a correction factor may not be needed, as the change in axle radius is negligible. Low values are achieved by increasing the roller size (which will increase the value, r_0, as well as lower the total angle of rotation, $\Delta\theta$) and decreasing the membrane thickness.

3.5 Soft Origami

Origami structures conventionally rely on mechanism-like hinge features for mobility. Creases are used in paper origami, while bushings, bearings, or living-hinges are often used in load-bearing structures. Mechanisms such as these are excellent for restricting the degrees of freedom for individual hinges, but these dedicated folding features introduce inherent complexity into the system. At least one such folding feature is needed for each hinge, requiring additional machining, fabrication, and/or assembly to produce the final structure. Moreover, each individual hinge introduces an additional potential point-of-failure for the system as a whole. For applications

such as tissue scaffolding, where the origami lattice might involve thousands or tens-of-thousands of micro-scale hinges, this type of approach is clearly not feasible.

The simplest possible folding structure is a thin, uniform sheet. If the sheet is sufficiently compliant, it will be capable of assuming extreme deformations without the need for creases or other dedicated folding features. An analogy may be made to bedsheets, which do not have any hinges, but instead rely on the user (external constraints) to impose folds and dictate the sheet's final geometry. The bedsheet is an example of an extremely compliant origami structure. This class of extremely compliant structures – which we term "Soft Origami" – remains unexplored by other researchers in the field, as existing work only contemplates rigid or semi-rigid systems.

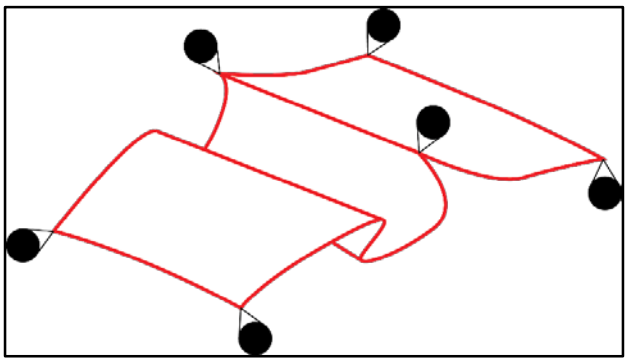

Figure 3.13: Idealized Soft Origami sheet, capable of achieving any curvature

3.5.1 Qualities of Soft Origami

An ideal Soft Origami structure is considered to be a *perfectly compliant* sheet – it may bend (and to a limited extent, stretch) to assume any imposed curvature. Further, because the structure has no load-bearing capability (it buckles under its own weight), its degrees of freedom are fixed entirely by its external constraints. Thus, the sheet may bend and fold with no need for specialized hinge features.

Under this definition, an ideal Soft Origami system may achieve bends with zero radius of curvature. For real systems, we define Soft Origami to refer to systems capable of achieving *negligible* radii of curvature under bending.

3.5.2 Derivation of the Origami Compliance Metric (OCM)

For engineering and design purposes it is important to use a metric for quantifying how closely a real structure mimics ideal Soft Origami. To this end the Origami Compliance Metric (OCM) has been created. It assumes the following:

1. The origami sheet is uniformly thick and continuous. All panels are identical in geometry and material properties.

2. The continuum limit of the sheet material is not approached (the length-scale over which material properties vary is extremely small when compared with the panel size).
3. The sheet material is isotropic and linear-elastic.
4. The sheet material exhibits a well-defined Young's Modulus (E) and failure strength (σ_f).
5. While total tip-to-tip deflection of the sheet may be large, local deformations are small and anticlastic deformations are negligible.

To achieve the characteristic OCM value of an origami sheet / pattern pair, a single panel from the origami pattern is extracted and modeled as a rectangular prismatic beam of relatively great width. The shortest side of the panel is considered, as this produces the most conservative OCM value. A uniform curvature is then imposed on the beam by applying moments to its tips:

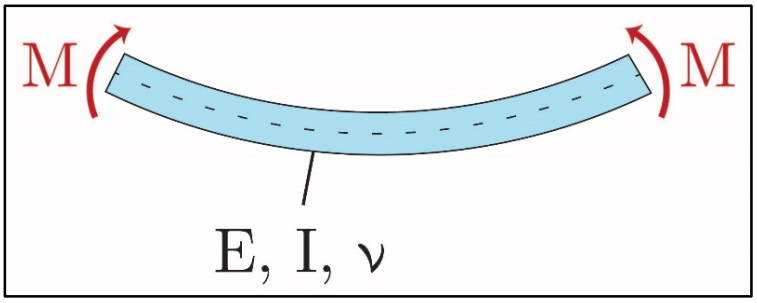

Figure 3.14: Wide beam under moment loading

The classic moment-curvature relation for this beam is:

$$\kappa = \frac{M(1-\nu^2)}{EI} \tag{39}$$

$\boldsymbol{M}$ = Imposed Moment $\quad$ $\boldsymbol{I}$ = Bending Moment of Inertia
$\boldsymbol{E}$ = Young's Modulus $\quad$ $\boldsymbol{\kappa}$ = Beam Curvature
$\boldsymbol{\nu}$ = Poisson's Ratio

The bending stress in the beam (σ_b) varies only with distance from the neutral axis:

$$\sigma_b = \frac{Mz}{I} \tag{40}$$

$\boldsymbol{\sigma_b}$ = Bending Stress $\quad$ $\boldsymbol{z}$ = Distance from neutral axis

Or, expressed in terms of the imposed curvature:

$$\sigma_b = \frac{E\kappa z}{1-\nu^2} \tag{41}$$

In this pure-bending case, the beam can be said to fail when the maximum stress observed reaches or exceeds the material's failure stress (σ_f). For this value, Ashby recommends choosing the yield strength for metals and polymers, the modulus of rupture for ceramics, the tear strength for elastomers, and the tensile strength for composites and woods [37]. At this time we recall assumptions 3 and 4 from before (the material is linear-elastic and exhibits a well-defined Young's Modulus, E, and failure strength, σ_f) and remember that the OCM will lose predictive power as the material strays from these assumptions.

The curvature at which peak bending stress occurs (the maximum attainable curvature for the beam before failure) is:

$$\kappa = \frac{2\sigma_f(1-\nu^2)}{Et} \tag{42}$$

The total angle through which the beam curves from tip-to-tip is:

$$\theta = \kappa L \tag{43}$$

When two adjacent folding panels meet, the relative angle between then is $\theta = \pi$, and this value is substituted to produce:

$$L_{180} = \frac{\pi E t}{2\sigma_f(1-\nu^2)} \tag{44}$$

L_{180} is the minimum panel length necessary to achieve a 180^o bend from the beam without inducing material failure. If a panel has thickness, t, Young's Modulus, E, failure strength, σ_f, and is significantly larger than L_{180}, the panel is capable of achieving large curvatures. A panel with identical material properties and thickness but a length significantly smaller than L_{180} will be unable to achieve large bending deflections without failing. The Origami Compliance Metric (OCM) is obtained when L_{180} is normalized by the panel length L:

$$OCM = \frac{L_{180}}{L} = \frac{\pi E t}{2\sigma_f L(1-\nu^2)} \tag{45}$$

A very large OCM value means many panel lengths are needed to achieve a 180^o bend, while a very small OCM value means a single panel can achieve a 180^o bend using only a fraction of its length.

3.5.3 Origami Compliance Regimes

The behavior of a structure analyzed using the OCM method is described by one of three possible modes:

Soft (OCM $\ll 1$):

The sheet is capable of extreme deflections under bending and will readily conform to externally-imposed displacements.

Mechanism-Reliant (OCM $\gg 1$):

The sheet has little tolerance for large deflections and imposing these deflections will result in significant material damage or catastrophic failure. Structures operating in this regime must incorporate dedicated folding features (such as hinges) if folding is to occur.

Hybrid (OCM $\approx$ 1):

The sheet is capable of moderately large deflections but a significant fraction of each panel must bend to accommodate global shape changes. The sheet will not readily conform to all arbitrary shape changes and may fail if large deflections are imposed. Hybrid Origami may require hinges or other folding features to achieve sufficient performance.

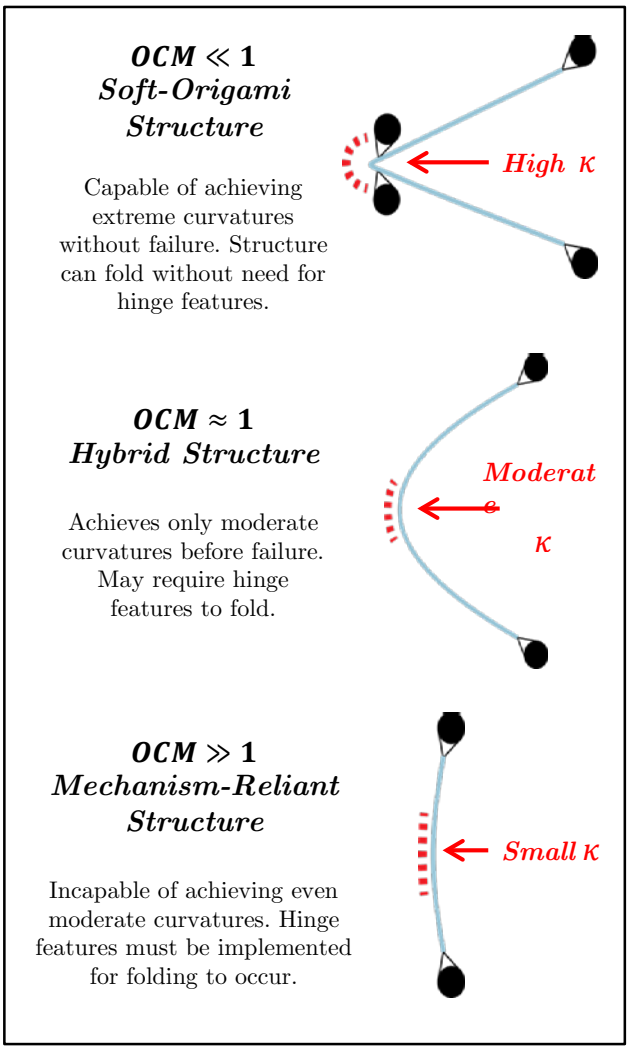

Figure 3.15: Origami Compliance regimes

Patterns for which all panels are identical (such as the accordion and Miura-Ori) will exhibit a single OCM value if the folding sheet is uniform. However, many origami patterns contain dissimilar panels and/or may require a sheet of varying thickness, thereby exhibiting different characteristic OCM values across their surface. In this case, the minimum and maximum OCM values for all panels can be obtained, giving a range across which the structure as a whole behaves. Even if OCM values differ, if all values remain strictly within one regime, the structure

as a whole can be said to operate globally within that regime. Structures spanning OCM regimes will not behave uniformly and are not considered here.

Table 4: Example OCM Values

	Plastic Wrap (HDPE)	Sheet Metal (1018 Steel)
$E\ (GPa)$	1	205
$t\ (mm)$	0.0125	1.5
$\sigma_f\ (MPa)$	20	345
$L\ (mm)$	25	25
ν	0.40	0.28
OCM	**0.047**	**61**

3.5.4 OCM Limitations

Assumption 5, the negligibility of anticlastic deformations, states that the local radius of curvature in a beam is large in comparison to the thickness of the material. The ratio of radius of curvature to beam thickness can be expressed as:

$$\frac{\rho_{180}}{t} = \frac{E}{2\sigma_f} \tag{46}$$

For most engineering materials the ratio of Young's Modulus (E) to failure strength (σ_f) exceeds 10:1. For most metals, plastics, and many polymers, it meets or exceeds 100:1. For materials such as these Assumption 5 is valid. Many elastomers exhibit $E{:}\,\sigma_f$ ratios of less than 1:1, a condition where Assumption 5 is no longer valid. In this case the designer should proceed with caution.

3.5.5 Constraining Soft Origami using Tension

Ideal Soft Origami systems lack any bending resistance and so cannot support compressive loads (of any magnitude) without buckling. This is demonstrated using the Rayleigh-Ritz buckling quotient, a result of the principle of virtual work. The buckling quotient for a beam of relatively great width is [38]:

$$N = \frac{EI}{1-\nu^2}\frac{\int_0^L \delta w'' \delta w'' dx}{\int_0^L \delta w' \delta w' dx} \tag{47}$$

$\boldsymbol{N}$ = Critical buckling load $\quad$ $\boldsymbol{I}$ = Bending Moment of Inertia
$\boldsymbol{E}$ = Young's Modulus $\quad$ $\boldsymbol{L}$ = Beam Length
$\boldsymbol{\nu}$ = Poisson's Ratio

Here, w is the characteristic shape function associated with buckling deflection. The variables $\delta w'$ and $\delta w''$ are the first and second variations of the shape function, respectively. The zero bending stiffness property of ideal Soft Origami corresponds to moment of inertia (I) of zero, and so the net compressive load which the structure can sustain (N) is also zero.

To constrain real Soft Origami sheets and prevent their buckling under self-weight, a small net tension may be applied between vertices. In the framework of membrane-driven folding this is easily achieved by modifying the membrane separation (D) using a stretch factor (k_D) to achieve a corrected value for membrane separation (D_c):

$$D_c = D(k_D + 1) \tag{48}$$

The parameter k_D represents the additional tensile strain induced in the folding sheet to counteract buckling; a value $k_D = 0.001$ represents 0.1% induced tensile strain. Note that the forces producing this strain act out-of-plane to the tension in the stretching membranes. If the membranes are constrained only at their ends (by their winding axles), these out-of-plane tensile forces will cause deformations in the membranes, introducing non-uniform and undesired error into the system. If precise control of these errors is critical, an additional, planar constraint for each membrane (i.e. a vacuum chuck lubricated to allow sliding) may be required.

3.6 Error Sensitivity

This section investigates the effect of assembly and fabrication errors on the folding performance of a unit cell, which is defined here as the percent error in the folding angle ϕ. Three types of errors in system fabrication are considered and each is assessed by its effect on the relative error of the folding angle $\Delta\phi/\phi$. The chain rule is used for each of the three errors in order to find the relative folding error:

$$\frac{\Delta\phi}{\phi} \approx \frac{d\phi}{d\lambda}\frac{d\lambda}{dc}\frac{1}{\phi}\Delta c \tag{49}$$

Here, c is used to as a placeholder for the variable whose error is propagated through. The following three errors are considered:

1. Error in L_0', the effective length between the winding axles
2. Error in r, the radius of the winding axles
3. Error in θ, the winding angle of the winding axles

In all calculations, values and maximum uncertainties from the prototype system are used ($r = 0.300"$, $L_0' = 8.0"$, $\Delta r = 0.005"$, $\Delta L'_0 = 0.05"$, $\Delta\theta = 0.1$).

Table 5 shows the effect of various errors (in $L_0', \theta,$ and r) on the unit-cell folding angle. In each case, the equation for stretch error $\Delta\lambda$ is provided, which is applied to Equation (49) to produce the respective plot for relative error.

For axle separation and axle radius errors, the percent folding angle error increases as folding proceeds, with errors rapidly rising after $\phi = 1.1$ radians. Lower plate-hinge ratios produce smaller errors of 1-4% for more complete folding, while high plate-hinge ratios may produce higher errors (approaching 10%). In the case of the high plate-hinge ratio $\left(\frac{L_p}{L_H} = 100\right)$, folding was not allowed to proceed past a stretch ratio of $\lambda = 10$ as stretches greater than this are not practical (the stretch cap appears as a green circle).

Axle rotation errors contribute significant error for very small folding angles (where the winding angle error is of the same order as the winding angle itself). The error quickly drops off past a folding angle of $\phi = 0.1$ radians, after which the error remains well below 1%.

Table 5: Effect of Actuation Errors on Folding Angle

Error Type	Stretch Error	Relative Folding Error
Axle Separation $(\Delta L_0')$	$\frac{d\lambda}{dL_0'} \approx \frac{1}{L_0'} \ln(\lambda)\,\lambda$ (50)	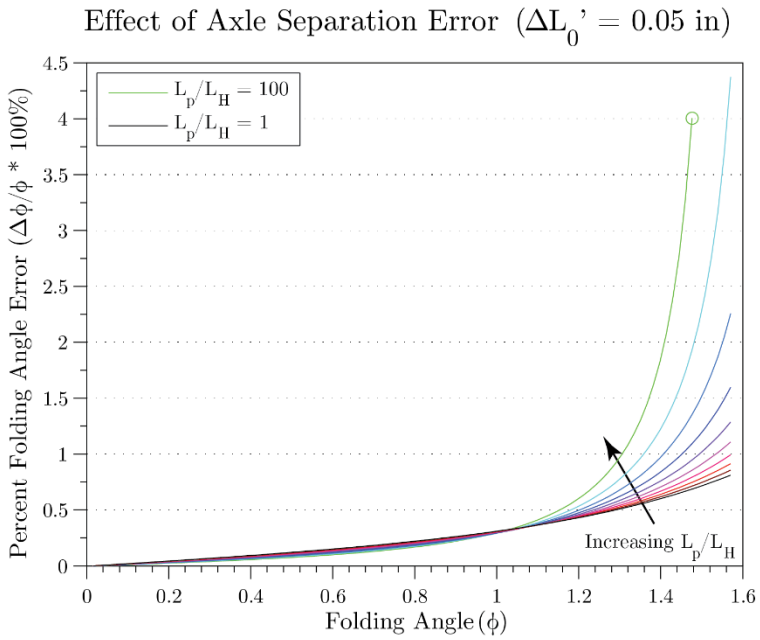

Axle Radius (Δr)

$$\frac{d\lambda}{dr} \approx \frac{1}{r}\ln(\lambda)\,\lambda \quad (51)$$

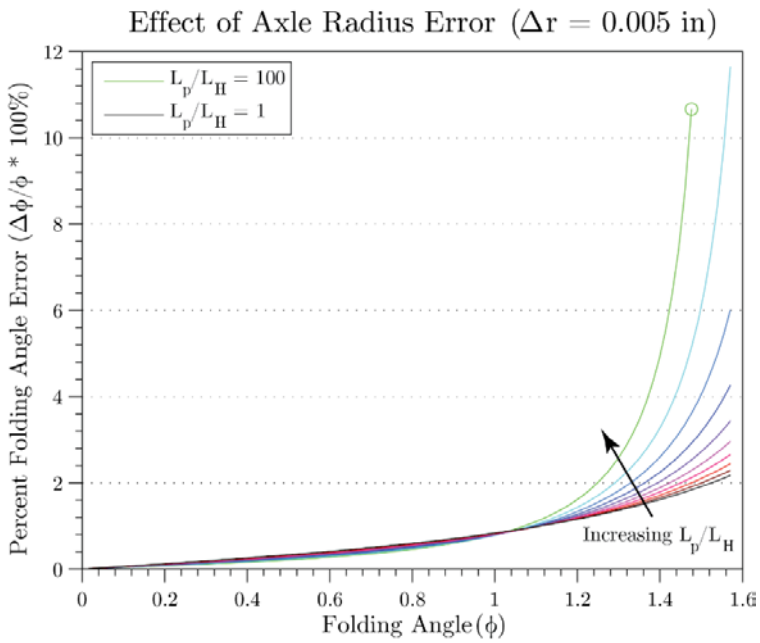

Axle Rotation ($\Delta\theta$)

$$\frac{d\lambda}{d\theta} \approx \frac{r}{L_0'}\lambda \quad (52)$$

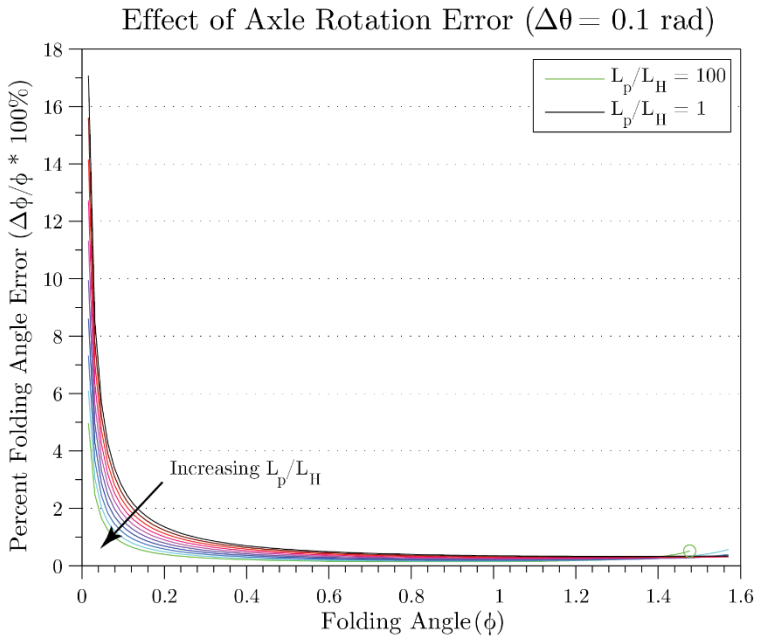

Chapter 4

Design of a Membrane-Driven Folding System

This Chapter presents the design of a prototype membrane-driven folding system, including mechanical, electronic, and software elements. Functional Requirements for the system are presented in Section 4.1. In Section 4.2, the design of mechanical subsystems and selection of key components is discussed. Section 4.3 presents the electronics and LabVIEW control system used to operate the system.

4.1 Functional Requirements

The functional requirements for the prototype folding system are given in Table 6:

Table 6: Functional Requirements for Prototype Machine

Property	Value	Units
Folding Area	>150x150	mm^2
Vertical Travel	>75	mm
Membrane Thickness	<0.3	mm
Tension Force	>2500	N
Stretch Resolution	<0.0005	--
Vertical Resolution	<0.1	mm
Dimensional Stability	<1	*% per 45 min*

The prototype machine is intended to fold patterns with panels of length $25\,mm$, though the machine is designed to accommodate panel lengths ranging from 10-50 mm. Explanations for the functional requirements are as follows:

- **Folding Area:** The maximum sheet size the machine can fold. Side-length of folding area was chosen to be a minimum of 6x the target panel length.

- **Vertical Travel:** The machine's vertical range-of-travel, allowing for separation of the upper and lower membranes. Chosen to be to 3x the maximum panel length.
- **Membrane Thickness:** The maximum membrane thickness the system is designed accommodate.
- **Tension Force:** The maximum tension the winding axles can exert on the folding membranes. Equal to twice the tensile strength for the thickest planned membranes ($0.3\ mm$).
- **Stretch Resolution**: The resolution of the positioning system controlling incremental changes in membrane stretch. The minimum stretch increment should be no more than 0.05% of the current stretch value.
- **Vertical Resolution**: The minimum resolvable increment for vertical translation of the upper subassembly.
- **Dimensional Stability**: The stretch achieved by the machine should be dimensionally stable over a period of 45 minutes, which is approximately the length of one full test.

4.2 Mechanical Design

4.2.1 Design Overview

The prototype membrane-driven folding machine is composed of two major subassemblies: the upper subassembly and the lower subassembly. The upper and lower subassemblies mirror one another in form and function. Each consists of an 80/20 frame, two winding axles, two winding motors, two central rollers, and mating components for connecting the subassemblies. The upper and lower subassemblies are shown in Figure 4.1.

a) Upper Subassembly

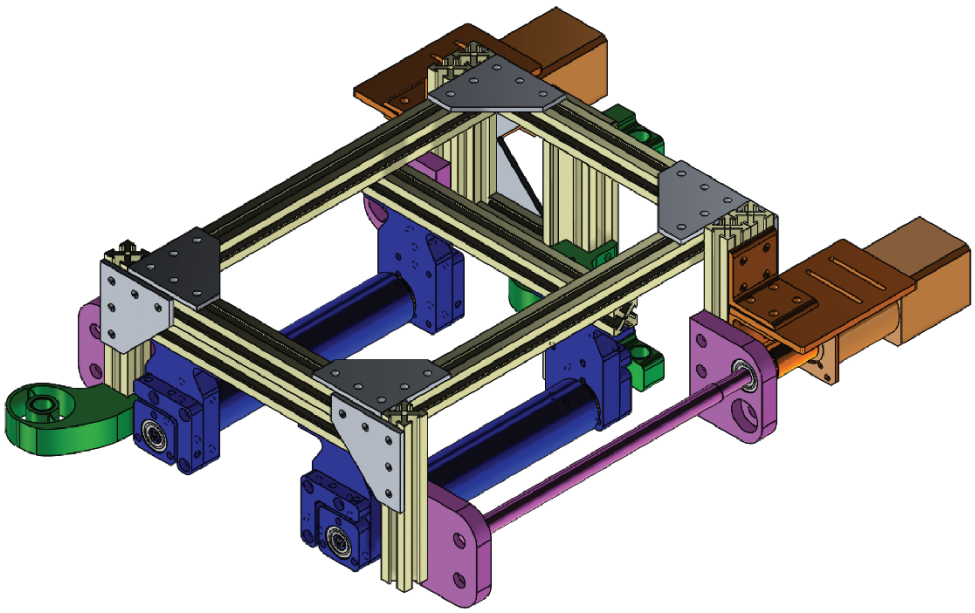

b) Lower Subassembly

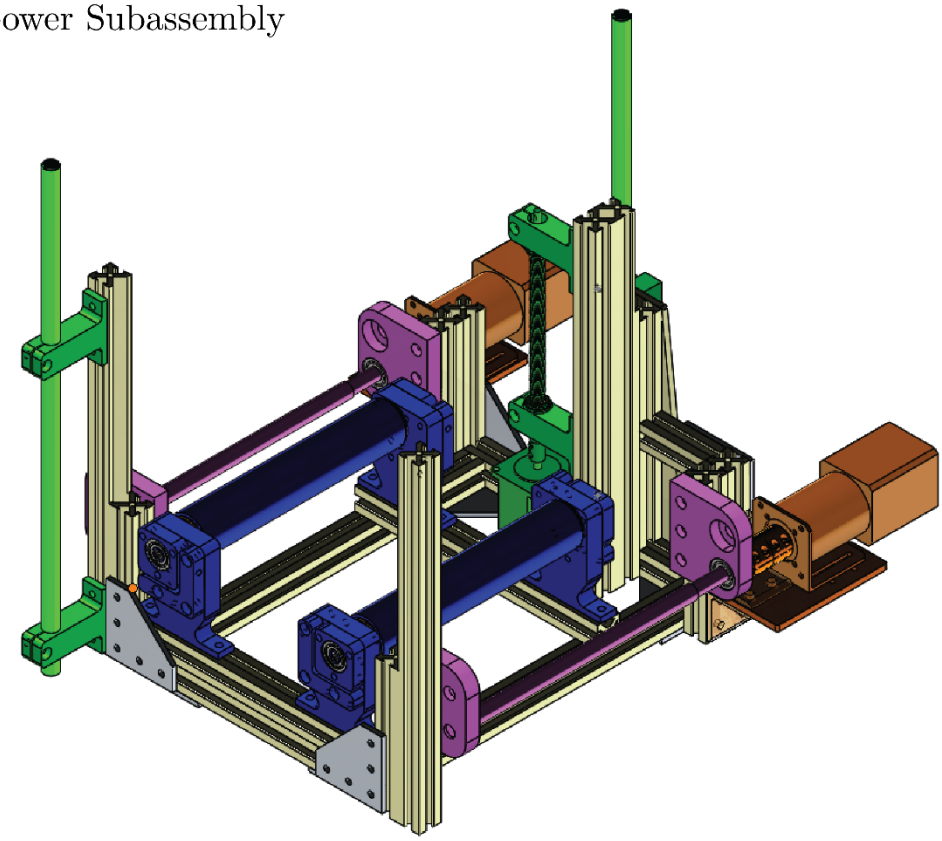

Figure 4.1: Upper and Lower Subassemblies

Subsystems are color-coded and discussed in the coming sections

4.2.2 80/20 Frame

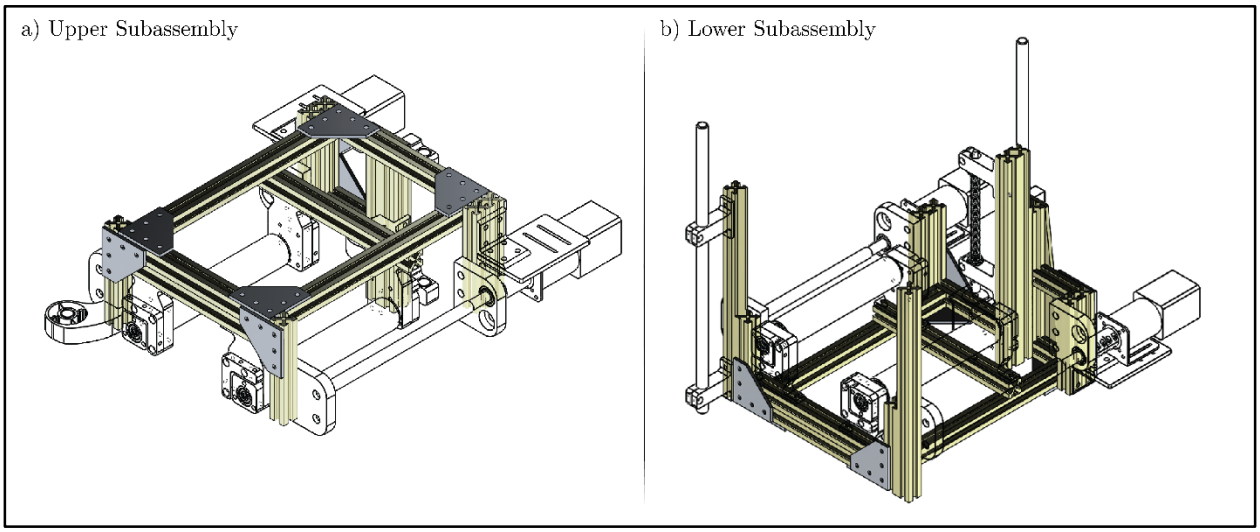

Figure 4.2: 80/20 frame components in upper and lower subassemblies

Extruded 80/20 was selected for construction of the system's frame. This significantly decreased fabrication time and overall cost. While a solid frame would have offered much greater stiffness, deflections of the system are repeatable and can be eliminated as a source of error through calibration of the computer-controlled folding algorithm. Ultimately, the modularity of 80/20 ultimate made it the best choice for this prototype.

4.2.3 Winding Axles

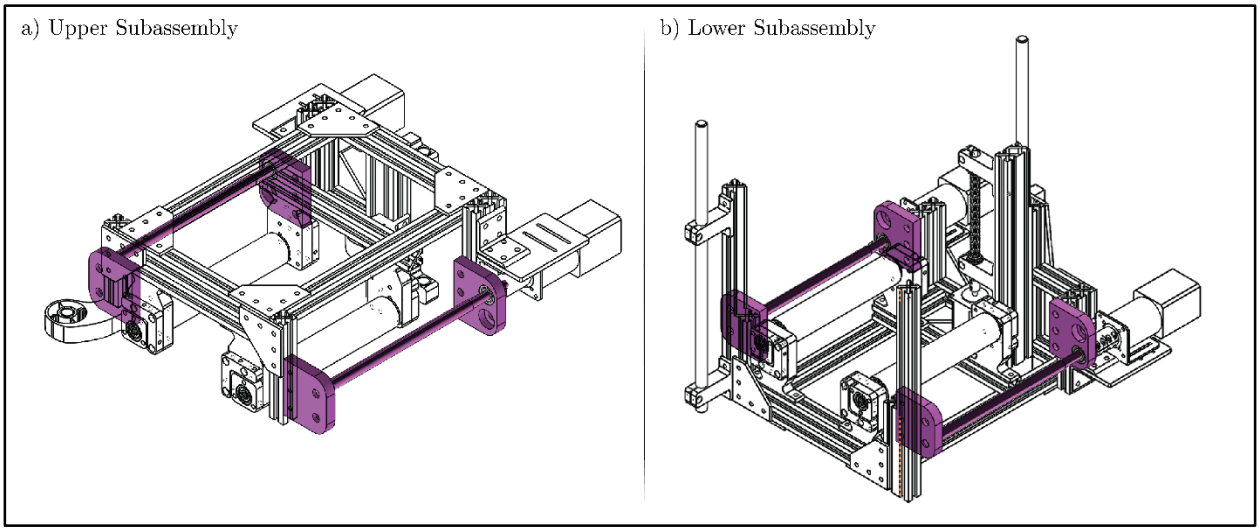

Figure 4.3: Winding axle components in the upper and lower subassemblies

The four winding axles induce and release strain from the actuating membranes via torque provided by stepper motors. The diameter of each winding axle for the prototype machine is $15.24\,mm$ ($0.600" \pm 0.002"$). All are machined from 6061-T6 aluminum, which offers significant rigidity and hardness advantages over plastics while being lighter and more easily machinable than steel. The stepper motor selected in Section 4.2.4 is rated for a holding torque of $40\,Nm$ and has 9331 steps per revolution of the output shaft (owing to the $46\frac{82}{125}:1$ gear ratio from the attached planetary gearbox). Coupled with the winding axle radius of $7.62\,mm$ ($0.300"$), the functional requirements for Tension Force and Stretch Resolution are well exceeded:

$$\text{Tension Force} = T/r = \frac{40\,Nm}{0.00762\,m} \approx 5250\,N \tag{53}$$

$$\text{Stretch Resolution} = \frac{r}{L_0'}\frac{2\pi}{N_{rev}} \approx 6.1 * 10^{-6} \tag{54}$$

Each winding axle is mounted on two high-load ball bearings (with rated Dynamic Load Capacity of $5330\,N$ per bearing) using an RC3 precision running fit to allow for disassembly and reconfiguration. Each axle is then mated to its driving stepper motor via a keyed shaft coupling. The shaft coupling constrains the translational and rotational degrees of freedom in the axial direction, while the bearings constrain the remaining four degrees of freedom.

4.2.4 Motor Selection

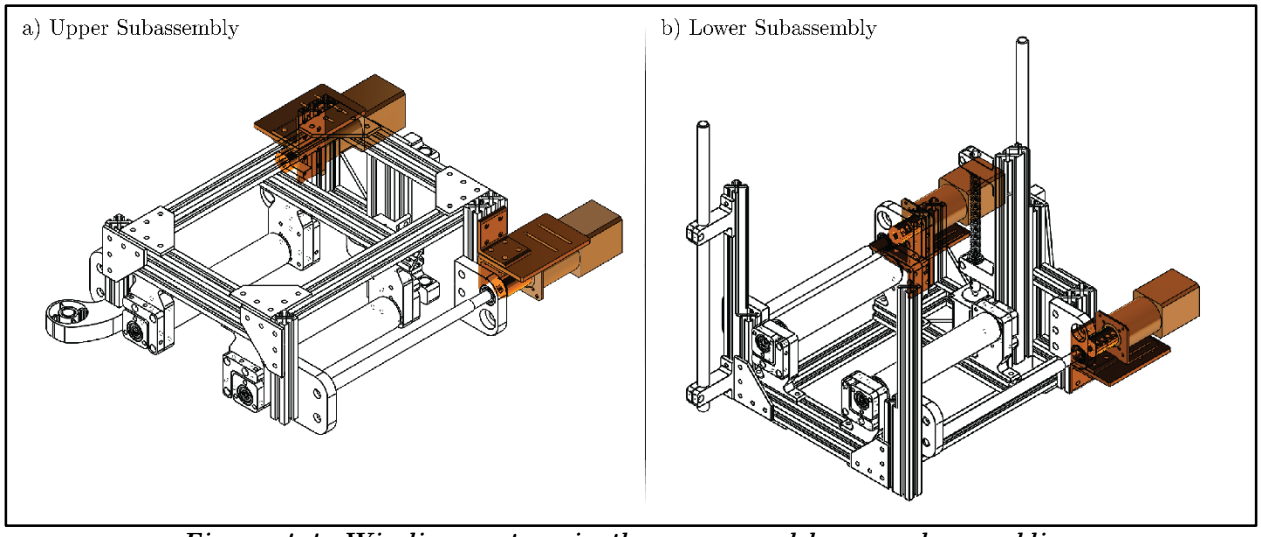

Figure 4.4: Winding motors in the upper and lower subassemblies

Three motor types (geared DC, geared continuous servo, and geared stepper) were considered for driving the winding axles. Rated torque and weight were of primary importance; the rated torque must be high enough to meet the functional requirement on Tension Force, while

weight must be low enough to allow for vertical actuation of the Upper Membrane Assembly. Candidate motors for each type are presented in Table 7.

Table 7: Pugh Table for Selection of Winding Motors

	Geared DC	**Geared Continuous Servo**	**Geared Stepper**
Make	Maxon Motor AG	McLennan Servo Supplies Ltd.	OMC StepperOnline
Model	RE 65 (Motor) GP 52 C (Gearbox)	M66CE (Motor) IP57-M03 (Gearbox)	23HS30-2804S-PG47
Torque Rating	30 Nm	20 Nm	**40 Nm**
Weight	3 kg	3 kg	**2 kg**
Feedback Control	Yes	**No**	**No**
Positioning Accuracy	High	High	**Very High**
Max Speed (w/ gearbox)	**Low (<100 RPM)**	Very Low (10 RPM)	**Low (<100 RPM)**
Cost per unit	High (>$1000)	Medium ($500)	**Low (<$100)**

The geared stepper motor from OMC StepperOnline was the clear choice. The motor (a NEMA-23 stepper) produces high torque from a low-weight package, requires no feedback control for high positioning accuracy, and costs less than $100 per unit.

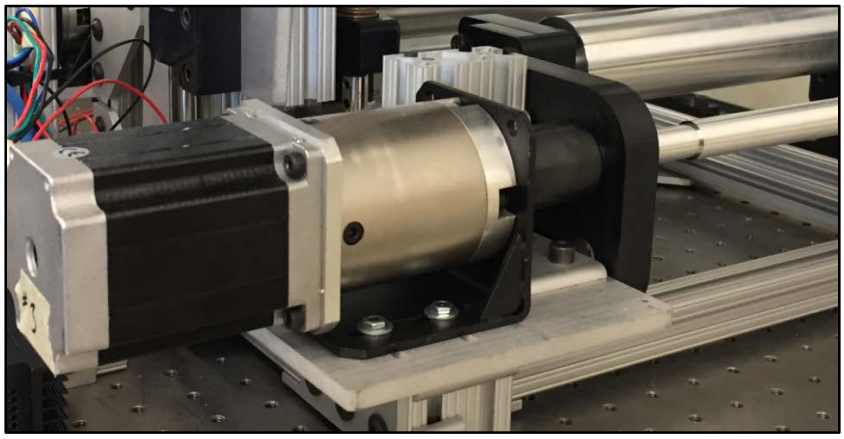

Figure 4.5: NEMA-23 stepper motor & planetary gearbox attached to winding axle

4.2.5 Central Rollers

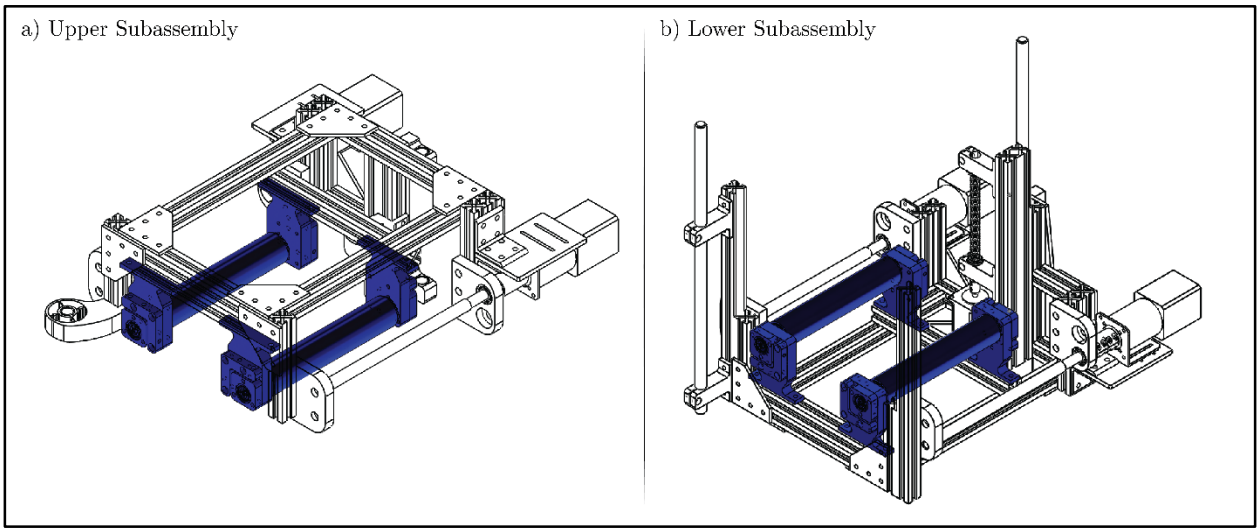

Figure 4.6: Central rollers in upper and lower subassemblies

The Upper and Lower Membrane Assemblies each incorporate a pair of central rollers whose purpose is to guide the two stretching membranes into contact with one other. The rollers are mounted on the same high-load ball bearings as the winding axles. Each is constrained axially by brass thrust bearings preloaded to $53\,N$ $(12\,lbf)$ using a wave spring.

The diameter of the central rollers is $44.45\,mm$ $(1.750" \pm 0.002")$ in order to clear the mounting brackets and ensure the top and bottom membranes can make direct contact. Together with the winding axles, the central rollers constrain the stretching membranes. This arrangement can be seen in Figure 4.7.

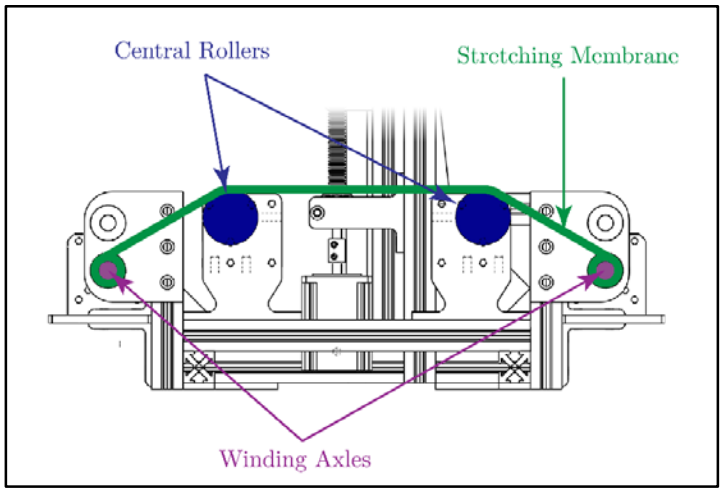

Figure 4.7: Path of stretching membrane over winding axles and central rollers

The central roller mounting brackets include three adjustable screws for fine-tuning the positioning of each central roller, and three additional screws for securing it in place. This combination allows the end of each roller to be adjusted to ensure proper mating between the upper & lower roller pairs.

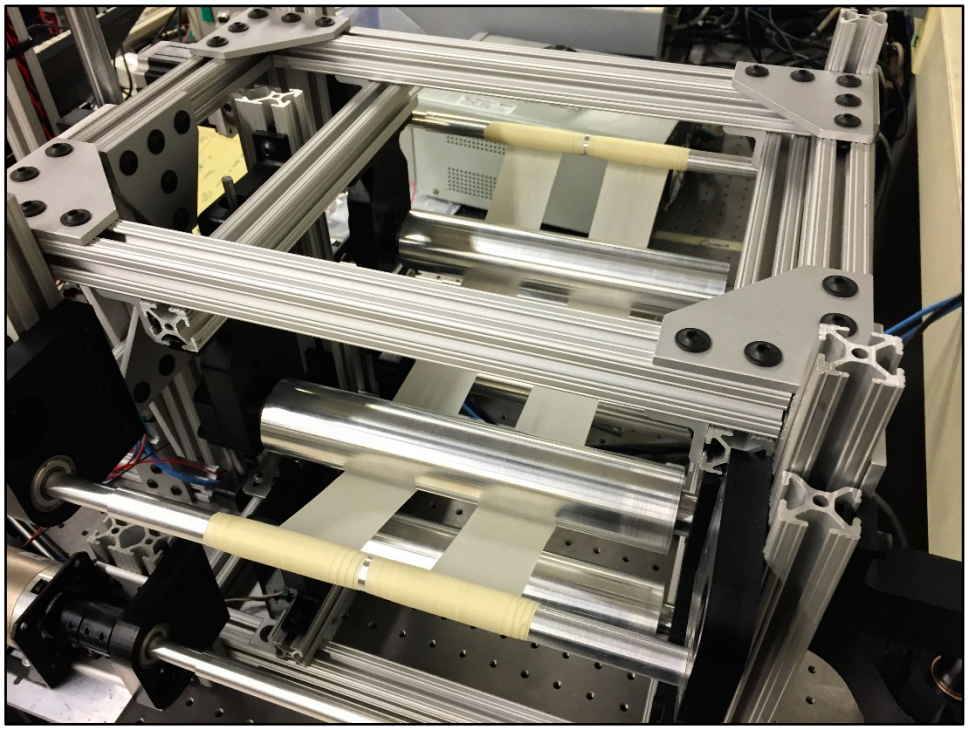

Figure 4.8: Photograph of two stretched membranes
Membranes on the upper subassembly are stretched across the central rollers by the winding axles

4.2.6 Mating Components

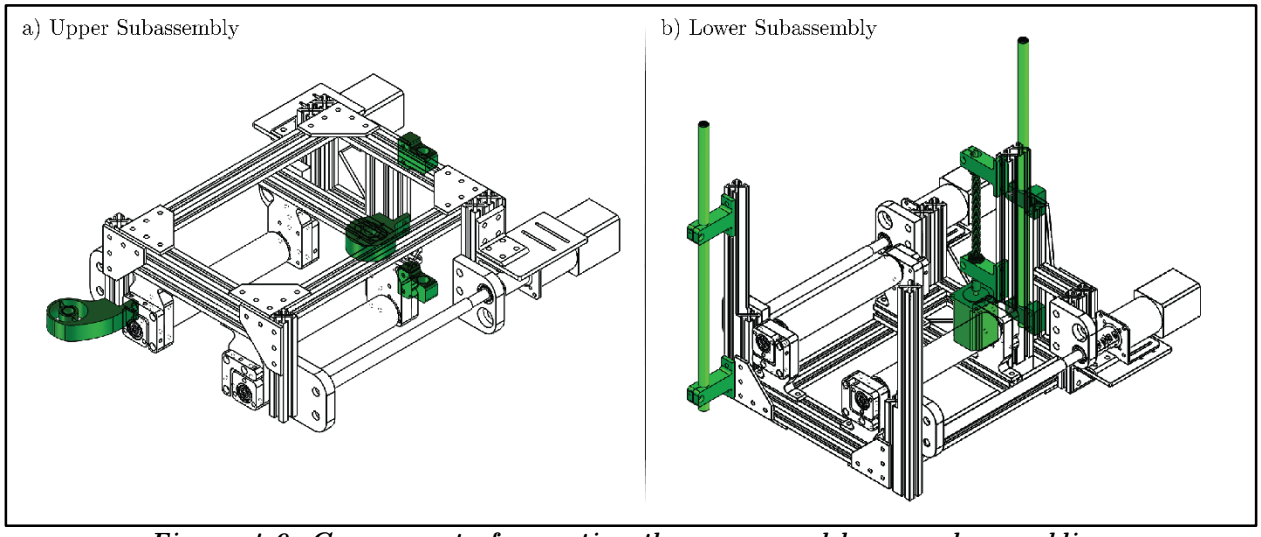

Figure 4.9: Components for mating the upper and lower subassemblies

The components discussed in this section provide for the proper mating and positioning of the upper and lower subassemblies. A lead screw is responsible for the vertical positioning of the

upper subassembly, while a system of guiderails and flexures constrains the remaining degrees of freedom.

4.2.6.1 Vertical Lead Screw

The prototype system implements a lead screw for actuating the upper subassembly up and down, allowing the membranes to separate or be drawn together. The placement of the lead screw is critical; it must be located as close to the upper assembly's center of mass as possible in order to prevent binding of the rail bushings on their guiderails. The lead screw in this assembly is located approximately 2.2 inches from the center-of-mass calculated in SolidWorks. This location was chosen so the lead screw could be placed as close to the center-of-mass as possible, while still leaving sufficient space for installation of other components and access to bolted joints.

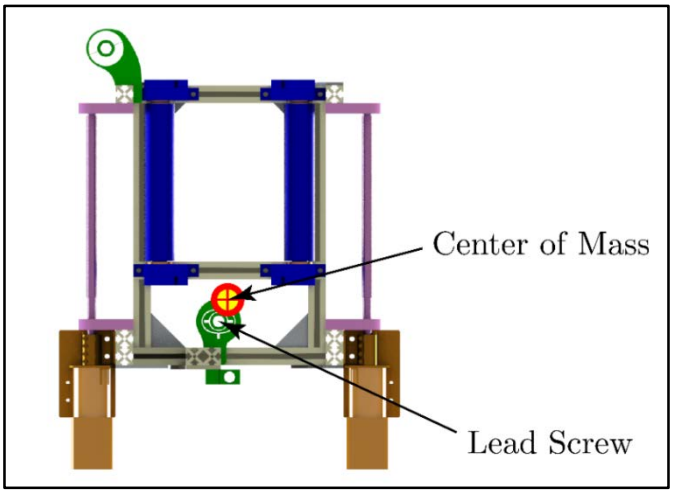

Figure 4.10: Location of lead screw relative to upper subassembly center-of-mass

A NEMA-23 stepper motor (Model #KL23H276-30-8B from Automation Technologies) and 1/2"-10 precision Acme-thread lead screw were chosen to provide the vertical impetus to the upper subassembly. With the motor's 200 steps per revolution and the 2.54mm (0.1") lead on the lead screw, this pair resolves 12.7 μm (0.0005") per step and beats the functional requirement for vertical resolution (100 μm).

The torque required to overcome friction and gravity to raise the upper assembly is [39]:

$$T_R = \frac{P_u d_p}{2}\left(\frac{\mu\pi d_p + L\cos(\alpha)}{\pi d_p \cos(\alpha) - \mu L}\right) + \mu_c\left(P_u + P_p\right)\frac{d_c}{2} \tag{55}$$

Table 8: List of Variables for Lead Screw Motor Torque Calculation

Symbol	*Value*	*Description*
T_R	$54\ Nm$ / $76\ oz.in.$	Torque to raise load on lead screw
P_u	$126\ N$ / $28.3\ lbf$	Approx. weight of upper assembly
d_p	$11.4\ mm$ / 0.45"	Lead screw pitch diameter
μ	0.4	Frict. coeff., lead screw & nut, cast iron on steel [40]
L	$2.54\ mm$ / 0.1"	Screw lead
α	14.5^o	Acme thread radial angle
μ_c	0.12	Frict. coeff., thurst bearing, oilite bronze on steel [41]
P_p	$31\ N$ / $7\ lbf$	Thrust bearing preload force
d_c	$19\ mm$ / 0.75"	Thrust bearing mean diameter

The selected motor has a rated torque of $1.99\ Nm$ ($282\ oz.in.$), satisfying the torque requirement with a safety factor of nearly four.

4.2.6.2 Flexures and Proper Constraint

Together with the vertical lead screw, the upper and lower subassemblies are mated using two guiderails. Two sleeve bearings mate the upper assembly to the primary guiderail, while a third sleeve bearing mates the upper assembly to the secondary guiderail:

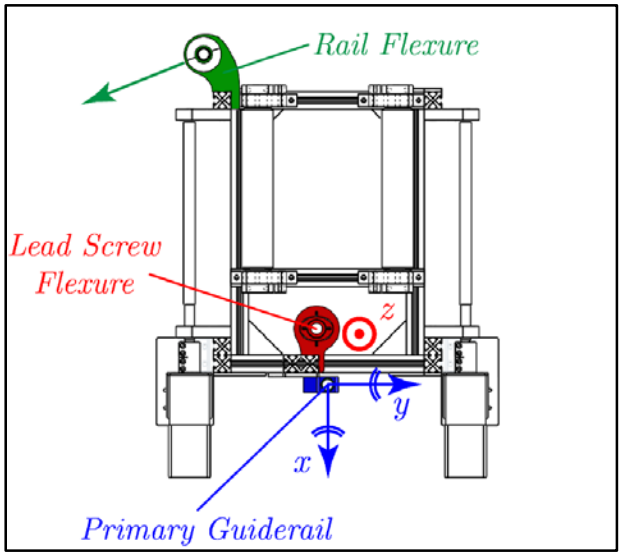

Figure 4.11: Upper subassembly constraint diagram

Sleeve bearings at the primary (blue) and secondary (green) guiderails constrain five degrees of freedom for the upper subassembly, while vertical translation is constrained at the lead screw (red). Constraint of the upper assembly is summarized in Table 9:

Table 9: Upper Subassembly Constraints and Degrees of Freedom

Degree of Freedom	*Constrained By:*
x-translation	Primary guiderail & sleeve bearings
x-rotation	Primary guiderail & sleeve bearings
y-translation	Primary guiderail & sleeve bearings
y-rotation	Primary guiderail & sleeve bearings
z-translation	Lead screw, sleeve bearing, & Lead Screw Flexure
z-rotation	Secondary guiderail, sleeve bearing, & Rail Flexure

Overconstraint is eliminated through the use of two flexures: the Lead Screw Flexure and the Rail Flexure. Both were machined from ABS using an abrasive waterjet and were designed using finite-element software (SolidWorks) to tolerate $\pm 0.75\ mm$ (0.03") deflection during operation.

4.3 Stretching Membranes and Folding Materials

Latex was selected as the material of choice for the stretching membrane. Latex is capable of recovering from extremely high strains and typically exhibits a maximum elongation before break of over 700%. Further it is widely available at low-cost and can be obtained in thin sheets as is required for this application. Latex exhibits viscoelastic behavior and so is prone to stress relaxation when maintained in tension. However, as this process is inherently displacement-controlled and not force-controlled, the stress relaxation does not significantly impact the performance of the machine. This is validated in Section 5.2.

Polyester film (13 μm / 0.0005" thick) was selected as the material to be folded. The thickness tolerance on the type of film used is extremely small (±1.3 μm / 0.00005") [42]. This film was selected to mimic the mechanical response of cell-bearing nanoporous membranes, which are typically constructed using similar materials and thicknesses.

4.4 Electronics and Controls

Electronic control of the five stepper motors in this system begins with a custom National Instruments LabVIEW program along with a CompactDAQ chassis for control signal generation. The signal diagram for the system is as follows:

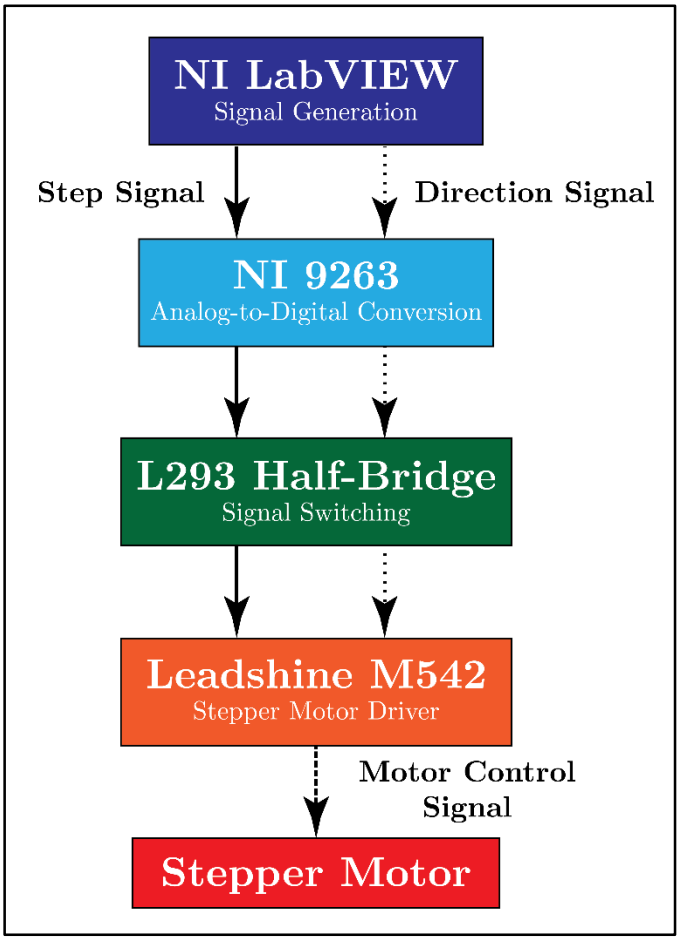

Figure 4.12: Motor control signal diagram

This control system operates in an open-loop scheme. This is a common arrangement for stepper motors operating well below their rated values for holding torque and maximum speed, as is the case with this system. The position of the stepper motors advances one discrete step for each voltage pulse sent to the stepper motor driver. LabVIEW determines the instantaneous position of each stepper motor using dead-reckoning; it assigns a position value to each motor, and then increments/decrements that value for each forward/reverse step commanded of the motor. This eliminates the need for position sensors and feedback control algorithms.

4.4.1 LabVIEW Signaling Scheme

The LabVIEW code which generates the motor control signals is organized as three components:

Front End – LabVIEW-operator interface. Here, the user supplies:

- **Sheet Parameters:** L_H, L_p, ϕ_f, t
- **System Parameters:** L_0', r

Back End – Performs calculations using input parameters and current system state. Utilizes the equations from Chapter 3 to generate stepper motor commands as the folding process executes.

Signal Generation – Converts stepper motor commands into control signals (pulse waveforms), which are output using an NI 9263 CompactDAQ.

This process is illustrated in Figure 4.13.

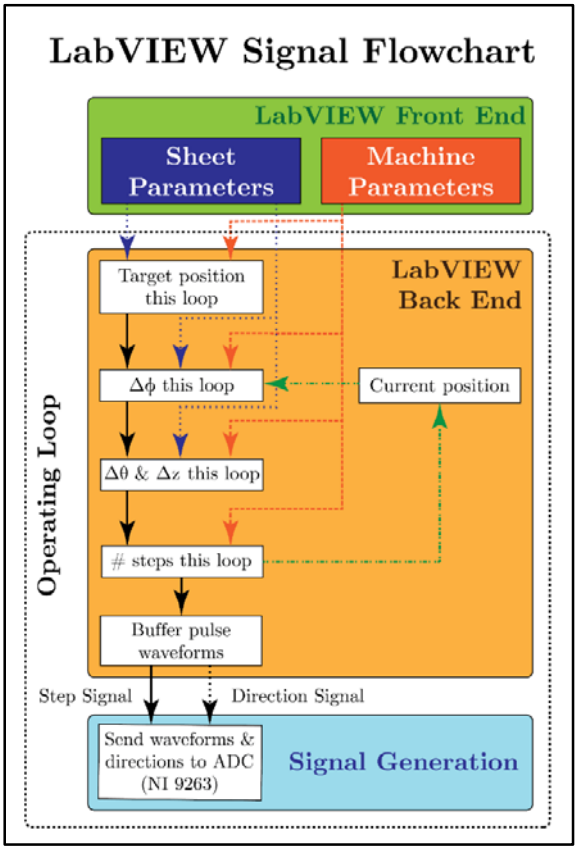

Figure 4.13: LabVIEW control program signal flowchart

4.4.2 Linearization of Folding Procedure

As a direct result of the large shape changes involved with folding, the rotational speeds of the stretching and lead screw stepper motors change significantly over the course of the folding process. In relation to the folding angle, the membrane separation rate decreases during the process, while the stretching rate increases. This is seen in Figure 4.14, which depicts the membrane stretch and separation as functions of the folding angle (in this example $L_H = 0$):

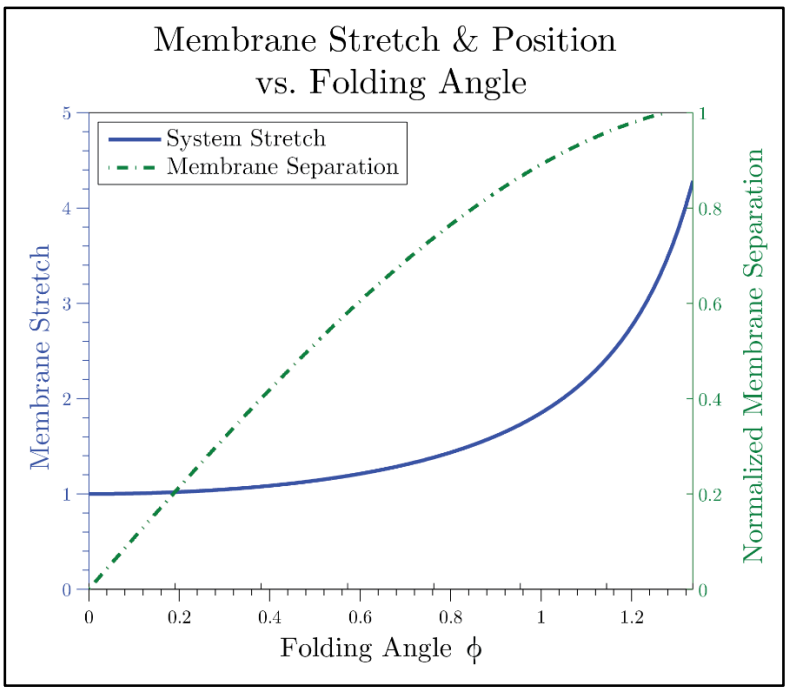

Figure 4.14: Simulation of rates-of-change for membrane stretch and separation

The LabVIEW control system approximates these constantly changing speeds by dividing the folding process into 100 linearized steps, each with a constant winding rate. This closely matches the non-linearized speeds:

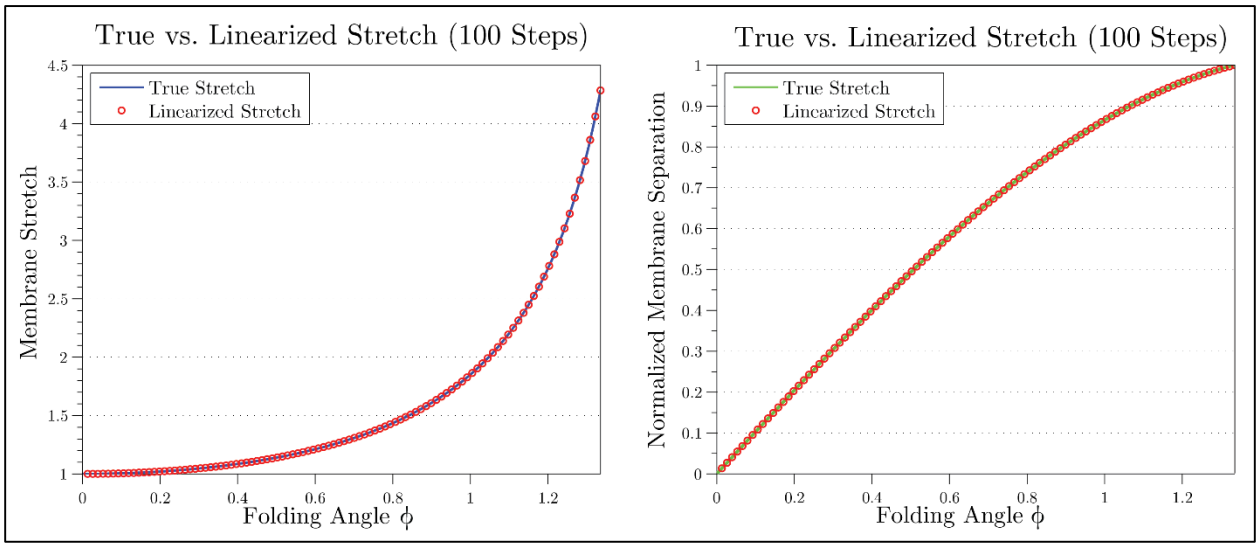

Figure 4.15: Simulated stretch linearization closely matches ideal curves

4.4.3 Stepper Motor Driver and Signal Switching

One Leadshine M542 motor driver is used to power each of the five stepper motors in this system (four winding motors and one lead screw motor). The M542 driver accepts voltage inputs on two channels: (a) a pulse channel, and (b) a direction channel. A single step is executed upon detection of a rising voltage from the pulse channel, and the direction of that step (clockwise/counterclockwise) is determined by the voltage state of the direction channel (0/5 volts, respectively). In this fashion, a waveform of N pulses advances the stepper motor by $\pm N$ steps, depending on the current direction setting.

Each of the channels on the M542 stepper drivers draws a current of approximately $18\,mA$, which exceeds the output of the NI 9263 CompactDAQ (rated at just $1\,mA$ per channel). To overcome this, an L293 half-bridge chip is used as a 0-5V switching power transistor, with the NI 9263 signal acting as the switching signal. A separate switching circuit is used for each direction signal and each step signal for each motor.

4.5 Functional Requirements Revisited

In Table 10 below, the functional requirements for this machine are revisited and compared with the values the machine has been designed to reach:

Table 10: Functional Requirements & Expected Performance

Property	Required Value	*Designed Value*	Units
Folding Area	>150x150	***200x225***	mm^2
Vertical Travel	>75	***102***	*mm*
Membrane Thickness	<0.3	***<0.3***	*mm*
Tension Force	>2500	***>5000***	*N*
Stretch Resolution	<0.0005	***<0.00001***	--
Vertical Resolution	<0.1	***0.012***	*mm*
Dimensional Stability	<1	*See Section 5.2*	*% per 45 min*

Chapter 5

System Operation & Preliminary Testing

The contents of this chapter concern the operation of the prototype machine for the folding of real systems. In Section 5.1, the prototype machine's ability to achieve a desired stretch is validated. In Section 5.2, the dimensional stability of the machine is demonstrated. Section 5.3 details the procedures required to prepare the machine for operation, and Section 5.4 presents preliminary results of a folding trial.

5.1 Validation of Stretch Relationship

The ability to attain accurate membrane stretch is a key performance goal for this machine, and this section documents the ability of the prototype machine to achieve this. The accuracy of achievable stress was measured according to the following process:

1. A stretching membrane was mounted to its winding axles, wound slightly to eliminate sagging, and then marked in two locations with permanent marker.
2. A top-down photograph of the stretching membrane was taken.
3. A stretch of $\lambda = 2$ (with respect to the membrane stretch in Step 2) was applied to the membrane.
4. A second top-down photograph of the stretching membrane was taken.
5. The distance between markings on each photograph was digitally measured. For consistency, all measurements were made by measuring the inside-edge of one black dot to the inside-edge of the other. A field-of-view correction (described in Appendix C) was also applied to minimize the effect of perspective on the measurement.
6. The ratio of stretched and unstretched distances was compared to the desired stretch $(\lambda = 2)$ to find the percent system stretch error.

For this experiment, a GoPro Hero 3 Black Edition camera was used to capture all images. The shutter was triggered via wireless remote to prevent accidental disturbance of the camera. Figure 5.1 shows the measurement images from this trial with measurement marks are circled in red for visibility:

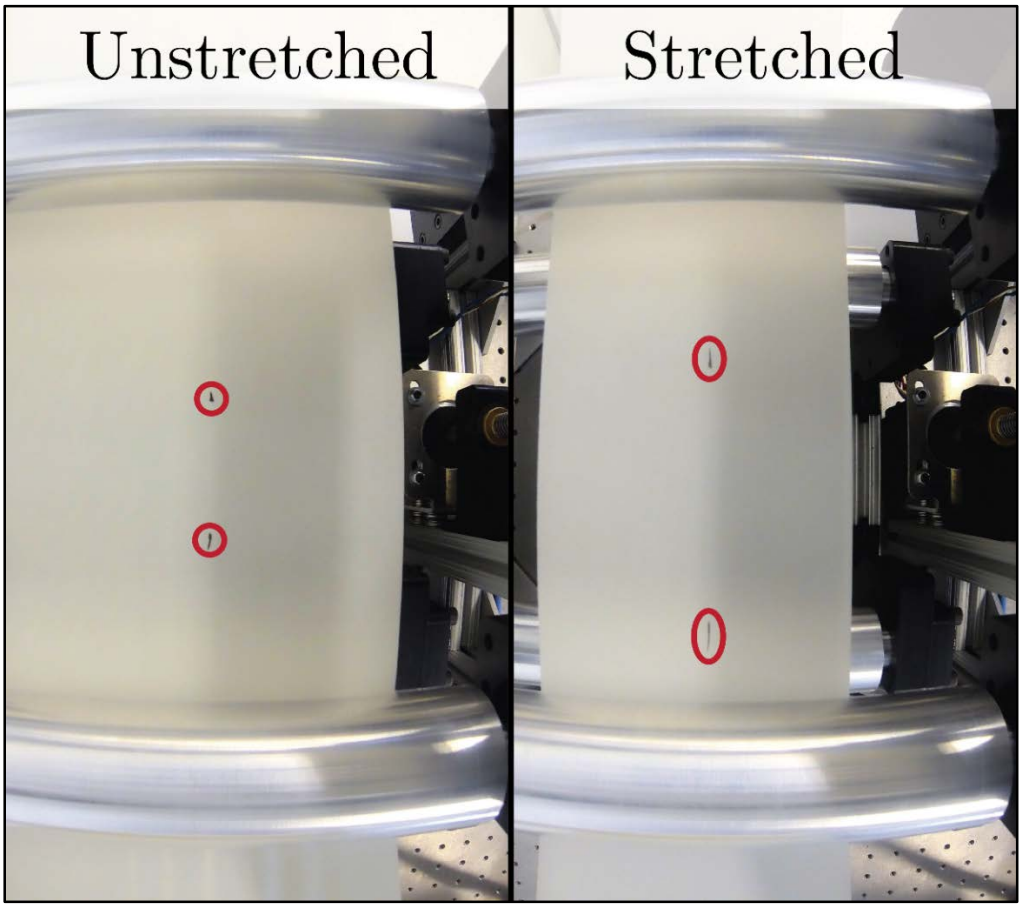

Figure 5.1: Photographs of stretch validation test

The results of this trial are given in by Table 11:

Table 11: Stretch Validation Test Results

Initial Separation:	438 ± 1 pixels
Stretched Separation:	851 ± 1 pixels
Lens-Corrected Stretch:	1.98 ± 0.01
Ideal Stretch:	2.00
% Stretch Error:	**1.0% ± 0.5%**

With a measured stretch error of approximately 1.0%, the deviation from ideal stretch is very small. Potential sources of error in this measurement include:

- Aberrations or other distortions in the photographic measurement system
- Error resulting from the winding radius approximation
- Friction with the central rollers induces additional lateral stresses not captured in the ideal model
- Errors in the measurements of r_0, or L_0, as detailed in Chapter 3.

5.2 Dimensional Stability

The dimensional stability of stretch was characterized in a similar fashion to the previous test:

1. A stretching membrane was mounted to its winding axles, wound slightly to eliminate sagging, and then marked in two locations with permanent marker.
2. A top-down photograph of the stretching membrane was taken.
3. A stretch of $\lambda = 2$ (with respect to the membrane stretch in Step 2) was applied to the membrane.
4. A second top-down photograph of the stretching membrane was taken.
5. 45 minutes were allowed to pass.
6. A third top-down photograph of the stretching membrane was taken.
7. The membrane stretch was returned to $\lambda = 1$.
8. A final top-down photograph of the stretching membrane was taken.
9. The distance between markings on each photograph was digitally measured. For consistency, all measurements were made by measuring the inside-edge of one black dot to the inside-edge of the other. A field-of-view correction (described in Appendix C) was also applied to minimize the effect of perspective on the measurement.
10. The unstretched and stretched separations before and after the 45 minute holding period are compared to determine the dimensional stability of the membrane stretch.

For this experiment, a GoPro Hero 3 Black Edition camera with remote shutter trigger was used for all photographs. Table 12 shows the results of this trial:

Table 12: Dimensional Stability Test Results

Measurement	Target Stretch	Elapsed Time (minutes)	Measured Stretch	**Measured % Error**
1	1.00	0	1.00 ± 0.01	**0.0% ± 1.0%**
2	2.00	1	1.98 ± 0.01	**1.0% ± 0.5%**
3	2.00	45	1.98 ± 0.01	**1.0% ± 0.5%**
4	1.00	46	1.01 ± 0.01	**1.0% ± 1.0%**

As seen from these results, the viscoelastic properties of the latex introduced very little error. Over 45 minutes under tension, the measured stretch was not observed to vary. Measured error after subsequent release of tension was 1%, meeting the functional requirement for dimensional stability (<1% over 45 minutes). The resolution of the measurement technique was a limiting factor in this trial and the confidence interval on the measured error is of the same scale as the error itself. As a result, the true system performance may be better than stated here.

5.3 Setup and Preparation for Folding

Each test run on the prototype machine requires the preparation of multiple components: the stretching membranes, the sheet to be folded, and the machine itself. These items are discussed in the following three subsections.

5.3.1 Membrane Preparation

Trials for this machine utilized four folding membranes in total: two attached to the lower subassembly and two attached to the upper subassembly. Each membrane was 3" (76.2 mm) wide, 0.006" (0.15 mm) thick, and approximately 20" (510 mm) long. Before placement, each membrane was washed and dried to remove any existing powders and particulates from the manufacturing process.

Alignment was achieved by laying the membranes across the lower subassembly (central rollers and winding axles) in the desired final arrangement: neighboring membranes were laid side-by-side and the upper membranes were laid directly on top of the lower membranes. The upper subassembly was then lowered until the upper and lower central rollers made contact, thereby

holding the membranes together and preserving the alignment. The membranes were then attached to their winding axles using masking tape. The tape was used for positioning and initial attachment, but also prevented the membranes from slipping on the axles during winding. This effect is possible due to the winding friction between the membranes and axles, which magnifies the maximum holding force from the tape according to the capstan equation:

$$\frac{T_{load}}{T_{hold}} = e^{\mu\theta} \tag{56}$$

Here, T_{hold} is the force required to oppose a loading T_{load} when the membrane is wound around the winding axle (with coefficient of friction μ) by θ radians. The exponential nature of this relationship enables even a small strip of masking tape to prevent slippage of the system. The length of each membrane (which is nominally 108 mm (4.25") longer than the axle-to-axle distance of the system) was chosen such that more than a full rotation of wrap around each axle is achieved before tension is induced in the membrane, ensuring a large load could be opposed by a very small holding force. It should be noted that the capstan equation assumes a non-elastic rope and is not valid once the membrane winds around itself (it assumes the case of a rope wrapping around a cylinder), so should not be used for predictive calculations in this system. It is presented here only to qualitatively demonstrate why a small strip of tape can be used to oppose the large tensile forces observed in this system.

After attachment, the upper and lower subassemblies were separated and the membranes were pulled into tension with a nominal stretch of approximately 5 in preparation for adhesion of the folding sheet.

5.3.2 Preparation of Folding Sheet, Adhesive, and Mask

The polyester film used as the folding sheet (137mm x 96.5 mm or 5.4" x 3.8") was cut to size using an Epilog Mini 24 laser cutter. Two paper masks of the same dimensions, one for each side of the folding sheet, were likewise cut using the laser cutter. The masks act as stencils for application of the adhesive, confining it to the desired vertex locations only.

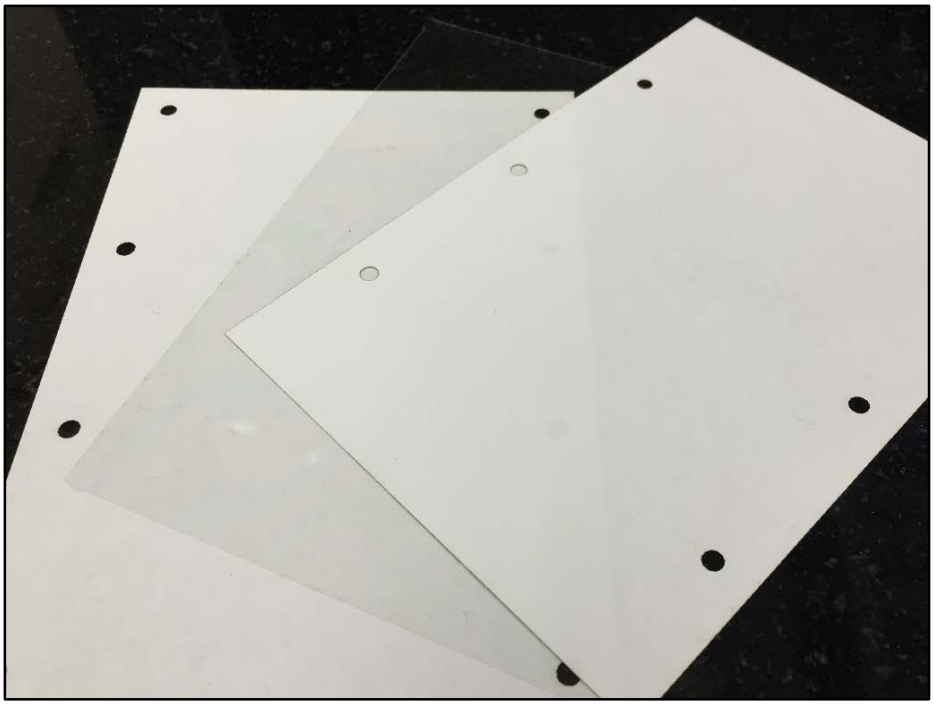

Figure 5.2: Laser-cut paper masks and polyester folding film

While the centers of two adjacent membranes remain equidistant during stretching, the Poisson effect causes the inside edges of the membranes to draw outwards and the outside edges to draw inwards, as seen in Figure 5.3. During release of tension, the opposite occurs: interior edges draw towards one another while exterior edges draw away. The spacing width of the mask holes was selected to be 81 mm (3.2") – slightly greater than the center-to-center distance of the stretching membranes (76 mm / 3"). The folding sheet would therefore experience a small sideways tension when the membrane strain was released, preventing wrinkling in this direction.

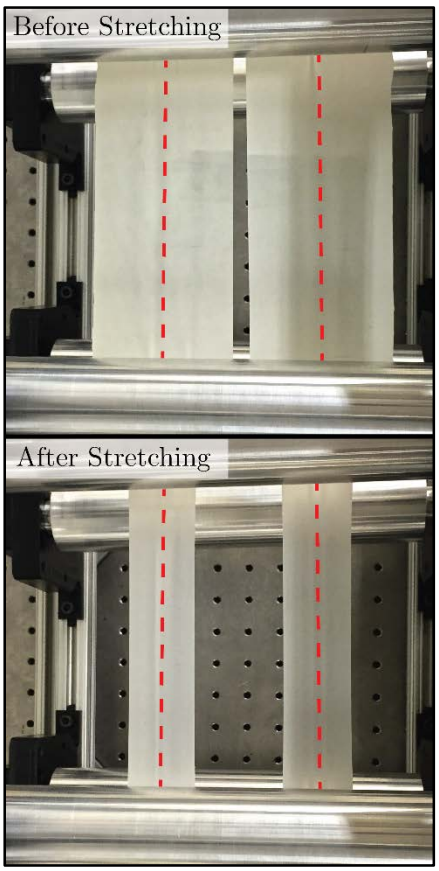

Figure 5.3: Effect of Poisson ratio: before & after stretching

Mechanical fixturing of the folding material to the stretching membrane was achieved using an adhesive. Due to the large strains imposed during operation, delamination of the adhesive was a major concern. This is because the stretching of the membrane acts to "peel" the adhesive from the membrane (this same phenomenon is what allows a 3M

Command Strip to be easily removed using relatively little force). An adhesive used in an application such as this must be sufficiently strong as to resist this peeling effect. 3M rubber and vinyl adhesive #80 was selected as it is specifically tailored to bind rubbers. Unlike other adhesives tested, the nature of the 3M #80 bond does not appear to suffer from conventional delamination, even under very high imposed strains.

During application of the adhesive the folding sheet was held between the two masks. Although the #80 adhesive is an aerosol spray, it was not applied directly to the sheet as spraying was neither easily controlled nor repeatable. Instead, the adhesive was sprayed into a small pool on another substrate, and then transferred to the folding sheet using an applicator stick. Adhesive was first applied to the bottom side of the folding sheet, the bottom mask was peeled away, and the sheet was lowered onto the membranes spanning the lower assembly. Adhesive was then applied to the top sheet, the top mask was peeled away, and the upper assembly was lowered into place (with the upper membranes making contact with the folding sheet). Although the holes in the mask were 3.18 mm (0.125") in diameter, it was observed experimentally that the total glued area could reach 6.4 mm (0.25") in diameter after making contact with the stretching membranes. This variation in adhesion area is believed to be a large source of error in this system and is discussed further in Section 5.4.

After application, this adhesive must be allowed to set for at least 30 minutes to ensure the bonds are sufficiently strong to endure folding.

5.3.3 Software Preparation

With the physical system prepared for folding, final preparation occurs in software by setting the appropriate system, membrane, and folding structure parameters in the LabVIEW control panel as seen in Figure 5.4:

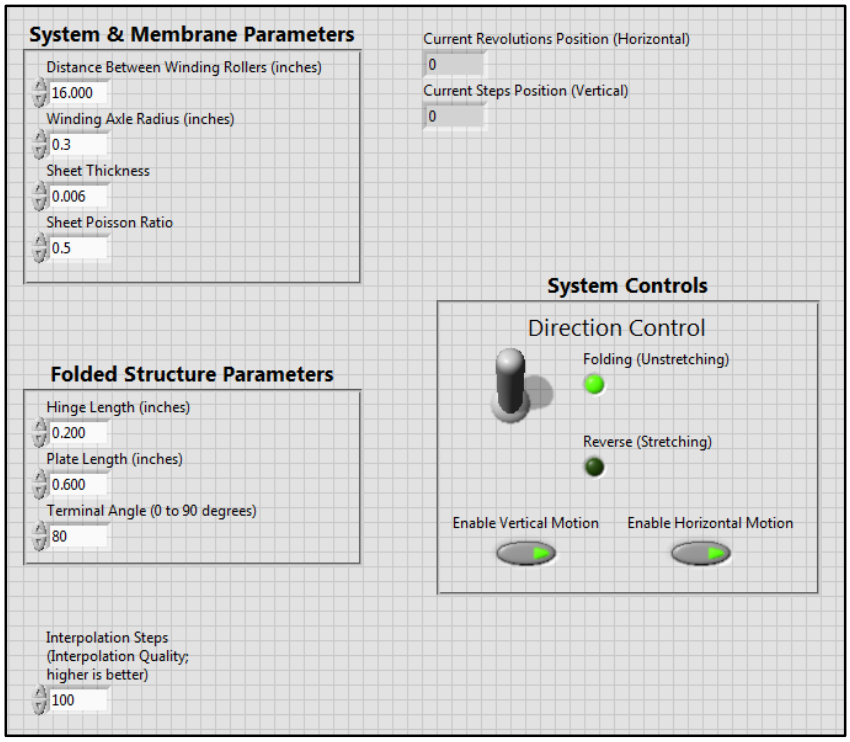

Figure 5.4: LabVIEW Control Panel

At this point, system preparation is completed and a test run can be executed.

5.4 Folding Results

Four stills from the folding sequence can be seen in Figure 5.5. In (a), folding has not yet begun and the membrane-sheet-membrane layers remain flat and flush with one another. In (b) the membranes have begun to separate, and some membrane stretch has been released. This process continues and the folding sheet begins to take on a three-dimensional geometry; in (c) the folding angle approaches 45 degrees. Folding continues until completion in (d), where the triplet folded units are clearly observed.

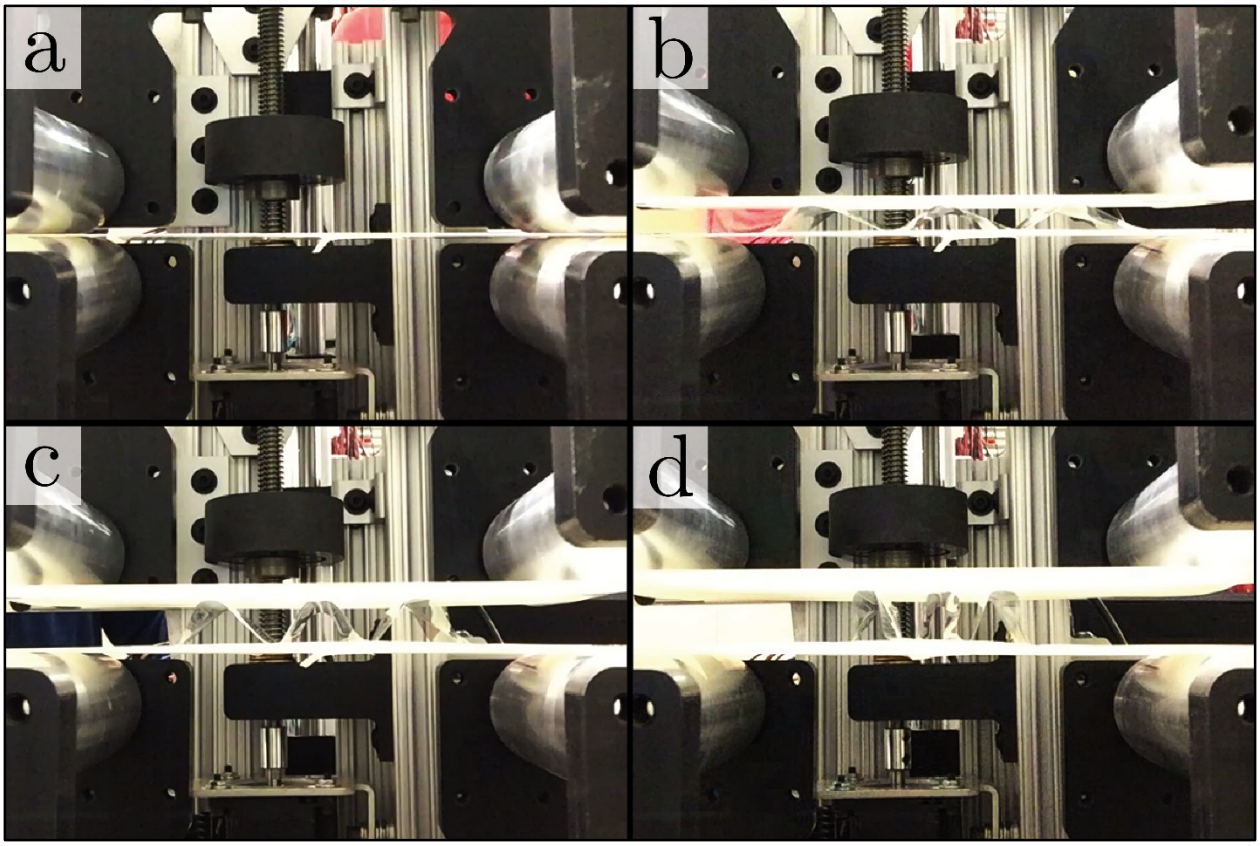

Figure 5.5: Sequence of images showing various points along the folding process

The final folded structure is shown from two additional angles in Figure 5.6:

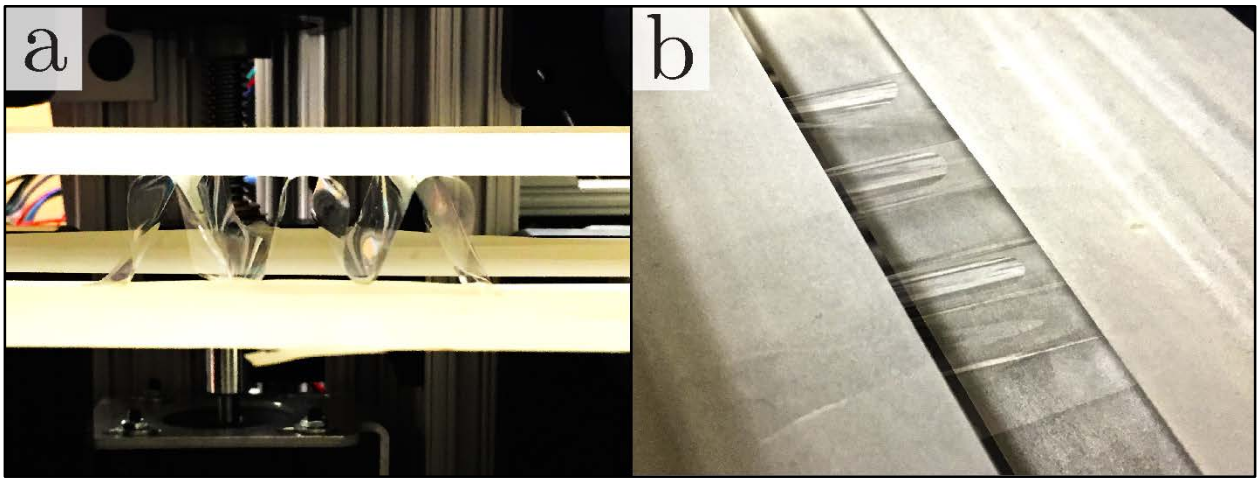

Figure 5.6: Structure folded using membrane-driven process
(a) Side-view close-up, where repeating accordion structure is easily observed
(b) Top-view, with fold peaks clearly visible

It is clear from these images above that this prototype membrane-driven folding process has achieved the goal of generating repeated 3D geometries in parallel. However, the folding units attained do not assume the desired shape. Significant bending and warping – a clear deviation from the ideal behavior modeled in Chapter 3 – is observed, and the folding units themselves are not uniform. This deviation from the ideal case is believed to result primarily from:

1. Poor precision in both the placement of and amount of adhesive at each vertex
2. The bending stiffness of the folding sheet, which introduces undesired curvature
3. Changes in the hinge length as the membrane stretches (the model presented in Chapter 3 assumes a constant hinge length)

Of these sources of error, that resulting from the adhesive is believed to be the most significant. In particular, the application of adhesive proved to be difficult to control. The sizes of glue sites were observed to vary widely, reaching twice the desired adhesion diameter (diameter of the mask hole) or more. This resulted in wide variations in the sizes of glue sites across a folding sheet, reducing performance of the system as a whole by (a) reducing the accuracy of the hinge length system parameter (input into LabVIEW), and (b) introducing large variations in glue site size from one site to the next.

Chapter 6

Conclusions & Future Work

The purpose of this work was the modeling and prototyping of a highly parallelized process capable of folding large and compliant two-dimensional sheets into ordered, three-dimensional structures. No existing research has attempted this previously. This work has introduced "membrane-driven folding," a process whereby pre-strained elastic membranes are used to drive folding. Rules for constraint and actuation, governing kinematic equations, and design rules necessary to implement this process were then presented. These were translated into functional requirements for a prototype machine, the design for which was given. This prototype machine was then tested and demonstrated to successfully achieve folding in this highly parallel, membrane-driven fashion.

The direct application of this work is the assembly of tissue scaffolds for replacement of human tissues and organs, where a folding process meeting the necessary functional requirements would enable the production of man-made tissues and organs at a fraction of the cost and time required by existing methods.

6.1 Thesis Synopsis

Chapter 1 of this thesis presented the motivation for this work and the need for a scalable folding process to enable the rapid and cost-effective manufacture of synthetic human tissues. Chapter 2 discussed options for actuating and constraining origami and showed that pointwise actuation provides the greatest control over hinge directionality and control of folding. Chapter 3 introduced the equations relevant to membrane-driven folding. Chapter 4 outlined the design of a prototype membrane-driven folding machine. Chapter 5 explained the setup and preparation process for running the prototype machine and presented preliminary results. In the next section of this chapter (Chapter 6), future work and paths forward are discussed.

6.2 Future Work

6.2.1 Error Correction & Automated Adhesion

The most immediate future work concerns the identification and correction of errors contributing to the non-ideal panel warp observed in testing. It is believed that the most significant source of this error lies in the poor process control in application of the adhesive which binds the folding structure to the folding membranes. Devising and implementing a repeatable and automated process for adhesive application would significantly increase the repeatability and precision of the system, after which other sources of error could be pursued. Additionally, an improved adhesion process would allow for much smaller unit cells to be folded (as glue sites could be made much smaller) and would eliminate what is currently the least automated step in the folding process, significantly improving cycle time.

6.2.2 Roll-to-Roll Manufacturing

Although this process is theoretically capable of folding hundreds or thousands of unit cells in one operation, the total output of the process is limited by the folding cycle time. A continuous roll-to-roll application of this process would not only eliminate many human factors in setup and operation, but would also significantly increase the process throughput (potentially by an order of magnitude or more).

6.2.3 Patterned Folding Sheets

The process discussed herein is intended for completely homogeneous sheets. However, folding performance could be significantly improved with the utilization of perforations or other features to enhance the folding performance of the system. One major drawback of homogeneous sheets is the lack of local features for promoting folding at precise locations, generating bending stresses in the material and producing undesired curvature and bending. Incorporating laser perforations into the folding sheet would enhance performance by further localizing bending to the perforation axis and the observed behavior would more closely mimic the model presented in Chapter 3.

6.2.4 Design for Biocompatibility

The ultimate application of this work is the assembly of tissue scaffolds for tissue and organ generation. To that end, many concessions for supporting cell life must be made in future versions. This includes:

- Utilization of biocompatible materials. For the stretching membrane (a biocompatible silicone with a very high extensile limit is one such option)
- A means of removing the folded structure from the machine and storing it without significant disturbance or loss of shape
- Pairing this process with TASR or other cell-sorting methods for a seamless and efficient workflow
- Validating the accuracy and precision of the system, especially with regards to the placement of cells in relation to neighboring surfaces

6.2.5 Two-Dimensional Folding

The work presented herein concerns the folding of sheets into the accordion pattern, a simple and straightforward one-dimensional form. By adding winding axles in the other in-plane direction, two-dimensional motion control would be possible and a variety of other shapes could be achieved. This would not only increase the complexity of potential folded forms, but would also improve the packing efficiency of the process by allowing folding in two directions simultaneously.

References

[1] R. J. Lang. (Accessed March 2015). *Robert J. Lang Origami*. Available: http://www.langorigami.com/

[2] T. Tachi, "Rigid-Foldable Thick Origami," in *Origami 5*, ed: A K Peters/CRC Press, 2011, pp. 253-263.

[3] National Academy of Engineering. (Accessed September 2013). *National Academy of Engineering: NAE Grand Challenges for Engineering*. Available: http://www.engineeringchallenges.org

[4] A. A. Chen, D. K. Thomas, L. L. Ong, R. E. Schwartz, T. R. Golub, and S. N. Bhatia, "Humanized Mice with Ectopic Artificial Liver Tissues," *Proceedings of the National Academy of Sciences,* vol. 108, pp. 11842-11847, 2011.

[5] S. Levenberg, J. Rouwkema, M. Macdonald, E. S. Garfein, D. S. Kohane, D. C. Darland*, et al.*, "Engineering Vascularized Skeletal Muscle Tissue," *Nature Biotechnology,* vol. 23, pp. 879-884, 2005.

[6] K. Stevens, K. Kreutziger, S. Dupras, F. Korte, M. Regnier, V. Muskheli*, et al.*, "Physiological Function and Transplantation of Scaffold-Free and Vascularized Human Cardiac Muscle Tissue," *Proceedings of the National Academy of Sciences,* vol. 106, pp. 16568-16573, 2009.

[7] R. Glicklis, J. C. Merchuk, and S. Cohen, "Modeling Mass Transfer in Hepatocyte Spheroids via Cell Viability, Spheroid Size, and Hepatocellular Functions," *Biotechnology and Bioengineering,* vol. 86, pp. 672-680, 2004.

[8] F. M. Wood, M. L. Stoner, B. V. Fowler, and M. W. Fear, "The Use of a Non-Cultured Autologous Cell Suspension and Integra® Dermal Regeneration Template to Repair Full-Thickness Skin Wounds in a Porcine Model: A One-Step Process," *Burns,* vol. 33, pp. 693-700, 2007.

[9] A. Atala, S. B. Bauer, S. Soker, J. J. Yoo, and A. B. Retik, "Tissue-Engineered Autologous Bladders for Patients Needing Cystoplasty," *The Lancet,* vol. 367, pp. 1241-1246, 2006.

[10] P. Macchiarini, P. Jungebluth, T. Go, M. A. Asnaghi, L. E. Rees, T. A. Cogan*, et al.*, "Clinical Transplantation of a Tissue-Engineered Airway," *The Lancet,* vol. 372, pp. 2023-2030, 2008.

[11] T. Shin'oka, Y. Imai, and Y. Ikada, "Transplantation of a Tissue-Engineered Pulmonary Artery," *New England Journal of Medicine,* vol. 344, pp. 532-533, 2001.

[12] T. Boland, T. Xu, B. Damon, and X. Cui, "Application of Inkjet Printing to Tissue Engineering," *Biotechnology Journal,* vol. 1, pp. 910-917, 2006.

[13] P. G. Campbell and L. E. Weiss, "Tissue Engineering with the Aid of Inkjet Printers," 2007.

[14] K. Jakab, A. Neagu, V. Mironov, R. R. Markwald, and G. Forgacs, "Engineering Biological Structures of Prescribed Shape using Self-Assembling Multicellular Systems," *Proceedings of the National Academy of Sciences of the United States of America,* vol. 101, pp. 2864-2869, 2004.

[15] K. Jakab, C. Norotte, B. Damon, F. Marga, A. Neagu, C. L. Besch-Williford, *et al.*, "Tissue Engineering by Self-Assembly of Cells Printed into Topologically Defined Structures," *Tissue Engineering Part A,* vol. 14, pp. 413-421, 2008.

[16] K. Jakab, C. Norotte, F. Marga, K. Murphy, G. Vunjak-Novakovic, and G. Forgacs, "Tissue Engineering by Self-Assembly and Bio-Printing of Living Cells," *Biofabrication,* vol. 2, p. 022001, 2010.

[17] M. Nakamura, A. Kobayashi, F. Takagi, A. Watanabe, Y. Hiruma, K. Ohuchi, *et al.*, "Biocompatible Inkjet Printing Technique for Designed Seeding of Individual Living Cells," *Tissue Engineering,* vol. 11, pp. 1658-1666, 2005.

[18] Y. Nishiyama, M. Nakamura, C. Henmi, K. Yamaguchi, S. Mochizuki, H. Nakagawa, *et al.*, "Development of a Three-Dimensional Bioprinter: Construction of Cell Supporting Structures using Hydrogel and State-of-the-Art Inkjet Technology," *Journal of Biomechanical Engineering,* vol. 131, p. 035001, 2009.

[19] C. Norotte, F. S. Marga, L. E. Niklason, and G. Forgacs, "Scaffold-Free Vascular Tissue Engineering using Bioprinting," *Biomaterials,* vol. 30, pp. 5910-5917, 2009.

[20] J. A. Phillippi, E. Miller, L. Weiss, J. Huard, A. Waggoner, and P. Campbell, "Microenvironments Engineered by Inkjet Bioprinting Spatially Direct Adult Stem Cells Toward Muscle-and Bone-Like Subpopulations," *Stem Cells,* vol. 26, pp. 127-134, 2008.

[21] R. E. Saunders, J. E. Gough, and B. Derby, "Delivery of Human Fibroblast Cells by Piezoelectric Drop-on-Demand Inkjet Printing," *Biomaterials,* vol. 29, pp. 193-203, 2008.

[22] T. Xu, C. A. Gregory, P. Molnar, X. Cui, S. Jalota, S. B. Bhaduri, *et al.*, "Viability and Electrophysiology of Neural Cell Structures Generated by the Inkjet Printing Method," *Biomaterials,* vol. 27, pp. 3580-3588, 2006.

[23] T. Xu, J. Jin, C. Gregory, J. J. Hickman, and T. Boland, "Inkjet Printing of Viable Mammalian Cells," *Biomaterials,* vol. 26, pp. 93-99, 2005.

[24] H. Yamazoe and T. Tanabe, "Cell Micropatterning on an Albumin-Based Substrate using an Inkjet Printing Technique," *Journal of Biomedical Materials Research Part A,* vol. 91, pp. 1202-1209, 2009.

[25] J. S. Miller, K. R. Stevens, M. T. Yang, B. M. Baker, D.-H. T. Nguyen, D. M. Cohen, *et al.*, "Rapid Casting of Patterned Vascular Networks for Perfusable Engineered Three-Dimensional Tissues," *Nature Materials,* vol. 11, pp. 768-774, 2012.

[26] G. Agarwal and C. Livermore, "Chip-Based Size-Selective Sorting of Biological Cells using High Frequency Acoustic Excitation," *Lab on a Chip,* vol. 11, pp. 2204-2211, 2011.

[27] N. Bassik, G. M. Stern, and D. H. Gracias, "Microassembly based on Hands Free Origami with Bidirectional Curvature," *Applied Physics Letters,* vol. 95, p. 091901, 2009.

[28] S. M. Felton, M. T. Tolley, B. Shin, C. D. Onal, E. D. Demaine, D. Rus, *et al.*, "Self-Folding with Shape Memory Composites," *Soft Matter,* vol. 9, pp. 7688-7694, 2013.

[29] R. Fernandes and D. H. Gracias, "Self-Folding Polymeric Containers for Encapsulation and Delivery of Drugs," *Advanced Drug Delivery Reviews,* vol. 64, pp. 1579-1589, 2012.

[30] E. Hawkes, B. An, N. Benbernou, H. Tanaka, S. Kim, E. Demaine, *et al.*, "Programmable Matter by Folding," *Proceedings of the National Academy of Sciences,* vol. 107, pp. 12441-12445, 2010.

[31] K. Kuribayashi-Shigetomi, H. Onoe, and S. Takeuchi, "Cell Origami: Self-Folding of Three-Dimensional Cell-Laden Microstructures Driven by Cell Traction Force," *PloS one,* vol. 7, p. e51085, 2012.

[32] Y. Liu, J. K. Boyles, J. Genzer, and M. D. Dickey, "Self-Folding of Polymer Sheets using Local Light Absorption," *Soft Matter,* vol. 8, pp. 1764-1769, 2012.

[33] B. Noy, M. S. George, B. Alla, Y. A. Nana, and H. G. David, "Hands-Free Microscale Origami," in *Origami 5*, ed: A K Peters/CRC Press, 2011, pp. 371-384.

[34] C. L. Randall, E. Gultepe, and D. H. Gracias, "Self-Folding Devices and Materials for Biomedical Applications," *Trends in Biotechnology,* vol. 30, pp. 138-146, 2012.

[35] J. Ryu, M. D'Amato, X. Cui, K. N. Long, H. J. Qi, and M. L. Dunn, "Photo-Origami - Bending and Folding Polymers with Light," *Applied Physics Letters,* vol. 100, p. 161908, 2012.

[36] V. B. Shenoy and D. H. Gracias, "Self-Folding Thin-Film Materials: From Nanopolyhedra to Graphene Origami," *MRS Bulletin,* vol. 37, pp. 847-854, 2012.

[37] M. F. Ashby, *Materials Selection in Mechanical Design*: Butterworth-Heinemann, 2005.

[38] A. R. A. Ragab and S. E. A. Bayoumi, *Engineering Solid Mechanics: Fundamentals and Applications*: CRC Press, 1998.

[39] R. L. Norton, *Machine Design : An Integrated Approach*. Boston: Prentice Hall, 2011, pp. 869.

[40] Carbide Depot. (Accessed October 2014). *Coefficients for Static Friction on Steel*. Available: https://www.carbidedepot.com/formulas-frictioncoefficient.htm

[41] Oilite Ltd. (Accessed October 2014). *Technical Pamphlet on Oilite Bushings*. Available: http://www.ondrives.com/data/pdf/bearings/bushings/oilites-tech.pdf

[42] McMaster-Carr. (Accessed February 2015). *Product Listing: Moisture-Resistant Polyester Film: .0005" Thick, 27" Width, 10' Length, Clear*. Available: http://www.mcmaster.com/#8567k102/=xbqq2h

Appendix A

Derivation of Equation (30)

The strains experienced by the membranes in the folding system are very large, (well exceeding 100%). Therefore the common small-deformation approximation for the effect of Poisson's Ratio on the out-of-plane dimension (thickness) is not valid, and a large-displacement approach is necessary. The derivation for this is as follows:

From the fundamental equation for Poisson's Ratio:

$$\frac{dt}{t} = -\nu \frac{dl}{l} \tag{57}$$

$$\int_{t_0}^{t_0+\Delta t} \frac{dt}{t} = -\nu \int_{l_0}^{l_0+\Delta l} \frac{dl}{l} \tag{58}$$

$$\ln\left(\frac{t_o + \Delta t}{t_0}\right) = -\nu \ln\left(\frac{l_o + \Delta l}{l_0}\right) \tag{59}$$

$$1 + \frac{\Delta t}{t_0} = \left(1 + \frac{\Delta l}{l_0}\right)^{-\nu} \tag{60}$$

$$\epsilon_t = -1 + (1 + \epsilon_l)^{-\nu} \tag{61}$$

Appendix

B

Subsystem Diagrams

The following pages contain high-resolution illustrations of the subsystems in the prototype machine. These figures are shown previously in Chapter 4, but are repeated here in more detail for easier viewing. Five subsystems are pictured:

1. 80/20 Frame
2. Winding Axles
3. Winding Motors
4. Central Rollers
5. Mating Components

In each case, the subsystem of interest is colored, while unrelated components are drawn as wireframes.

a) Upper Subassembly

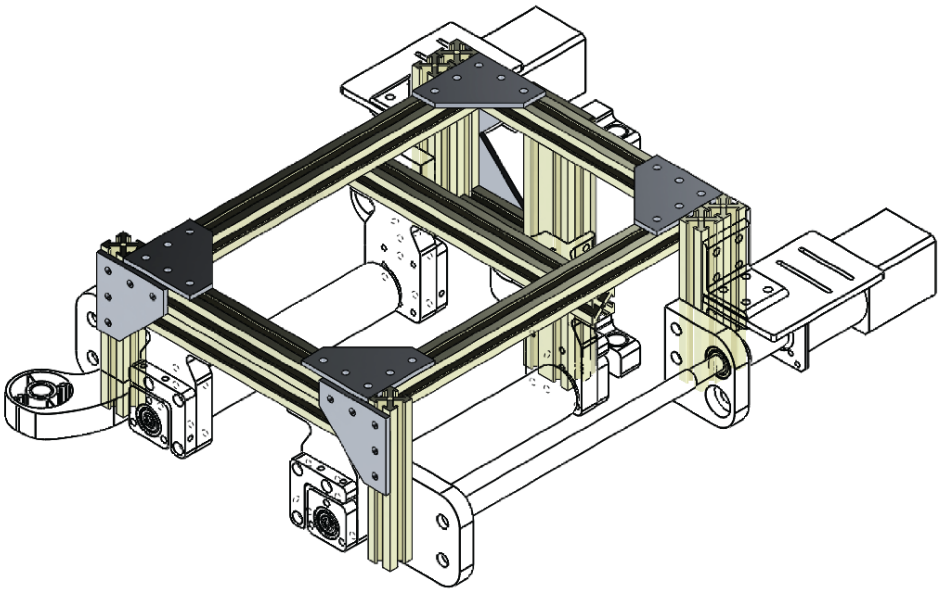

b) Lower Subassembly

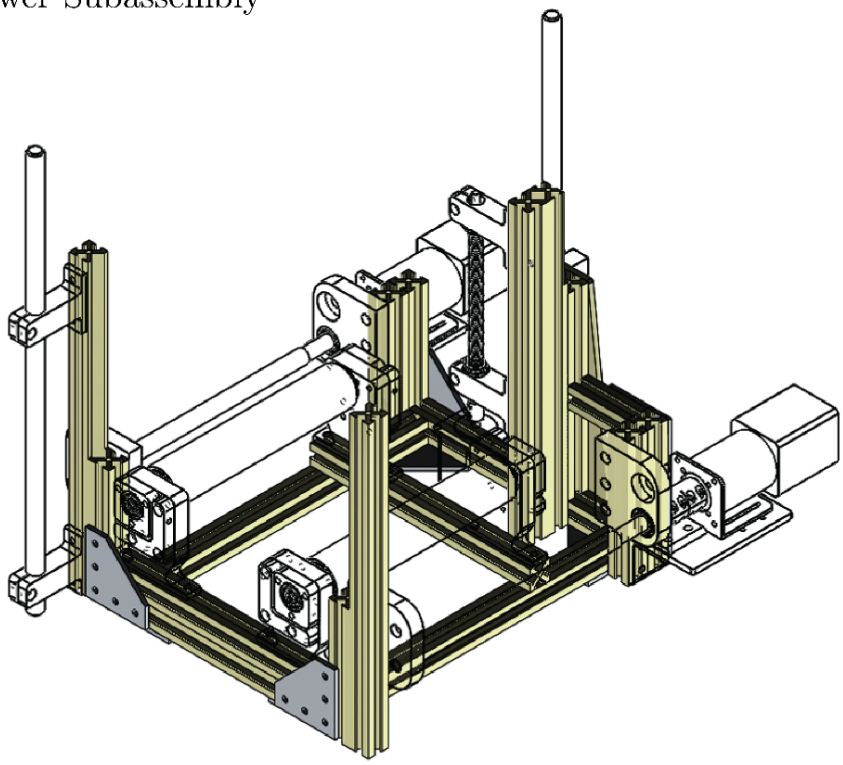

Figure B-1: Large illustration of "80/20 Frame" subsystem

a) Upper Subassembly

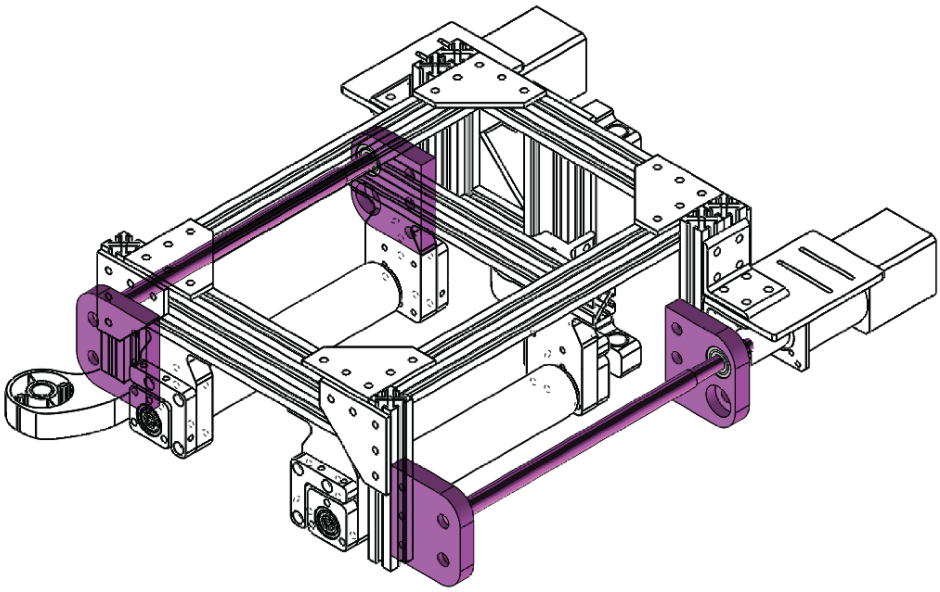

b) Lower Subassembly

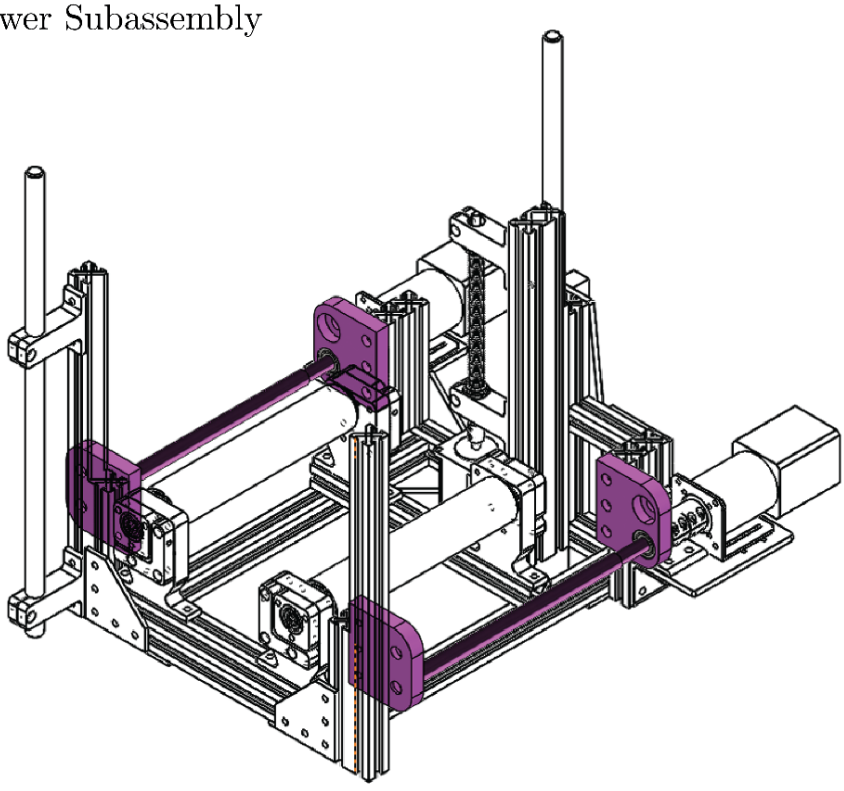

Figure B-2: Large illustration of "Winding Axles" subsystem

a) Upper Subassembly

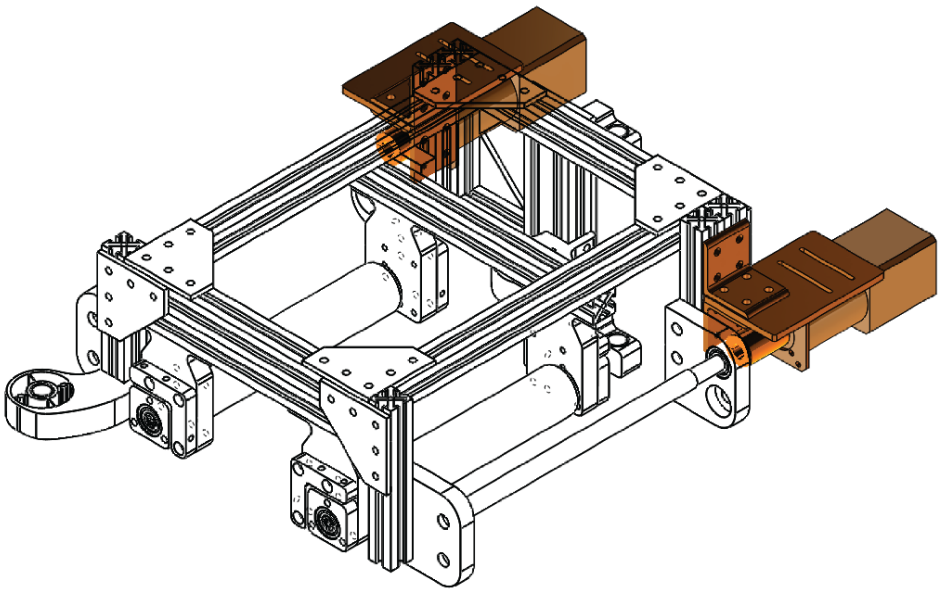

b) Lower Subassembly

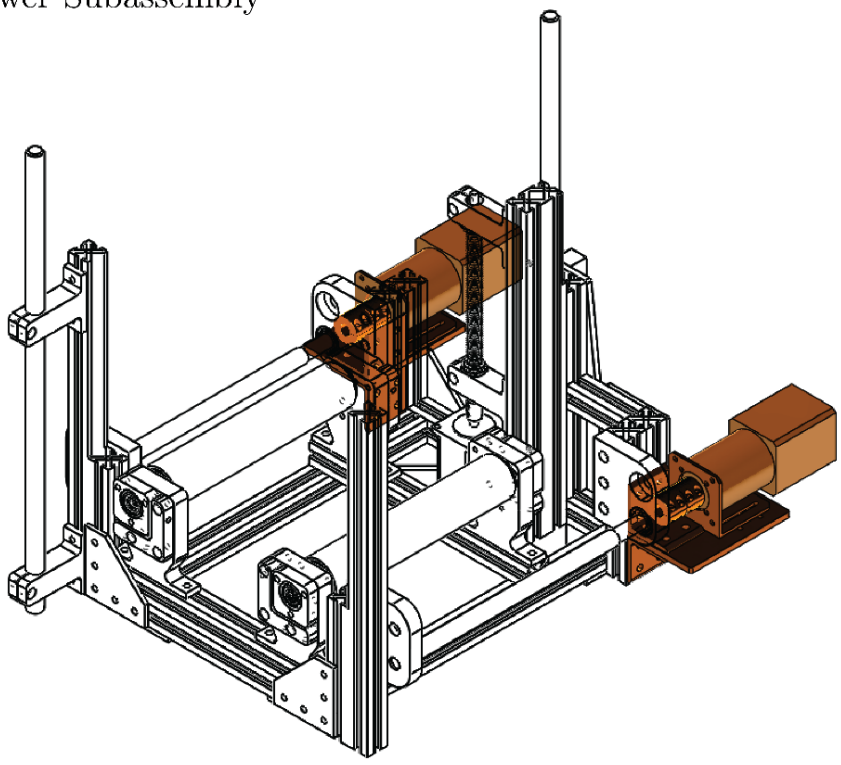

Figure B-3: Large illustration of "Winding Motors" subsystem

a) Upper Subassembly

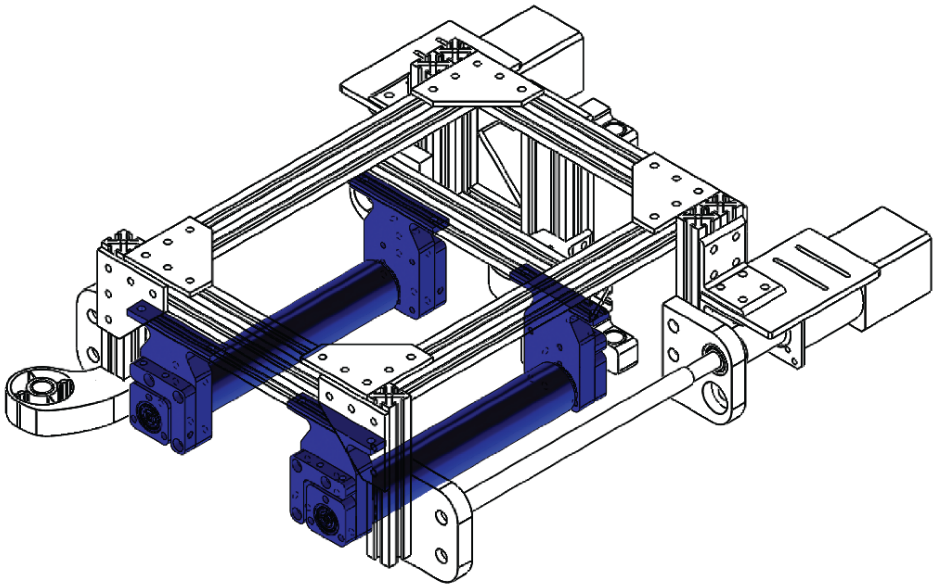

b) Lower Subassembly

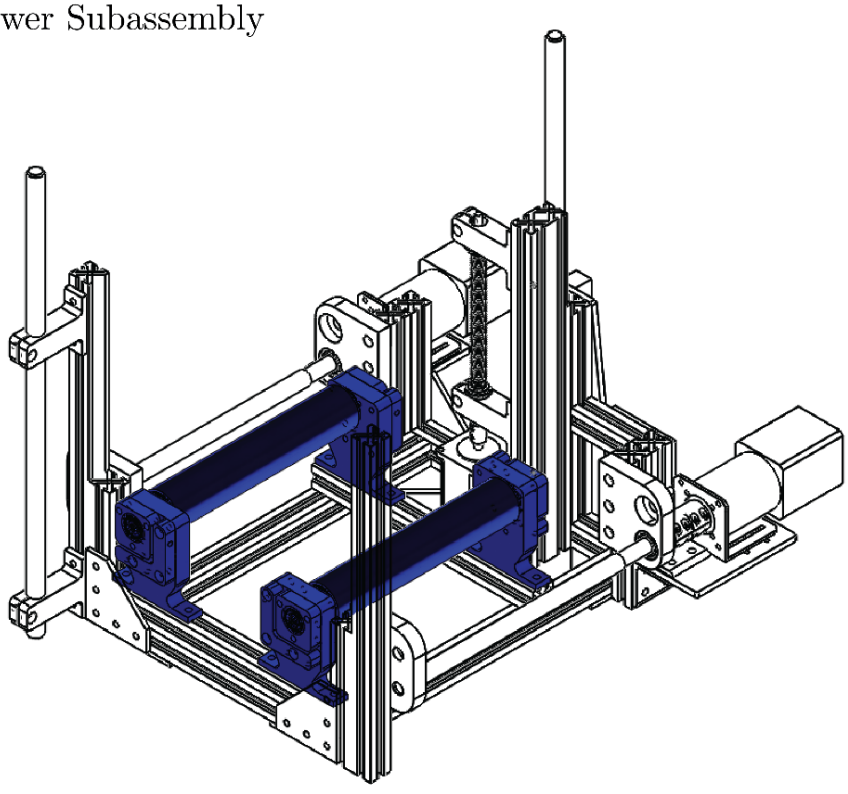

Figure B-4: Large illustration of "Central Rollers" subsystem

a) Upper Subassembly

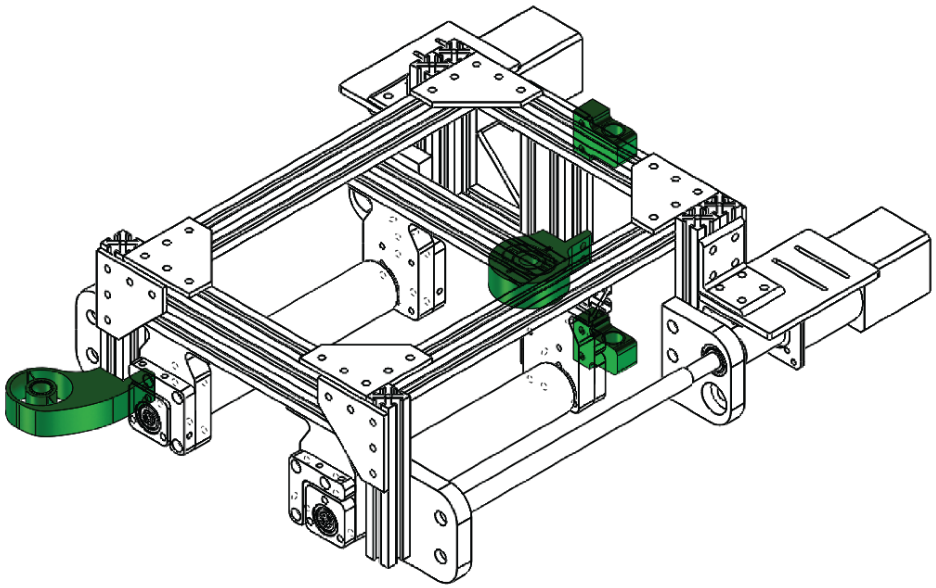

b) Lower Subassembly

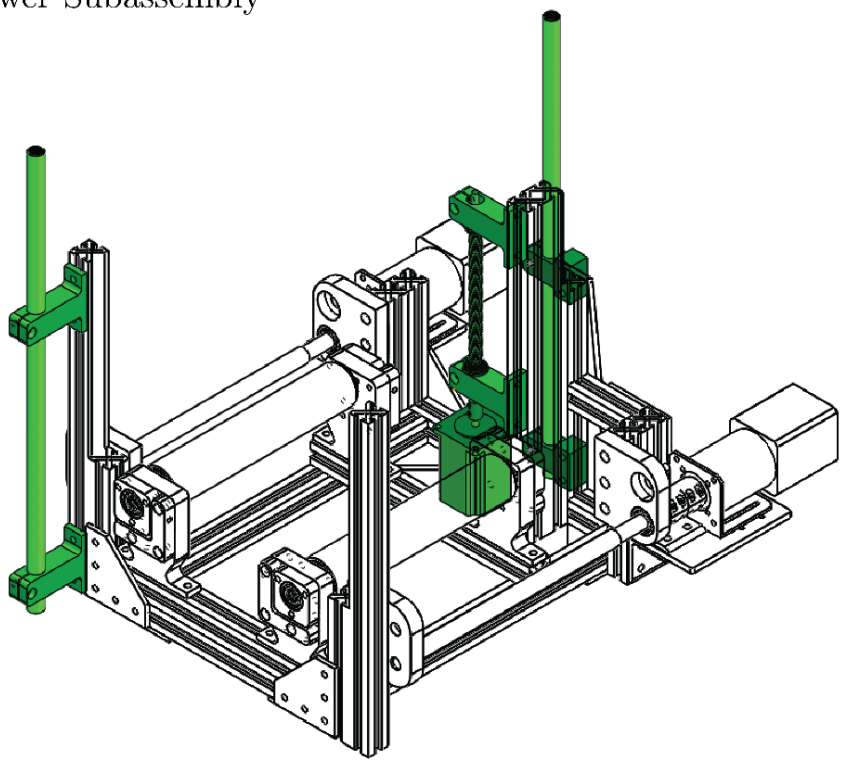

Figure B-5: Large illustration of "Mating Components" subsystem

Appendix C

Field-of-View Correction

A GoPro Hero 3 Black Edition camera was used to capture the photographs used for the measurements presented in Chapter 5. This camera has a wide angle of the lens (94.4 degrees along the measured direction) and was placed a relatively short distance from the folding membrane (158 mm / 6.2”). Due to the lens angle and close proximity to the measured surface, pixel counts do not convert directly to distance measurements; an angular correction must be applied.

The camera configuration is represented as:

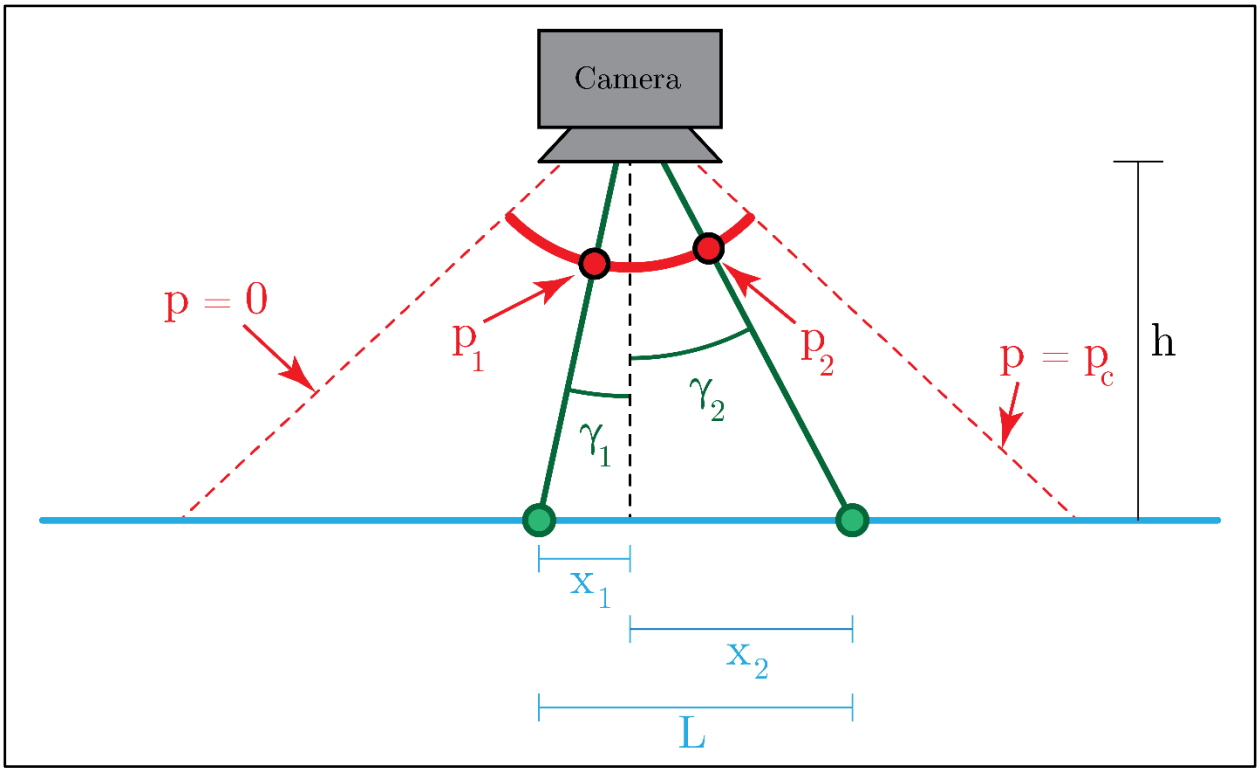

Figure C-1: Diagram for camera field-of-view correction

In this configuration, points on the measured plane (blue) are detected at a pixel (red) of the camera sensor. The transformation from pixel coordinate (p) to plane coordinate (x) is as follows:

The pixel coordinate p_i relates to the angle γ_i as:

$$\frac{p_i - \frac{p_c}{2}}{p_c} = \frac{\gamma_i}{FOV} \tag{62}$$

Here, P_c is the pixel resolution in the measured direction and FOV is the angular field-of-view in the measured direction. The measured plane location relates to the angle by:

$$x_i = h \tan \gamma_i \tag{63}$$

The pixel coordinate can be converted to the measured plane location:

$$x_i = h \tan\left(FOV * \frac{p_i - \frac{p_c}{2}}{p_c} \right) \tag{64}$$

And the distance between points x_1 and x_2 is:

$$L = |x_2 - x_1| = \left| h\left(\tan\left(FOV * \frac{p_2 - \frac{p_c}{2}}{p_c} \right) - \tan\left(FOV * \frac{p_1 - \frac{p_c}{2}}{p_c} \right) \right) \right| \tag{65}$$